Supercapacitive Sensors for Force/Strain Measurements in Biomedical Applications

A DISSERTATION
SUBMITTED TO THE FACULTY OF THE
UNIVERSITY OF MINNESOTA
BY

Ye Zhang

IN PARTIAL FULFILLMENT OF THE REQUIREMENTS
FOR THE DEGREE OF
DOCTOR OF PHILOSOPHY

Adviser: Rajesh Rajamani

August 2019

© Ye Zhang 2019
All rights reserved

Acknowledgements

First and foremost, I would like to express my sincere gratitude to my advisor Professor Rajesh Rajamani for his guidance and support throughout the years at the University of Minnesota. His advice on my research and motivation and encouragement have been invaluable. He is a great advisor, professorial researcher, and mentor. His enthusiasm, creativity, hardworking nature, positive mindset, and acts of kindness have brought constant encouragement to me.

I am very grateful to my dissertation committee members Professor Julianna Abel, Professor Suhasa Kodandaramaiah, and Professor Gerald Timm for insightful comments and feedback in improving this dissertation.

I would also like to extend my gratitude to Lee Alexander for his help and suggestions in developing test stands and prototypes.

I would also like to thank all past and current lab mates: Dr. Yan Wang, Dr. Shan Hu, Dr. Garrett Nelson, Dr. Mahdi Ahmadi, Dr. Song Zhang, Dr. Ryan Madson, Dr. Woongsun Jeon, Corey Cruttenden, Zhenming Xie, Greg Johnson, Heng Wang, Hamidreza Movahedi, and Dingyi Gu. It has been a pleasure to work alongside them. To those that joined the lab the same time as me, Dr. Ryan Madson and Dr. Woongsun Jeon, I could not imagine going through this process with anyone else. I am grateful for your support both academically and personally.

A special thank you to Tianyou for being a part of my life and for all the support, understanding, patience, generosity, joy and love that you bring.

Most importantly, I would like to express my sincere appreciation to my parents. This dissertation would not have been accomplished without their support and love. Thank you for teaching me the significance of determination, diligence, sincerity and perseverance and for motivating and encouraging me in all that I do. You are my ultimate inspiration.

This research was supported in part by Mn-Reach, a NIH Research Evaluation and Commercialization Hub, and by the National Science Foundation under Grant EFRI 1830958.

Dedication

To my beloved parents, Furen Zhang and Xiuying Wang

Abstract

This dissertation develops a new class of flexible force and strain sensors based on the principle of supercapacitive sensing. The sensing mechanism consists of a change in capacitance in a double-layer supercapacitor in response to an applied force or strain by inducing a change in the contact area between an electrolyte and a pair of electrodes. The new sensors can provide a measurement sensitivity several orders of magnitude higher than traditional capacitive sensors, and have other advantages such as flexibility, soft material construction, ability to operate in liquid environments, tremendous ease of fabrication and unprecedented configurability.

As a key component of the new sensors, a paper-based solid-state electrolyte with high deformability is developed. The paper substrate can be easily cut and shaped into complex three-dimensional geometries on which ionic gel can be coated. Paper dissolves in the ionic gel after determining the shape of the electrolyte, leaving behind transparent electrolyte structures with micro-structured fissures responsible for their high deformability. Exploiting this simple paper-based fabrication process, this dissertation develops diverse sensors of different configurations and demonstrates their operation and their advantages.

First, force sensors in multiple configurations involving electrolytes that are arch-shaped, corrugated and dome-shaped are fabricated. They have sensitivity that is 1000 times larger than similarly sized capacitive sensors and have negligible parasitic capacitance when used in immersive liquid environments. The use of such force sensors on a urethral catheter which can be used to diagnose the cause of urinary incontinence in a Urology application is demonstrated. A urethral catheter with five distributed force sensors is fabricated that can be used to measure distributed urethral closure pressure in a human subject. Experimental results with the catheter, including cuff tests and ex vivo tests are presented.

Next, their high sensitivity allows the use of multiple supercapacitive sensors together in a quad structure to enable a sensor in which normal and shear forces can be simultaneously measured. Such a sensor can have multiple applications in robotics and in

wearable monitoring systems which can benefit from measurement of multi-axis forces. The performance of the multi-axis normal-shear force sensor is evaluated using extensive experimental data with a wide range of force combinations. Due to manufacturing imperfections, the sensor does not have uniform axisymmetric sensitivity. Hence, a learning algorithm which utilizes a deep neural network to model the sensor response to multi-axis forces is developed and implemented. The learning algorithm allows the sensor system to provide highly accurate normal and shear force estimates, no matter what the alignment of the forces applied on the sensor.

Finally, the use of the supercapacitive sensors for strain measurement is evaluated. The paper-based electrolyte is strengthened with silicate nanoparticles to allow it to withstand over 110% stretch without failure. The strengthened electrolyte is used in a unique strain sensor design. The strain sensor is shown to have ultra-high sensitivity and its performance in a wearable home-monitoring application to measure the size of the leg and thus monitor leg-swelling is demonstrated.

The contributions of this dissertation include the development of a new soft deformable electrolyte, the development of a paper-based supercapacitive sensor system, and the development of novel sensor configurations such as a simultaneous normal-shear force sensor, a distributed urethral catheter with multiple pressure sensors and a highly stretchable strain sensor. The developed class of new sensors provides extremely high sensitivity and other advantages in spite of easy fabrication with no requirement for clean room facilities.

Table of Contents

List of Tables

List of Figures

Citations of Published Work

Some portions of this thesis have appeared in the following publications:

Journal Publications:

1) Zhang Y, Sezen S, Cheng X, and Rajamani R, "Supercapacitive Strain Sensor with Ultra-High Sensitivity and Range," *IEEE Sensors Letters*, vol. 3, no. 2, pp. 1-4, February 2019.
2) Zhang Y, Sezen S, Ahmadi M, Cheng X, and Rajamani R, "Paper-Based Supercapacitive Mechanical Sensors," *Nature Scientific Reports*, vol. 8, no. 1, Article16284, November 2018.
3) Zhang Y, Rajamani R, and Sezen S, "Novel Supercapacitor-Based Force Sensor Insensitive to Parasitic Noise," *IEEE Sensors Letters*, vol. 1, no. 6, pp. 1-4, December 2017.
4) Zhang Y and Rajamani R, "High Voltage Thin Film Supercapacitor with Nano-Structured Electrodes and Novel Architecture," Technology, vol. 4, no. 1, pp. 55-59, March 2016.
5) Zhang C, Yu X, Alexander L, Zhang Y, Rajamani R, and Garg N, "Piezoelectric Active Sensing System for Crack Detection in Concrete Structures," Journal of Civil Structural Health Monitoring 6(1):129–139, February 2016.

Conference Publications:

1) Zhang Y, Ahmadi M, and Rajamani R, "An Instrumented Urethral Catheter with Supercapacitor Based Force Sensor," ASME. Frontiers in Biomedical Devices, 2018 Design of Medical Devices Conference (): V001T06A002. doi:10.1115/DMD2018-6904.

2) Ahmadi M, Zhang Y, Rajamani R, Timm G, and Sezen S, "A Supercapacitive Pressure Sensor for a Urethral Catheter," in Proceedings of the 2018 IEEE Electronics in Medicine and Biology Conference, Honolulu, Hawaii, USA, August 2018.
3) Zhang C, Ahmadi M, Yu X, Alexander L, Zhang Y, Rajamani R, and Garg N, "Piezoelectric Active Sensing System for Crack Detection in Concrete Structures," in 94th Transportation Research Board Annual Meeting, Chicago, IL, USA, January 2015.

Patent:

Zhang Y, Rajamani R, and Sezen S, "Flexible Electrolytes for Supercapacitor-Based Sensors," US Patent Application, 16/127,827 (2018).

Chapter 1

Introduction

The objective of this dissertation is to develop supercapacitive sensors for medical applications involving force and strain monitoring. The biomedical sensors are based on a new sensing principle, namely supercapacitive sensing. In a supercapacitive sensor, a change in mechanical force is translated into a change in the contact area between a pair of electrodes and an electrolyte, which consequently creates a change in capacitance. The new sensors have significantly higher sensitivity and several other advantages compared to traditional capacitive sensors.

1.1 Fundamentals of Supercapacitors

Supercapacitors, also called electrochemical capacitors or ultracapacitors, store their energy in the electric field of an electrochemical double-layer [1], [2]. A basic form of a supercapacitor is shown in Figure 1-1, consisting of two electrodes isolated from electrical contact. An electrolyte solution between the two electrodes enables the flow of ionic current between the electrodes.

In recent years, supercapacitors have attracted significant attention, mainly due to their high power density, long lifecycle, safety, and as a bridge for the power/energy gap between traditional dielectric capacitors and batteries/fuel cells [3]. In general, the electrodes in a supercapacitor are fabricated from materials that have high surface area and

high porosity. The charges can be stored and separated at the interface between the conductive solid particles of the electrodes and the ions of the electrolyte. The electrode-electrolyte interface can be treated as a capacitor with electrical double-layer capacitance, which can be expressed as

$$C = \frac{\varepsilon A}{d} \tag{1-1}$$

where A is the area of the electrode surface, which for a supercapacitor should be the active surface of the electrode porous layer; ε is the medium (electrolyte) dielectric constant, which will be equal to 1 for a vacuum and larger than 1 for all electrolyte materials.; and d is the effective thickness of the electrical double layer, which is the size of a couple of atomic layers, in the order of Angstroms. Thus, due to a large area A and extremely small distance d, the capacitive areal density of a supercapacitor can reach as high as $\mu F/cm^2$ [3], which is significantly larger than that of a conventional capacitor.

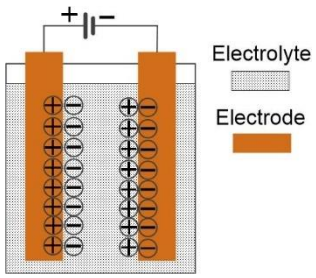

Figure 1-1 Schematic of a supercapacitor

There are two major types of supercapacitors. One is the electrical double layer capacitor (EDLC), in which the electrode material is not electrochemically active, i.e. the charge storage process is non-faradaic and electrostatic, and no electron transfer takes place across the electrode surface. The other type is the pseudocapacitor, in which the electrode material is electrochemically active, which can directly store charges during the charging and discharging process.

1.1.1 Electrical Double Layer Capacitor (EDLC)

The capacitance of the electrode/electrolyte interface in an EDLC is associated with an electrode-potential-dependent accumulation of electrostatic charge at the interface. The mechanism of surface charge generation includes surface dissociation as well as ion

adsorption from both the electrolyte and the crystal lattice defects. These processes operate solely on electrostatic accumulation of surface charges. The electrical double layer capacitance comes from electrode materials particles and electrolyte, where an excess or a deficit of electric charges is accumulated on the electrode, and the electrolyte ions with counterbalancing charge are built up on the electrolyte side in order to meet electroneutrality. Most common materials for electrodes in an EDLC are carbon materials, including activated carbon [4], carbon aerogels [5], carbon nanofibers [6], carbon nanotubes (CNT) [7], Graphene [8], etc. [9]. Figure 1-2 shows a thin film EDLC developed in our lab using a graphene and CNT composite for the electrodes. The areal specific capacitance achieved was as high as 25 mF/cm^2 [10].

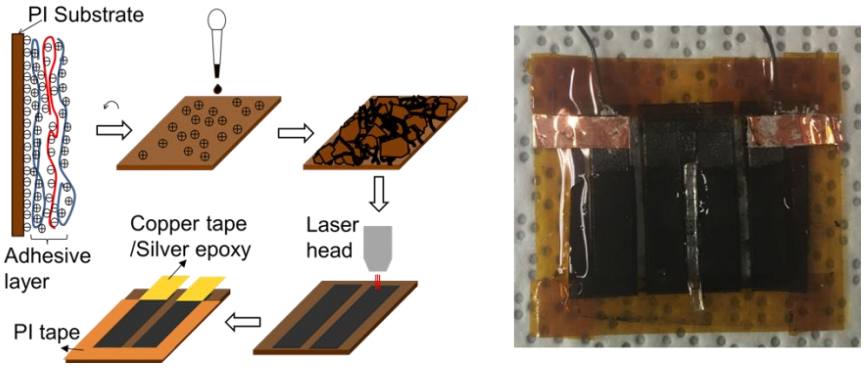

Figure 1-2 Thin-film supercapacitor with nano-structured electrodes [10]

1.1.2 Pseudocapacitor

In pseudocapcitors, when a potential is applied, fast and reversible faradaic reactions (redox reactions) take place on the electrode materials and involve the passage of charge across the double layer, similar to the charging and discharging process that occurs in batteries, resulting in faradaic current passing through the supercapacitor cell [11]. Materials undergoing such redox reactions include conducting polymers and several metal oxides, including RuO_2, MnO_2 , etc.[9] Three types of faradaic processes occur at pseudocapacitor electrodes: reversible adsorption, redox reactions of transition metal oxides, and reversible electrochemical doping-dedoping in conductive polymer-based electrodes. These processes not only extend the working voltage but also increase the specific capacitance of the supercapacitors [12]. Since the electrochemical processes occur

both on the surface and in the bulk near the surface of the solid electrode, a pseudocapacitor exhibits far larger capacitance values and energy density than an EDLC. However, a pseudocapacitor suffers from relatively lower power density than an EDLC because faradaic processes are normally slower than nonfaradaic processes. Moreover, because redox reactions occur at the electrode, a pseudocapacitor often lacks stability during cycling, similar to batteries.

Nowadays, there is also research interest in hybrid supercapacitors with an asymmetrical electrode configuration, in which both EDLC and faradaic capacitance mechanisms occur [12], [13].

Due to the stability and long cycle life of EDLC, it is favorable to be used in mechanical sensors, compared to the less stable pseudocapacitor. Therefore, in this dissertation, we are only interested in making use of EDLCs in mechanical sensors. So, unless stated otherwise, supercapacitors indicate EDLCs in this dissertation.

Supercapacitors have been widely used as energy storage devices, but have only been recently explored as force sensors. Similar to a capacitive force sensor, an applied force is converted to a change in capacitance in a supercapacitive sensor. However, the working mechanism of a supercapacitive sensor is different from a capacitive sensor: the former device converts a contact area change between the electrodes and the electrolyte to a change in capacitance, while the latter one converts a distance change between the parallel electrodes to a change in capacitance. In next section, capacitive sensors are first discussed before the introduction of supercapacitve sensors as a comparison.

1.2 Capacitive Force/Pressure Sensors

Capacitive transducers for force, acceleration and angular rate have found their applications in many fields and are a well-established sensor technology. However, they suffer from errors due to parasitic noise and have a significant sensitivity versus range trade-off in their performance.

1.2.1 Introduction to Capacitive Force/Pressure Sensors

MEMS (Microelectromechanical systems) accelerometers [14]–[16] and gyros[17], [18] based on the capacitive mechanism are the most widely sold MEMS devices. They have advantages of low cost and low power consumption. Working on a similar principle, capacitive pressure sensors, also have similar properties.

Pressure sensors have been widely used in medical, aerospace, automobile, industrial and commercial applications [19]. These sensors may be based on piezoresistive, capacitive, or optical principles [20]. Among them, capacitive sensors are noteworthy, due to their low temperature hysteresis and pressure hysteresis, capability for miniaturization, and low power consumption. Generally, a capacitive pressure sensor consists of two parallel electrodes. One electrode is a membrane or attached to a membrane, while the other is fixed. When pressure is applied on the membrane, it deforms and displaces. The relative movement of the electrodes results in a capacitance change depending on the distance between the two electrodes as shown in Figure 1-3.

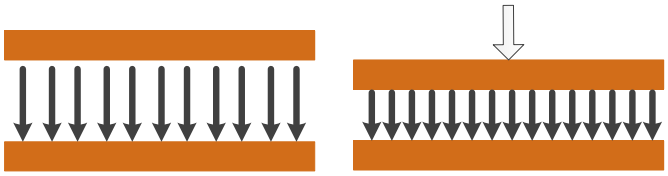

Figure 1-3 Working mechanism of a capacitive force sensor

1.2.2 Mechanical Capacitive Sensors for Biomedical Applications

Measurement of pressure in various parts of the human body is of great significance in biomedical applications. These sensors may be based on electrolyte conductance [21], L/C resonance [22], optics [23], piezoresistive[24], [25] or capacitive[26]–[28] sensing principles. These pressure sensors have been used by researchers to measure blood pressure[28], intraocular pressure[22], record nerve tissue signals[26], record gait and physical activity[29], etc. MEMS capacitive pressure sensors have been particularly noteworthy due to their easy miniaturization, low power consumption, freedom from temperature effects, and IC compatibility. Generally, the capacitive sensors are based on traditional parallel plate capacitors. These sensors can be generally categorized by working

principles into several types:

(1) Cavity based parallel-plate pressure sensors [22], [28], [30]–[32]

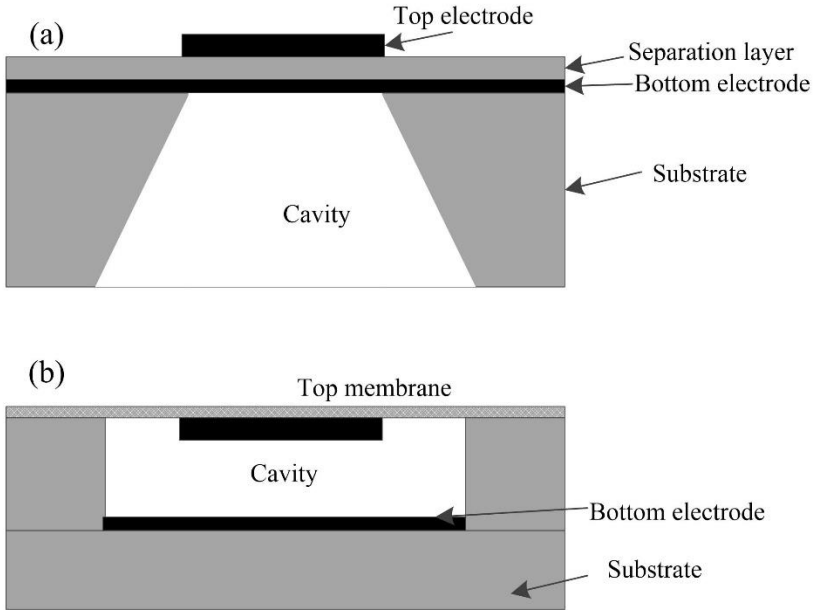

Figure 1-4 Cavity based parallel-plate pressure sensor: (a) cavity on one side of the two electrodes; (b) cavity between the two electrodes

Figure 1-4 illustrates two typical configurations of this kind of sensor. Each has a chamber that is closed off by an elastic membrane and usually a cavity filled with air or other dielectric material is formed. The capacitance of the capacitor changes due to the variation of distance between the membrane and the backside of the chamber, a co-operating electrode.

(2) Touch mode pressure sensor [33]–[38]

Touch mode capacitive pressure sensor produces close linear capacitance to pressure relationship. The conducting diaphragm touches a dielectric coated ground plane (Figure 1-5 (a), (b)). The major component of output capacitance is the capacitance of the touched area with a thin layer of isolation layer which gives a larger capacitance per unit area compared to the air-gap capacitance in the untouched area.

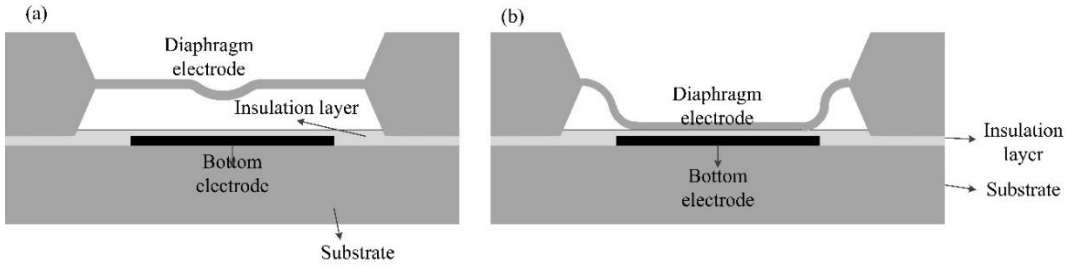

Figure 1-5 Touch mode pressure sensor (a) original position, (b) with force applied

(3) Cavity-free pressure sensor [26], [29], [39], [40]

In this type of sensor, no cavity is created, which reduces the space needed for the sensor body. Two structures of this type of sensor are shown in Figure 1-6. Figure 1-6 (a) and (b)) show a sensor with deformable electrode. Figure 1-6 (c)) shows a cavity-less sensor dependent on the deformation of the elastic dielectric layer.

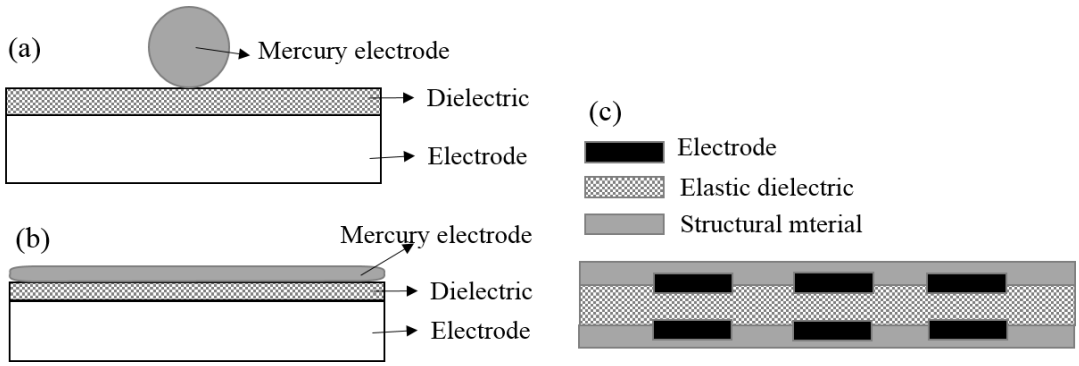

Figure 1-6 Cavity-free pressure sensor (a) mercury electrode sensor (original state), (b) mercury electrode sensor (with force applied), (c) flexible dielectric sensor.

1.2.3 Challenges in Use of Capacitive Sensors for Biomedical Applications

Due to the working mechanism of traditional capacitive pressure sensors involving separation between micro-fabricated electrodes, the sensitivity of most traditional capacitive sensors is low, usually around several pF/kPa.

The behavior of a simple electrostatic capacitor can be generally described by

$$C = \frac{\varepsilon A}{d} \tag{1-2}$$

where the capacitance is a function of the permittivity, ε, the device dimensions with A being the plate cross sectional area and d being the distance between the two parallel plates.

Most capacitive sensors measure capacitance changes due to the change of the distance d.

Taking the derivative of the capacitance in equation(1-2) with respect to d, we get

$$\frac{\partial C}{\partial d} = -\frac{\varepsilon A}{d^2} \tag{1-3}$$

So, the free distance d between the electrodes needs to be small to achieve a high $\partial C/\partial d$.

For purposes of illustrating the trade-off between sensitivity and range, assume a simple mechanical model for the capacitor sensor dynamics, as shown in Figure 1-7. Then

$$\Delta F = k\Delta d \tag{1-4}$$

where k is the stiffness, Δd is the deflection of the sensor, and ΔF is change of applied force. Then, from equations (1-3) and (1-4), the sensitivity of the sensor can be expressed as:

$$\frac{\partial C}{\partial F} = -\frac{\varepsilon A}{kd^2} \tag{1-5}$$

From the above equation, to achieve high sensitivity, we want to keep d as small as possible. Usually, the free distance d is of the order of microns. But this limits the range of forces that can be measured, since the maximum force that can be measured before the electrodes touch is $F_{max} = kd$. If we want to enlarge the measuring range, we have to sacrifice the sensitivity of the sensor. A typical capacitive pressure sensor only offers a total change in capacitance of a few pico Farads, which usually needs the use of a compensation circuit to sense these very small variations in capacitance.

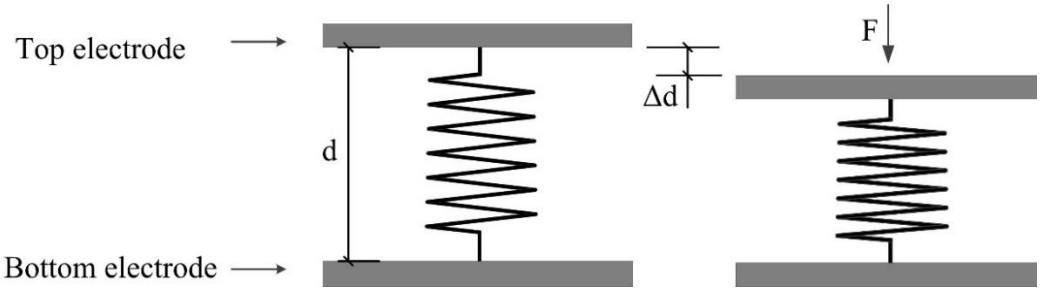

Figure 1-7 Mechanical model of capacitor

A second problem with traditional capacitive sensors is the existence of parasitic noise from fringe capacitance. In most electrostatic sensors that are fabricated by current MEMS

methods, the distance between the electrodes is not negligible relative to the lateral dimensions [41]. As shown in Figure 1-8, a fringe electric field is created on a parallel plate capacitor which has non-negligible distance between the plates. The discontinuity in the material results in additional radial components in the electric field, which in turn generates parasitic capacitance components on the sides of a capacitor.

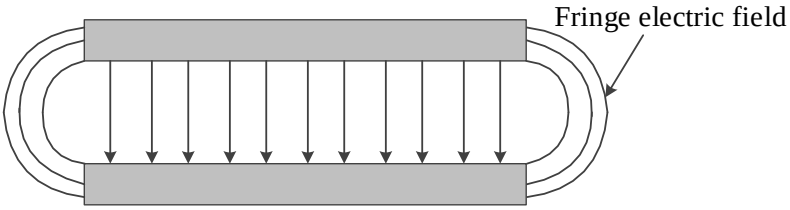

Figure 1-8 Fringe electric field on a parallel capacitor

Parasitic capacitance can also exist between other electronic components, passivation layers etc. in the capacitive sensors [42], [43]. The resultant parasitic capacitance is of the order of femto Farads (fF) to pico Farads (pF) in liquid environments. Parasitic capacitance can be compensated by measurement in the absence of loads and subsequent subtraction, but this is only possible when the parasitic noise is static. In biomedical in-vivo applications of the capacitive sensors, the interference from human tissues on the fringe electric field of the sensor can cause dynamic parasitic noise, which can greatly pollute the sensor signal and cannot be eliminated by subtraction. A simple bio-sensor is shown in Figure 1-9. As a human finger approaches the sensor, due to the existence of the fringe electric field, a portion of which will be shunted to the finger, an additional charge capacity, i.e. a parasitic capacitance, will be added to the capacitance of the sensor. This parasitic capacitance generally exists in all capacitive sensors and influences their accuracy.

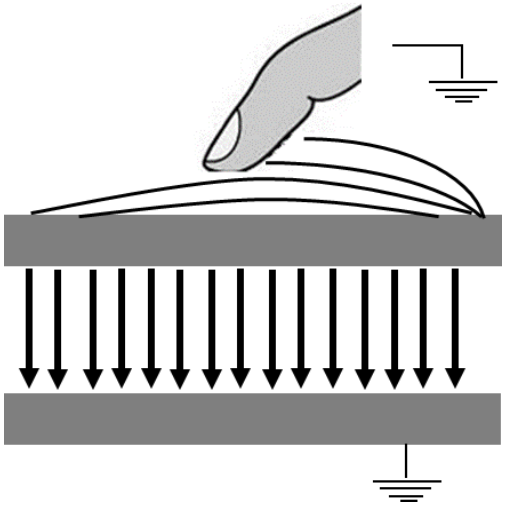

Figure 1-9 Parasitic capacitance on a parallel capacitor

Thus, traditional capacitive sensors suffer from two limitations:

- The trade-off between sensitivity and range

- Errors due to parasitic noise in liquid environments

These are the two limitations that this dissertation will attempt to address by the replacement of traditional capacitors with supercapacitors for sensing.

1.3 Supercapacitive Sensors

This dissertation proposes the use of supercapacitors as sensors to overcome the performance limitations of traditional capacitive sensors. Supercapacitors have been explored to store energy [1], [44]–[47] in the past due to their significantly higher energy density, compared to conventional capacitors, and their higher power density compared to batteries, as discussed in section 1.1. Their use for sensing, however, remains quite novel.

Sensing principles for supercapacitor-based sensors are developed in this dissertation in which a load dependent real-time change in capacitive area is utilized instead of a change in distance between parallel plates (Figure 1-10).

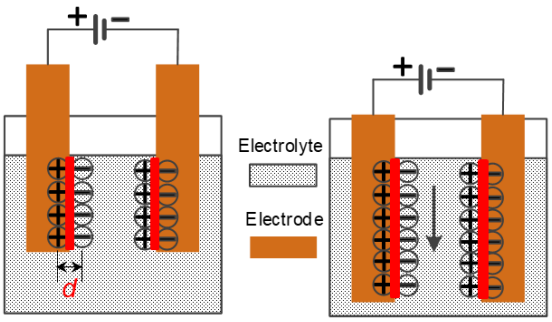

Figure 1-10 Working mechanism of a supercapacitive sensor

Parasitic capacitance can be a big concern for a conventional capacitive sensor. In a supercapacitive sensor, on the other hand, the sensitivity of capacitance change due to force is high enough to make the parasitic capacitance negligible. Besides, the fringe effect is negligible on a supercapacitive sensor, resulting in a minimal parasitic capacitance. Further, since, a supercapacitor-based sensor measures capacitance changes due to changes in capacitive area, instead of changes due to distance, the working range of the sensor is not limited by the short distance between the two parallel electrodes. Thus, significantly larger working range can be achieved.

Based on the analysis above, supercapacitive sensors may be immune to parasitics, and have both high sensitivity and large working range. However, the use of supercapacitors as sensors has hardly been explored. Only a couple of previous publications in literature have investigated the use of supercapacitor-based sensors.

In [48] a novel droplet-based pressure macro sensor is presented using elastic and capacitive electrode-electrolyte interfaces to achieve ultra-high mechanical-to-electrical sensitivity ($1.58\mu F/kPa$) and resolution ($1.58Pa$) with a simple device architecture. This sensor is designed based on the principle of electrical double layer capacitor (EDLC), which is one type of supercapacitor. It provides high sensitivity and resolution, but no miniaturized version of this sensor has been researched. Besides, the authors of the paper did not fully understand or seek the benefits of the supercapacitor sensors in terms of its ability to eliminate parasitic noise and to highly reduce the sensitivity vs. range constraint. For flow-based pressure sensing, [49] presented a pressure sensor using a one-side-electrode and an implementation of electrical double layer capacitance concept. A microchannel was created, inside which, fluidic volume changes by the applied pressure

and leads to a capacitance change. The sensitivity achieved was $0.77\mu F/kPa$, which is not impressive.

Since a supercapacitor has a much higher specific capacitance compared to traditional capacitors, supercapacitor-based force sensors have the potential of providing both higher sensitivity and higher immunity to parasitic capacitance. This is because parasitic capacitance is expected to remain of the order of pF on micro-sensors, while a supercapacitor might have nominal capacitance that is more than 3 orders of magnitude larger. The use of supercapacitor-based sensors for any real applications has never previously been pursued.

1.3.1 Supercapacitive Sensors with Liquid Electrolyte

In order to realize supercapacitive sensing, according to equation (1-1), the only term that can vary while sensing is the area A. By changing the relative position of the electrode in the electrolyte, we can change the contact area between the electrodes and electrolyte. Two liquid-electrolyte-based embodiments to realize this sensing principle are initially explored: droplet-based supercapacitive sensors and electrolyte pool-based supercapacitive sensors. Initial prototypes of both types of sensors are designed, fabricated and tested to establish feasibility of the proposed ideas.

(1) Electrolyte droplet-based sensors

The working mechanism of droplet-based sensors is shown in Figure 1-11(a). An electrolyte droplet is confined between two parallel electrodes. The surface of the electrodes is treated to be superhydrophobic. A hydrophilic spot in the center of the bottom electrode is made to anchor and stabilize the droplet, so it will not move around while sensing. By applying force, the distance between the two electrodes changes, and thus the droplet will be squeezed, and the contact area of the electrolyte droplet and the electrodes will change. That results in a change of capacitance. After the force on the sensors is released, the super hydrophobicity of the surface will facilitate the deformed droplet to go back to the original state. Available commercial superhydrophobic coatings can provide a water contact angle as high as $150°$.

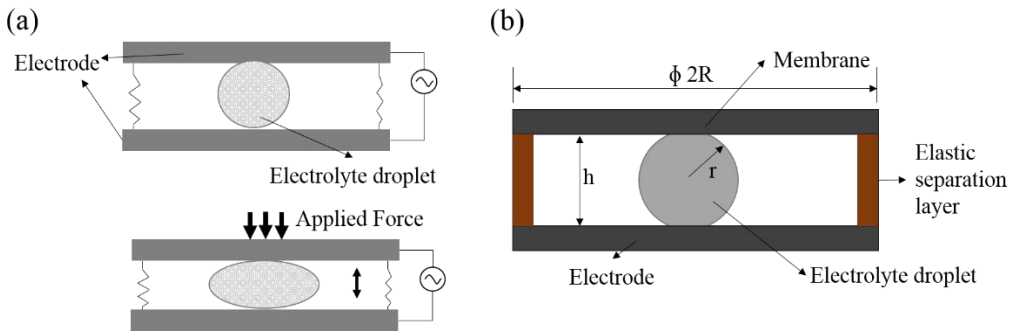

Figure 1-11 (a) Schematic of the droplet-based sensor (b) Analysis of droplet-based capacitive sensor principle

Figure 1-11 (b) illustrates a simple schematic of the droplet-based capacitive sensor with a droplet (radius r) in a cylindrical chamber (radius R, height h). The overall deformation of the sensing chamber, which includes the deflection of the flexible membrane and the compression of the elastic separation layer, will lead to the change of the contact area, and therefore, result in variation of capacitance. The mechanical-to-electrical sensitivity of the sensing device can be analytically expressed as [48]

$$\frac{\Delta C}{P} = c_0(\alpha R^2 + \beta h)\frac{D_d R^2}{h^2} \tag{1-6}$$

where, c_0 is the unit area capacitance, α, β represent the membrane deflection and the elastic deformation of the separation layer and can be determined by the geometrical and mechanical properties of the sensing membrane and the separation layer, respectively. The first term corresponds to the membrane deflection while the second term represents the separation layer deformation. They both contribute to the overall mechanical-to-capacitive sensitivity. A macro electrolytic droplet-based sensor prototype was initially fabricated as a part of this dissertation research to establish feasibility of the idea. A photograph of the fabricated sensor is shown in Figure 1-12.

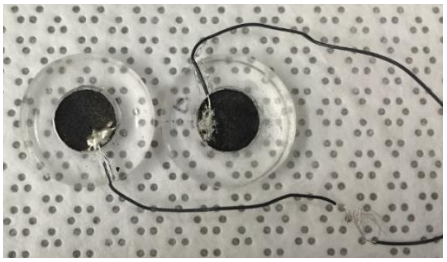

Figure 1-12 Photo of an electrolytic droplet-based sensor

The structural material of this sensor consists of PDMS (Polydimethylsiloxane). A mold machined from acrylic glass was used to cure the PDMS case. The PDMS base and curing agent were mixed at ratio of 10:1 and degassed, then the mixture was cast into the mold and cured. The electrode fabrication follows the same process discussed in [10]. Two circular electrodes (8mm in diameter) were cut using laser, and then glued to the PDMS case. The superhydrophobic spray (PFC M1604V, FluoroPelTM) was applied on the electrode surface. Silver epoxy was used as the contact at the two electrodes. The two pieces were then assembled together to make a sensor. The sensor was tested using a force gauge (Torbal, FC50, $50NX0.01N$). The capacitance increases monotonically as the applied force on the sensor increases, as shown in Figure 1-13. However, the challenge in this simple-minded design is the need to prevent the influence of gravity. Besides, it is challenging to downsize the sensor because it is hard to create a micro-sized droplet.

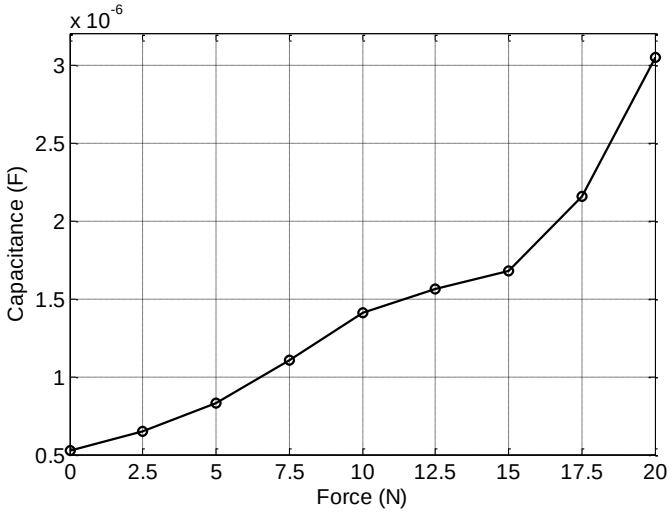

Figure 1-13 Capacitance response of the droplet-based sensor

(2) Electrolytic pool-based supercapacitive sensor

A schematic of an electrolytic pool-based sensor is shown in Figure 1-14. The electrodes of the sensor are immersed in a pool of electrolyte. A force on the electrode causes deformation and then a change of the dipped length inside the electrolyte. This consequently changes the capacitance.

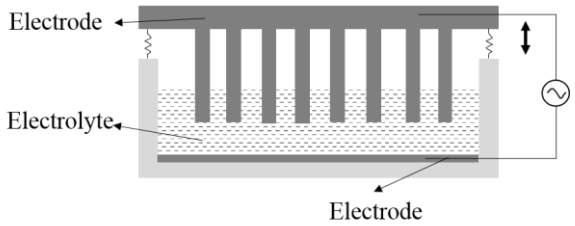

Figure 1-14 Schematic of electrolytic pool-based sensors

A macro electrolytic pool-based pillar sensor prototype was also fabricated in this dissertation research to establish feasibility of the idea. A photograph of the deformable top electrode of the fabricated sensor is shown in Figure 1-15.

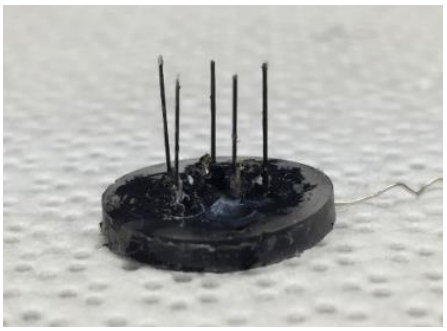

Figure 1-15 Deformable top electrode of the electrolytic pool-based sensor

Optical fibers (FT200EMT, $\varnothing 200\,\mu m$ Multimode Optical Fiber, THORLABS) were used as the structural material. Acid-treated functionalized CNTs were used as the effective electrode material. The polymer cladding on the silica core of the optical fiber (OF) makes a layer-by-layer CNT fabrication method possible, which helps the CNTs adhere to the OFs. PDMS was also used as material for the sensor case. The OF/CNT electrodes were dipped into a superhydrophobic spray (PFC M1604V, FluoroPel^{TM}) for 15 mins and then dried in the air for 6 hrs.

The submerged depth of OF/CNT electrode in the electrolyte was changed using a translation stage with 10 microns resolution in translational movement. The static capacitance of the sensor was measured using a Potentiostat (Digi Ivy 2000). The results are shown in Figure 1-16. Three rounds data were recorded with seven positions in each round. The distance between two positions is 0.5 mm.

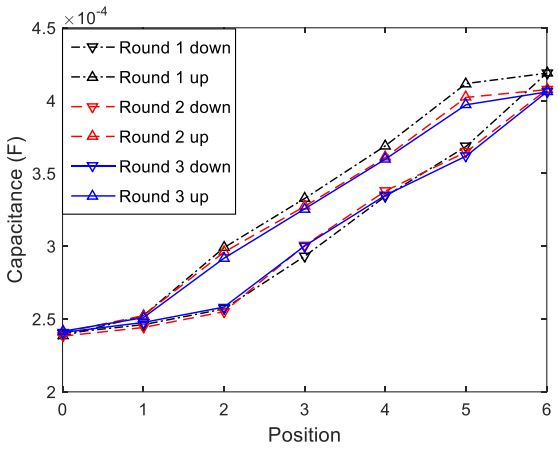

Figure 1-16 Capacitance response of the electrolytic pool-based sensor

There is hysteresis in the capacitance, i.e. the pushing-down process always has lower capacitance than the pulling-up process. As shown in Figure 1-17, it takes time for the electrolyte solution to drain from the already-wetted part of the electrode while pulling up. There are electrolyte ions left in the micro or nano pores of the CNTs on the electrode shortly after the electrodes being pulled up, which contributes to the hysteresis. So, measures have to be taken to reduce the hysteresis. Besides, the challenge in this simple-minded design is the need to prevent the influence of gravity due to tilting and from changing the height of the liquid electrolyte.

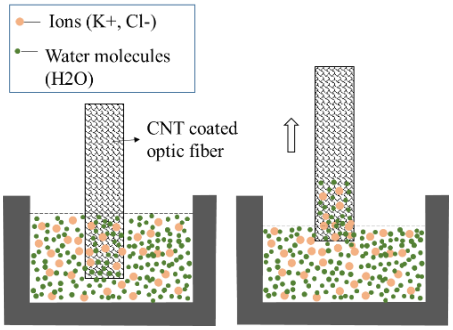

Figure 1-17 Hysteresis of the OF/CNT electrode while pulling up from electrolyte

1.3.2 Supercapacitive Sensors with Solid-State Electrolyte

The liquid-state supercapacitive sensors have several inherent disadvantages, which limit the broad use of these sensitive sensors:

(1) The sensors cannot be easily miniaturized to create micro-sensors, since it is

difficult to create size-controlled micron-sized droplets or liquid pool and to trap the liquid inside a sealed sensor;

(2) The presence of the hydrophobic coating on the surface of the electrodes reduces the capacitance, because it increases the distance between the electrolyte and the electrode;

(3) Even in large-sized sensors, each sensor needs to be individually calibrated to account for variability in liquid size and location inside the sensor chamber;

(4) The high cost of the hydrophobic coating and the large size of the sensor pose problems in creating a sheet of such sensors for measuring distributed forces (e.g. forces from the foot of a patient as he/she walks);

(5) The shelf life of liquid-state sensors is short due to atmospheric evaporation;

(6) The effect of gravity on the liquid may limit their application in systems involving non-planar motion.

In this dissertation, a functionalized paper as a substrate for making highly flexible solid-state electrolytes in supercapacitive force sensors is developed, which help address all of the above limitations of current liquid-based supercapacitive sensors. The new electrolytes are made by introducing active materials into the porous matrix of paper and functionalizing the entire thickness of the paper. The deformation of the electrolytes in response to an applied force and the resulting change in its contact area with the electrodes can then be used to sense the applied force, as shown in Figure 1-18.

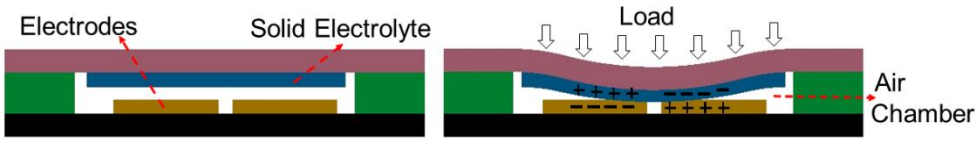

Figure 1-18 Supercapacitive sensors with solid electrolyte before and after loading

1.4 Thesis Contributions

The primary research contributions of this dissertation are as follows:

1) Development of a new method for fabricating solid-state electrolytes based on

paper substrates coated with ionic gel. This paper-based solid electrolyte has high flexibility, low Young's modulus and offers tremendous ease of fabrication.

2) Development of supercapacitive sensors using the new paper-based solid electrolyte. The supercapacitive sensors have ultra-high sensitivity and negligible parasitic capacitance when used in liquid environments.
3) Development of an instrumented urethral catheter based on supercapacitive sensing principles for a Urology application. This catheter can be used to measure the distributed pressure inside the urethra. The supercapacitive sensor has a sensitivity more than 1000 times higher than a conventional capacitive sensor. It has negligible parasitic noise, which makes it appropriate for in vivo use in the urethra.
4) Development of a supercapacitive sensor that can simultaneously measure normal and shear forces. A quad-unit force sensing cell consisting of 4 internal individual force units is designed and fabricated using MEMS fabrication and 3D printing. A neural network is used to model and learn the sensor response, so that it provides an accurate estimate of the shear and normal forces no matter what the alignment of the applied force is.
5) Development of a supercapacitive strain sensor based on a nanoparticle-strengthened solid electrolyte. The strain sensor has high sensitivity, can withstand over 100% strain and can differentiate extremely small strain.

1.5 Thesis Outline

The structure of the rest of this dissertation is as follows:

In Chapter 2, the influence of parasitic noise on supercapacitive sensors is investigated and compared with that on conventional capacitive sensors. Two sensors with the same dimensions based on the two sensing principles, capacitive and supercapacitive, are fabricated. Responses of each sensor in air and in water are recorded. Also, different test scenarios are created to further investigate the influence of the parasitic noise. Additionally, the sensitivity of two sensors are compared.

In Chapter 3, a new method for fabricating solid-state electrolytes based on paper

substrates coated with ionic gel is developed. Its mechanical properties are investigated through dynamic mechanical analysis and compared to a solid electrolyte without paper. The ion conductivity is investigated through electrochemical impedance spectroscopy. The microstructure of the paper-based solid electrolyte is observed using scanning electron microscope to help understand the improvement of mechanical properties that occurs by adding paper. A few different embodiments of supercapacitive force sensors are presented using the new paper-based solid electrolyte. Experiments are conducted to show the high sensitivity of the sensors and their immunity to parasitic noise.

In Chapter 4, an instrumented urethral catheter with 5 distributed supercapacitive sensors is developed for a urology application. The working mechanism of the supercapacitive sensor is presented. The design of the catheter is described in detail and followed by an introduction to the fabrication process. Four different experiments are performed to evaluate the performance of the catheter: a load cell calibration test, an ex vivo test, a cuff test, and an inside-water test. These test results demonstrate the high sensitivity and negligible parasitic capacitance of the sensor.

In Chapter 5, a simultaneous shear and normal force sensor based on supercapacitive sensing is developed. The working mechanism of the supercapacitive sensor is presented. The design of the sensor is described in detail followed by an introduction to the fabrication process. Datasets including sensor response for a wide range of applied forces are collected using a custom-designed laboratory setup and used to obtain a sensor model through machine learning. This model is used to obtain an accurate estimate of the normal and shear forces applied on the sensor based on the individual readings from the sensors. The sensitivity of the sensor to normal and shear forces are investigated respectively. An inside-water test is also conducted to show the negligible parasitic noise added to the sensor in liquid environments.

In Chapter 6, supercapacitive sensing is further explored for strain sensors using a strengthened paper-based solid electrolyte. A method of further strengthening the paper-based solid electrolyte to allow high stretchability is developed. The mechanical properties of the new strengthened electrolyte are investigated using dynamic mechanical analysis. The design and fabrication process of the strain sensor are described in detail. The response

of the sensor to increasing strain is recorded using a custom-designed laboratory setup. Then, in order to examine the sensor response to extremely small strain, a cantilever test is conducted. The test results show the high sensitivity and high range of the sensor. Possible applications of the strain sensor are discussed and demonstrated.

Chapter 2

Supercapacitive Sensors Insensitive to Parasitic Noise

2.1 Introduction

Chapter 2 aims to compare the performance of conventional capacitive sensors and the new supercapacitive sensors. As mentioned in Section 1.2, traditional capacitive sensors suffer from signifant parasitic noise when used in liquid environments or inside the human body. The parasitic noise overwhelms the force response of the sensor and makes it impossible to calculate the absolute force experienced by the sensor. In this chapter, a macro supercapacitor based force sensor that is immune to parasitic noise is developed. The supercapacitor consists of co-planar electrodes and a solid state ionic gel electrolyte on a deformable membrane. Force extertion causes deformation of the electrolyte membrane, increases its area of contact with the electrodes, resulting in a change in capacitance. A capacitive sensor of the same size is also made to compare with the supercapacitive sensor.

Capacitive sensors have the advantages of low temperature hysteresis and low power consumption [29], [31], [50], [51]. In capacitive force sensors, the force is translated into a change in the distance between two parallel-plate electrodes. By measuring the real-time capacitance between the electrodes, the force can be calculated. Figure 2-1(a) shows a

parallel plate capacitive sensor. For most of the MEMS fabricated capacitive sensors, the distance between the two electrodes is not negligible compared to the lateral dimension. The discontinuity in the material results in additional radial components in the electric field, called fringe electric field. In addition to the electric field in between the parallel plates, the device also has fringe capacitance due to the fringe electric field lines at the edges of the device. When a capacitive sensor is immersed in a liquid environment or is placed inside a human or animal body, the fringe capacitance becomes very significant due to the high dielectric constant of the surrounding medium. As shown in Figure 2-1(b), the surrounding in vivo environment causes an additional capacitance called as parasitic capacitance which can cause a large error in the relationship between force and the measured capacitance value. In fact, for a conventional capacitive sensor, parasitic capacitance in water or tissue can be several times as large as the nominal capacitance due to force [19], [52], [53]. Due to the existence of the fringe electric field around the electrodes, parasitic noise is inevitable in these conventional sensors. The value of parasitic noise on biomedical sensors can reach values in the $fF - pF$ range.

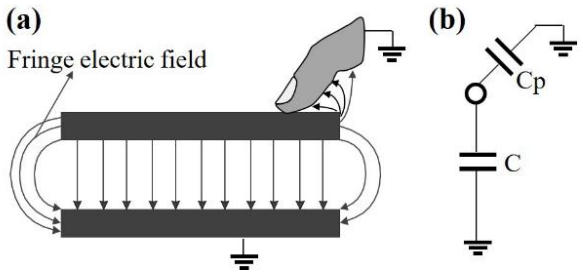

Figure 2-1 (a) Fringe electric field and parasitic capacitance on a capacitive sensor. (b) Equivalent electric circuit of a capacitor with parasitic capacitance

The error due to parasitic capacitance can be compensated by measurement of background capacitance in the liquid in the absence of loads and subsequent subtraction of this value, but this is only possible when the parasitic noise is static. In biomedical in vivo applications of the capacitive sensors, the interference from human tissues on the fringe electric field of the sensor can cause highly dynamic parasitic noise, which can greatly contaminate the sensor signal and cannot be eliminated by subtraction. In order to investigate the influence of parasitic noise on capacitive sensors and supercapacitive

sensors, two sensors of the same dimensions based on the two principles are fabricated and tested in liquid environments. The outline of the rest of this chapter is as follows: In section 2.2, the design and fabrication of the two sensors are presented. Experimental tests and results are presented in section 2.3 along with discussion of the results. Conclusions are presented in section 2.4.

2.2 Sensor Design and Fabrication

2.2.1 Design and Fabrication of a Supercapacitive Sensor

A novel solid-state supercapacitor-based force sensor that does not use liquid electrolytes is developed. A solid electrolyte film is attached to a membrane and assembled over two co-planar electrodes on the bottom substrate. A load from the top causes a deformation of the membrane and brings the electrolyte to contact the electrodes, translating the load into a change in contact area, consequently leading to a change in capacitance. The measured capacitance is utilized to estimate the applied force.

The proposed supercapacitive sensor consists of three layers which are the bottom layer with the two parallel electrodes, the spacing layer and the top layer with solid electrolyte transferred on (Figure 2-2(a)). Two gold electrodes were fabricated by first evaporating gold on the polyimide (PI) substrate and then patterning using photolithography and wet etching technique. The planar layout of the two electrodes on the same substrate makes the alignment easier during bonding. The spacing layer is made of PDMS (Polydimethylsiloxane) by molding. The solid electrolyte is essentially an ionogel, in which the ionic liquid (IL) can move freely in the matrix of a UV-curable polymer gel. An IL,1-ethyl-3-methylimidazolium tricyanomethanide [EMIM] [TCM] (IOLITEC Inc.), a prepolymer solution, consisting of PEG diacrylate (PEGDA, Mw = 575 g/mol) monomers (Sigma–Aldrich) and a photo initiator of 2-hydroxy-2-methylpropiophenone (HOMPP, Sigma–Aldrich) were mixed at a ratio of 50:40:10wt%. The mixture was drop-cast on a slide with Kapton tape defined boundaries and covered by another slide on top. Then it was put under a UV lamp (265μW/cm2) and exposed for 1min. The cured solid electrolyte film was transferred onto a clear PET (Polyethylene terephthalate) film (Dura-Lar, 0.003inch)

as the top flexible layer. For bonding, the three layers were treated with oxygen plasma first, and then a thin layer of uncured PDMS was brushed on the bonding surfaces. At last, they were pressed together and left on a hotplate at 75°C for 12hr. The sensor was fully sealed and protected from water leaking-in. The effective sensing area was 10 mm x 13 mm and the chamber formed by the spacing layer had a depth of 0.7 mm. A photograph of the as-fabricated sensor is shown in Figure 2-2(b).

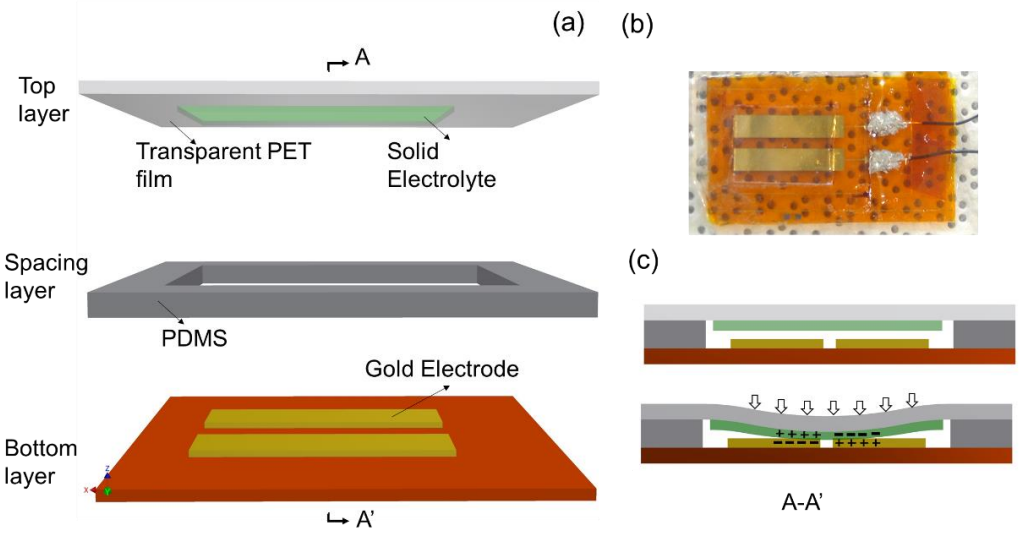

Figure 2-2 (a) Structure of the supercapacitive sensor. (b) Photograph of the as-fabricated supercapacitive sensor. (c) Illustration of sensing mechanism

2.2.2 Design and Fabrication of a Capacitive Sensor

In order to compare the supercapacitor's performance with a more traditional sensor, a conventional capacitive force sensor was also fabricated (Figure 2-3(a)).

The capacitive sensor also consists of three layers which are the bottom layer with one electrode, an insulation layer on top of the electrode, a spacing layer and a top layer with the other electrode. The copper electrodes were patterned on PI/Copper substrate (DuPont™ Pyralux® AC) using wet etching technique. On one electrode, a thin PDMS layer was brushed for insulation. The spacing layer is obtained using the same molding method as on the supercapacitor. The top and bottom layer were stacked together and aligned face to face with the spacing layer in between as shown in Figure 2-3(a). The bonding method is same as described for the supercapacitor. The as-fabricated

conventional capacitive sensor is shown in Figure 2-3(b). The dimensions of the conventional sensor are approximately the same as those of the supercapacitive sensor.

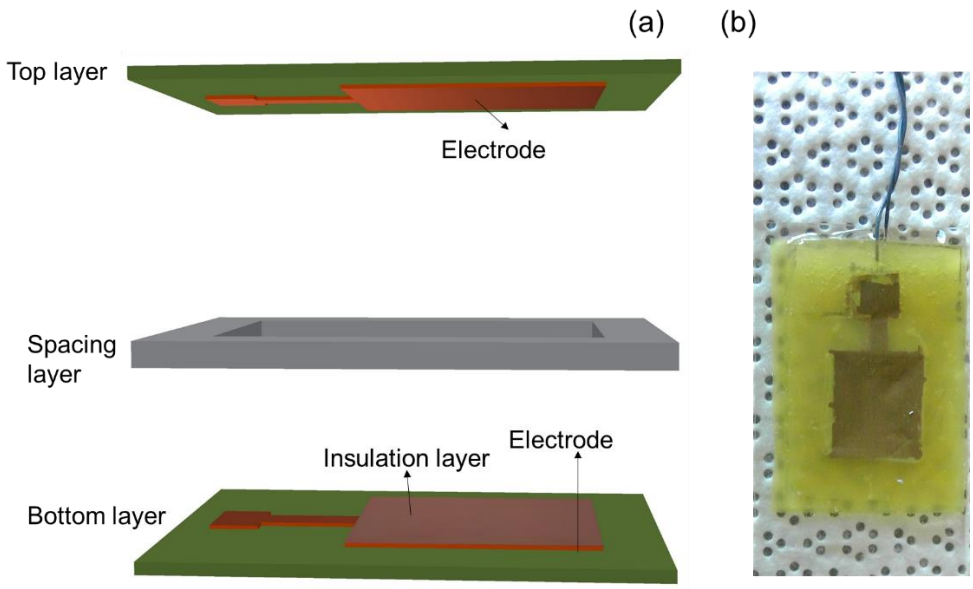

Figure 2-3 (a) Structure of the capacitive sensor. (b) Photograph of the as-fabricated capacitive sensor

2.3 Experimental Results

The two sensors were fixed to a glass slide and tested by applying forces on it using a force gauge (Handpi, Digital Force Gauge) both in air and in water. A schematic of the custom-designed experimental setup is shown in Figure 2-4. The sensor is fixed on the bottom stage, while the force gauge is installed on a translational stage over the sensor. By moving the stage down, force can be applied on the sensor from the top. The capacitance changes were recorded using a capacitance meter (Rigol 3068E). A soft rubber was put on top of the sensor to generate a distributed force. For the test in water, the whole device was immersed in water in a shallow container (Figure 2-5).

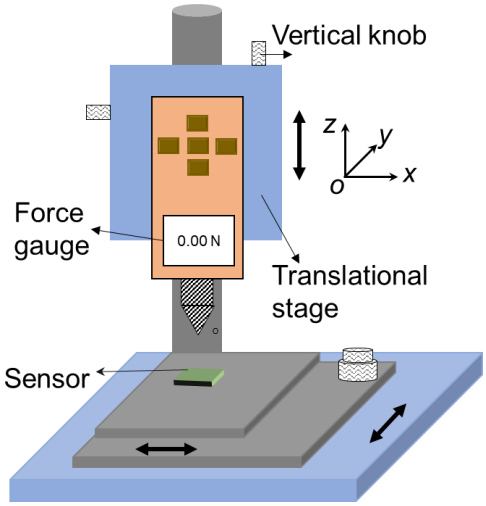

Figure 2-4 Schematic of the experimental setup

The normal force from water is negligible (less than 0.01N). The test results for the supercapacitive sensor are shown in Figure 2-6. As the force increases, the contact area between the solid electrolyte and the electrodes underneath increases, resulting in a change in capacitance. The sensitivity of the supercapacitive sensor is around $0.13\mu F/N$. In comparison of the response in air and water, there isn't any obvious capacitance change due to operation inside water. In other words, the sensor has negligible parasitic capacitance.

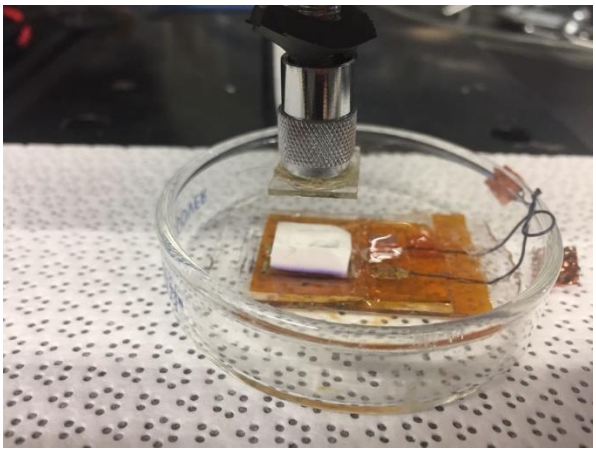

Figure 2-5 Supercapacitive sensor tested in water

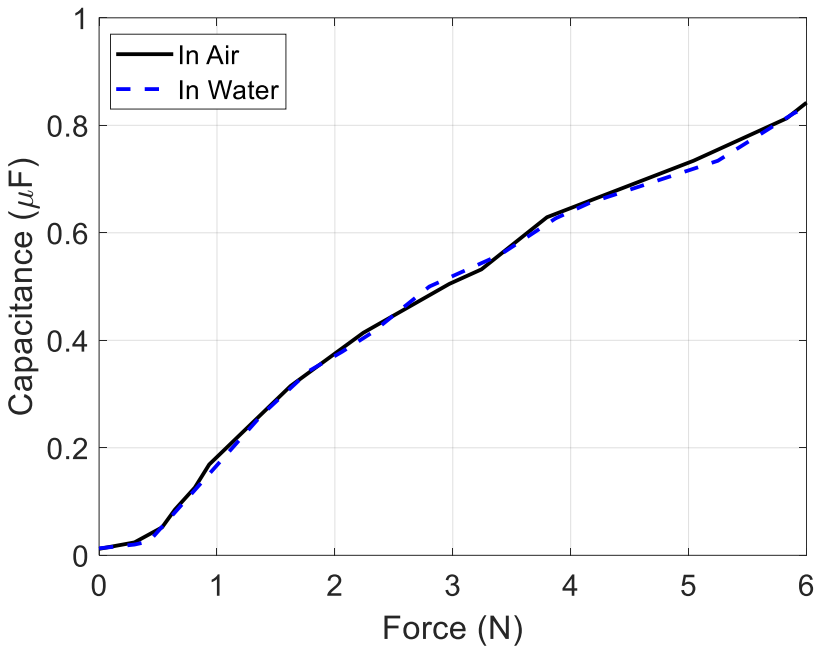

Figure 2-6 Response of supercapacitive sensor to applied force in air and in water

The same test procedure is conducted on the traditional capacitive sensor. The results for the traditional capacitive sensor are shown in Figure 2-7. As the force increases, the distance between two electrodes decreases, thus increasing the capacitance. The sensitivity of capacitive sensor is approximately 0.3pF/N which is much lower than that of the supercapacitive sensor. More importantly, after immersion in water, the capacitance of the sensor increases by as much as 50%, which is caused by parasitic noise. A huge offset in measured capacitance can be seen in Figure 2-7 between the in-water and in-air values.

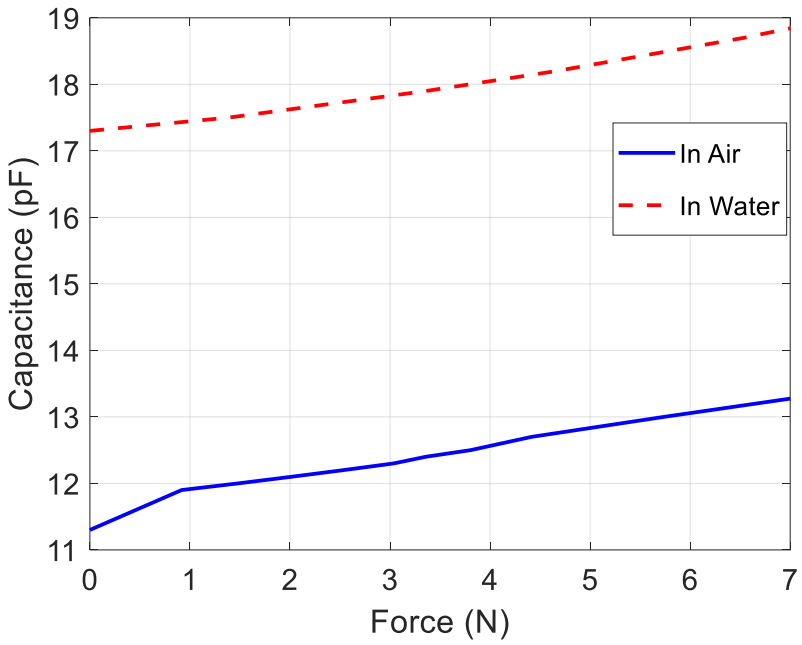

Figure 2-7 Response of traditional capacitive sensor to applied force in air and in water

A larger range of forces is shown in Figure 2-7 because of the lower sensitivity of the sensor. Both sensors had the same operating range of force measurement.

In order to further investigate the different influence of parasitic capacitance on the supercapacitive sensors and capacitive sensors, the two sensors were also tested in four additional scenarios as described below:

Scenario 1: A steel tweezer was placed over the sensors (1-2mm away from the top of the sensor)

Scenario 2: A human finger was used to approach the sensors (1-2mm away from the top of the sensor)

Scenario 3: The two wires which collect current from the two electrodes were untwisted.

Scenario 4: The sensors were placed inside extracted real sheep tissues. (The tissues were carefully wrapped around the sensor to make sure no pressure is applied on the sensing area, but the sensor itself is enclosed by the tissue).

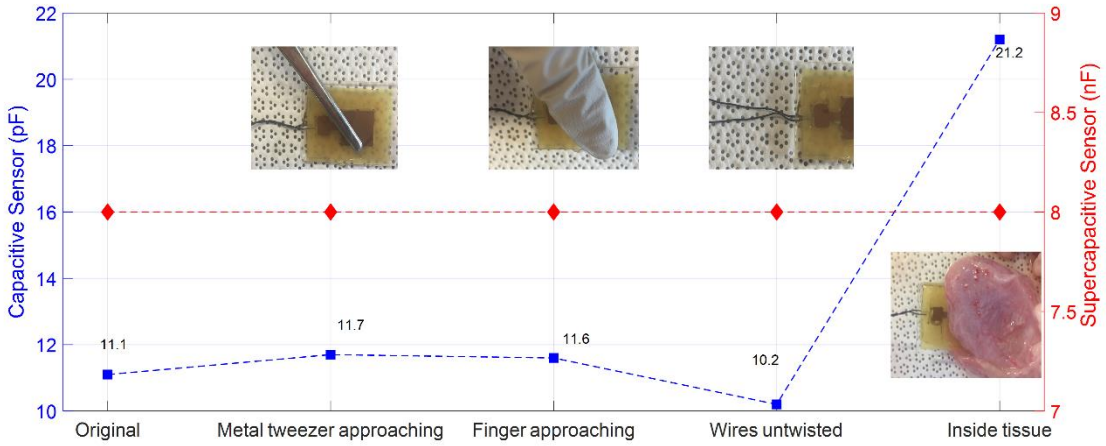

Figure 2-8 Four test scenarios to investigate the influence of parasitic noise

The results from the four scenarios are shown in Figure 2-8. As shown in the figure, when a finger approaches or a metal tweezer is moved close to the traditional capacitive sensor, its capacitance increases significantly, which means an additional parasitic capacitance is created in these two scenarios. That makes the sensor sensitive to interferences and limits its use in many circumstances. Besides, the capacitance of the traditional sensor became smaller after the wires were untwisted. The parasitic noise from the wires is not negligible, since the capacitance of the conventional sensor is low. When put inside the real sheep tissues, the capacitance jumped to nearly twice of the original capacitance. That limits the in vivo use of capacitive sensors, like in biomedical applications. However, in case of the supercapacitive sensor, the capacitance remained the same in all four scenarios, with no change whatsoever.

2.4 Conclusions

A novel solid-state supercapacitor-based force sensor has been developed and successfully fabricated using an ionic gel solid electrolyte and planar electrodes. Also, a similarly sized conventional capacitive sensor was fabricated to compare its performance with that of the supercapacitive sensor. Tests have been conducted on these two sensors in air and in water, as well as in other typical use scenarios. Results show that while the conventional capacitive sensor suffers significantly from parasitic noise and has

significantly lower sensitivity, the new supercapacitor-based force sensor is completely immune from parasitic capacitance. Furthermore, its force sensitivity of 0.13μF/N exceeds the 0.3 pF/N sensitivity of the conventional capacitive sensor by 6 orders of magnitude! This indicates that the supercapacitor-based sensor could be highly suitable for biomedical in-vivo applications. In the following chapters, the supercapacitive sensor is miniaturized, further improved using a novel paper-based electrolyte, and then applied for in vivo use in multiple real-world applications.

Chapter 3

Flexible Solid-State Paper-Based Electrolyte for Supercapacitive Sensors

3.1 Introduction

In this chapter, a flexible solid-state paper-based electrolyte is developed with excellent mechanical and electrical properties and offering unprecedented configurability for use in sensor embodiments.

Paper offers multiple advantages as a substrate material for sensors: it is ubiquitous, low cost, light weight and biodegradable [54]. Paper-based sensors would be especially valuable for health care diagnostics in developing countries and for other similar cost sensitive applications [55]. Recently, researchers have developed paper-based sensors, which could provide highly inexpensive microfluidic devices [56], [57] and portable bio-assays [58]–[60] for detecting analytes in point of care health diagnostics. Devices fabricated from paper also include respiration analysis sensors [61], textile sensors [62], capacitive touch sensors [63] and microelectronics [55], [64]. Paper is porous and made up of a network of cellulose fibers, which offers unique structural properties. It is naturally hydrophilic and readily absorbs aqueous liquids that spread inside the paper through capillary flow within its fiber matrix [65]. The cellulose fibers can also be functionalized, thus tuning their properties such as hydrophilicity, if desired, as well as their permeability

and reactivity [66]. As a result, fabrication methods for paper-based sensors are extremely flexible, ranging from cutting, wax printing, screen printing, and analogue plotting to photolithography, inkjet printing and etching, plasma treatment, flexography printing, and laser treatment. [65], [67]–[69] Although tremendous progress has been made on paper-based sensors, the use of paper as a substrate for mechanical sensors is in its preliminary stages. Some pioneering work in this area include piezoresistive force sensors based on a carbon resistor patterned on paper [70], and resistive strain gauges on paper [71], [72]. Although these sensors can be very quickly fabricated and are highly inexpensive, their range of measurement is typically small, extending only up to 16mN for force sensors [70] and a maximum of 1.2% extension for strain sensors. These metrics compare poorly with the large range of traditional microelectromechanical system (MEMS) sensors.

To overcome this limitation, in this chapter a new fabrication method and sensing mechanism for paper-based mechanical sensors is presented that enable them to outperform MEMS sensors on both sensitivity and range. The new paper-based sensors retain their low-cost advantage and can be quickly fabricated in a matter of minutes with no need for cleanroom facilities. Hence, these new sensors can have broad applications in several industrial and bio-medical contexts. The large range and high sensitivity of our paper-based sensors arise from the principle of supercapacitive sensing.

As discussed in Chapter 1, liquid-state supercapacitive sensors have several inherent disadvantages, which limit the broad use of these sensitive sensors:

(I) The sensor cannot be easily miniaturized to create micro-sensors, since it is difficult to create size-controlled micron-sized droplets or liquid pool and to trap the liquid inside a sealed sensor;

(II) The presence of the hydrophobic coating on the surface of the electrodes reduces the capacitance, because it increases the distance between the electrolyte and the electrode;

(III) Even in large-sized sensors, each sensor needs to be individually calibrated to account for variability in liquid size and location inside the sensor chamber;

(IV) The high cost of the hydrophobic coating and the large size of the sensor pose problems in creating a sheet of such sensors for measuring distributed forces

(e.g. forces from the foot of a patient as he/she walks);

(V) The shelf life of liquid-state sensors is short due to atmospheric evaporation.

(VI) The effect of gravity on the liquid may limit their application in systems involving non-planar motion.

In this chapter, functionalized paper is used as a substrate for making highly flexible solid-state electrolytes in supercapacitive force sensors, which helps address all of the above limitations of current supercapacitive sensors. The new electrolytes are made by introducing active materials into the porous matrix of paper and functionalizing the entire thickness of the paper. The deformation of the electrolytes in response to an applied force and the resulting change in its contact area with the electrodes can then be used to sense the applied force. In addition to the electrolyte, the entire sensor can also be made from paper substrates resulting in a simple and quick fabrication process.

In Section 3.2, the fabrication of the novel paper-based solid electrolyte is presented. In Section 3.3, the properties of the paper-based solid electrolyte including mechanical properties, ion conductivity, and micro-structures are studied and compared with an ionic gel electrolyte. In Section 3.4, multiple embodiments of the paper-based supercapacitive force sensors are discussed in detail including the design of the sensors and their performance.

3.2 Solid Electrolyte for Supercapacitive Sensors

A highly flexible solid-state electrolyte with a significant capability for deformation is essential for supercapacitive mechanical sensors. The basic requirements for the electrolyte include:

(1) Excellent mechanical properties with high flexibility and toughness to provide high sensitivity and high sensing range

(2) Excellent electrical properties to provide good ion mobility

(3) Easy fabrication process

(4) Low cost

A paper-based electrolyte is fabricated in this chapter by mixing an ionic liquid with a

photo-curable polymer, brushing this ionic mixture on to filter paper, and then exposing the combination to UV light for a short time duration (1 minute). The new paper-based solid electrolyte meets all the requirements listed above. Also, in this section, an ionic gel solid electrolyte is fabricated to compare with the paper-based solid electrolyte.

3.2.1 Ionic Gel Solid Electrolyte

Ionic-gel electrolytes that incorporate ionic liquid into a cross-linkable polymer matrix provide both mechanical stability and high electrical conductivity [73]–[78]. Figure 3-1 shows the facile fabrication process of the ionic gel electrolyte. An ionic liquid (IL),1-ethyl-3-methylimidazolium tricyanomethanide [EMIM][TCM] (IOLITEC Inc.), a prepolymer solution, consisting of PEG diacrylate (PEGDA, Mw = 575 g/mol) monomers (Sigma–Aldrich) and a photo initiator of 2-hydroxy-2-methylpropiophenone (HOMPP, Sigma–Aldrich) are mixed in the ratio of 5:4:1 by weight by sonicating. The mixed gel is drop-cast on to a mold, covering the mold with a piece of glass slide, and exposing under UV light for 1 min. The polymer inside the gel crosslinks into long chains forming a network (Figure 3-2). The ionic gel consists of a conductive IL, which provides the desired electrical conductivity, and a prepolymer solution, which is photo cross-linkable and offers the structural integrity [79].

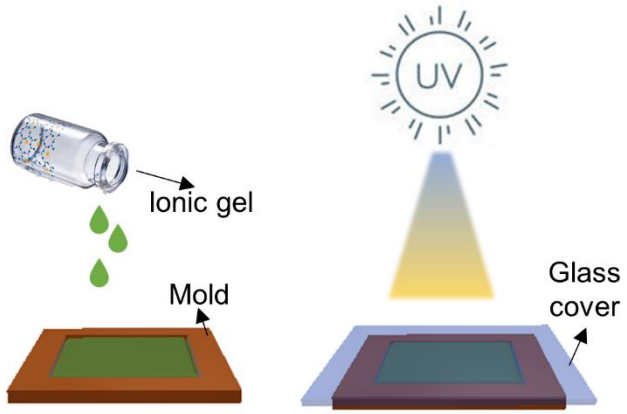

Figure 3-1 Fabrication process of an ionic gel electrolyte without filter paper

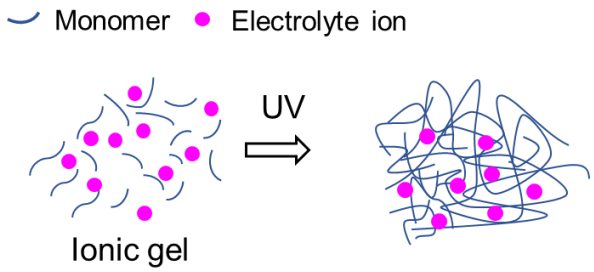

Figure 3-2 Crosslinking process of the ionic gel

However, a traditional ionic gel has very limited flexibility. A piece of the as-fabricated ionic gel solid electrolyte is shown in Figure 3-3. The ionic gel electrolyte cracks while it is being bent while the alternate paper-based solid electrolyte can be bent and completely folded without mechanical failures. Besides, the original ionic gel electrolyte is usually used in the form of a thin film, and a mold is needed to make the film. In order to use a solid-state electrolyte for supercapacitive sensing, good mechanical properties, ease of fabrication with desirable shapes, the ability to form good electrode/electrolyte contact, and high ionic conductivity are essential characteristics. The poor mechanical properties of the ionic gel solid electrolyte limit its application as a sensing element in supercapacitive sensors which require a large sensing range.

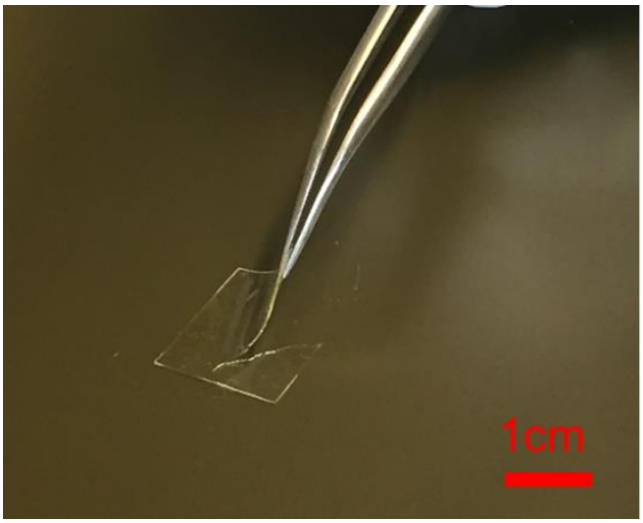

Figure 3-3 Limited flexibility of the ionic gel solid electrolyte

3.2.2 Paper-based solid electrolyte

A paper-based solid electrolyte is developed here by incorporating paper into the ionic

gel. The filter paper used to make this electrolyte is shown in Figure 3-4. An IL,1-ethyl-3-methylimidazolium tricyanomethanide [EMIM][TCM] (IOLITEC Inc.), a prepolymer solution, consisting of PEG diacrylate (PEGDA, Mw = 575 g/mol) monomers (Sigma–Aldrich) and a photo initiator of 2-hydroxy-2-methylpropiophenone (HOMPP, Sigma–Aldrich) are mixed in the ratio of 5:4:1 by weight by sonicating. The mixed gel is then brushed on to the filter paper (MF-Millipore, HATF, 0.45um). The filter paper can be pre-shaped to achieve different geometries. After 1 min under UV exposure, the flexible solid paper-based electrolyte is obtained. It should be noted that the ratio of the components can be changed to achieve solid electrolytes with different mechanical properties.

Figure 3-4 Cellulose filter paper used to make solid electrolyte

Figure 3-5 compares the flexibility of the ionic gel electrolyte and the paper-based solid electrolyte. By brushing the ionic gel on to filter paper before cross-linking, the mechanical properties are improved. The new paper-based solid electrolyte meets all the requirements listed at the beginning of this section.

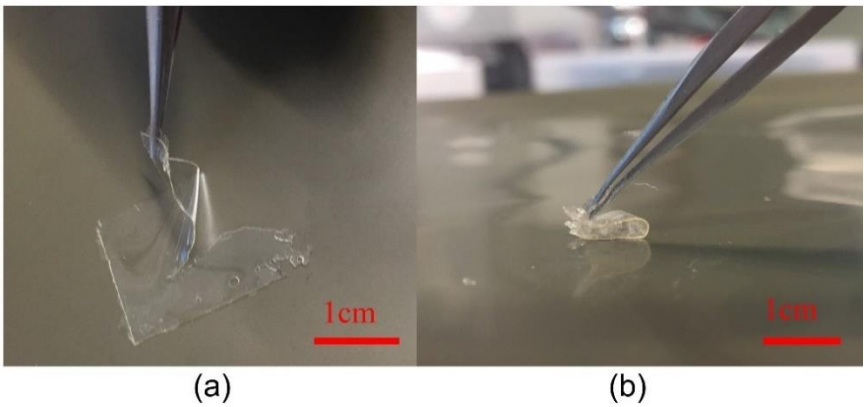

Figure 3-5 (a) Failure of an ionic gel electrolyte without filter paper under bending. (b) Significantly higher flexibility of a paper-based electrolyte.

Due to the softness and flexibility of the paper-based electrolyte, it can be easily shaped into complex geometries, which is hard, if not impossible, to achieve with the original ionic gel electrolyte. Figure 3-6 shows some examples of electrolyte geometries created from the paper-based electrolytes, including a hollow cylinder, an arch, a ring, a corrugated element, a dome and a spiral. These geometries result in electrolyte structures with ultra-low stiffness, which is favorable when incorporated in supercapacitors. Such supercapacitors can deform significantly by force with dramatically increasing contact areas.

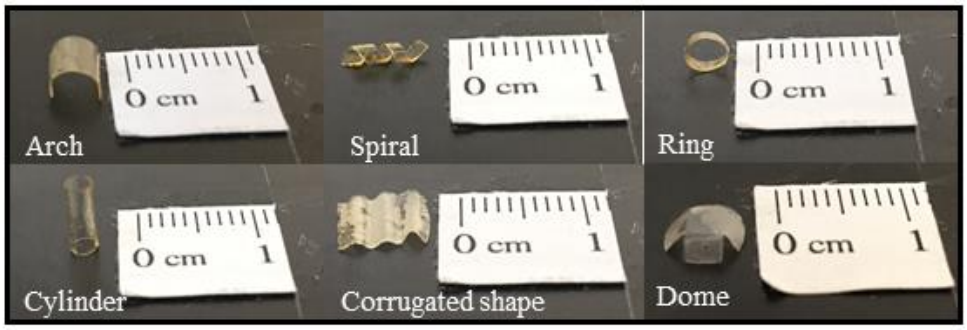

Figure 3-6 Different configurations of the paper-based solid electrolyte

3.3 Properties of Paper-Based Electrolytes

The properties of the paper-based electrolyte are investigated using multiple technologies and compared with the properties of the ionic gel solid electrolyte.

3.3.1 Mechanical Properties

Thin films of ionic gel electrolytes and paper-based electrolytes were stretched under tensile forces using dynamic mechanical analysis (DMA, RSA G2, TA Instruments) (Figure 3-7) and their stress-strain curves were obtained, as shown in Figure 3-8. In comparison with the ionic gel electrolyte, the ultimate tensile strength (maximum stress before failure) of the paper-based electrolyte is 50% larger, the toughness 3.55 times higher and the maximum elongation strain 2.5 times larger. To further characterize the flexibility of the two electrolytes, Figure 3-9 compares the Young's modulus of the ionic gel and paper-based electrolytes under cyclic tensile loads at low frequencies. The Young's

modulus of the paper-based electrolyte is only about the half of the Young's modulus of the ionic gel electrolyte. Therefore, compared to the original ionic gel electrolyte, the paper-based electrolyte is softer, tougher and more flexible. The mechanical properties of the ionic gel electrolyte and the paper-based electrolyte are summarized in Table 3-1.

Figure 3-7 DMA test setup

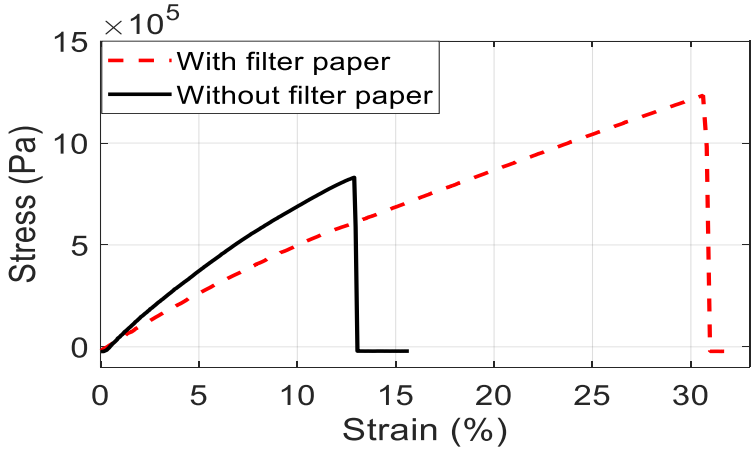

Figure 3-8 Stress-strain curves of an ionic gel electrolyte and a paper-based electrolyte

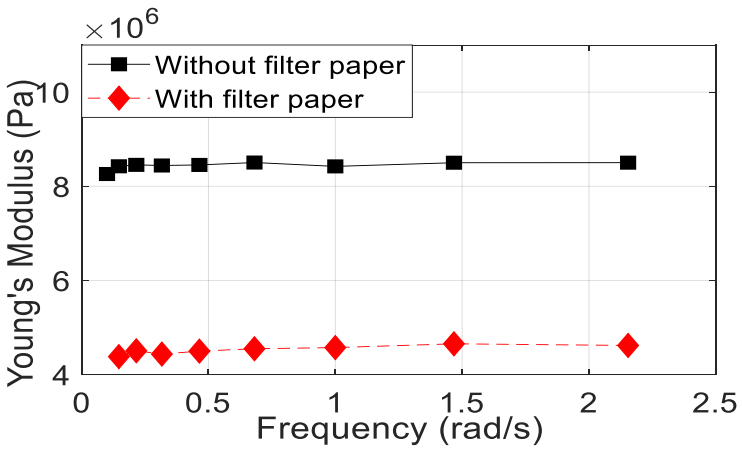

Figure 3-9 Young's modulus of an ionic gel electrolytes and a paper-based electrolyte under tensile cyclic loads at low frequencies

Table 3-1 Mechanical properties of an ionic gel electrolyte and a paper-based electrolyte

	Ionic gel electrolyte	**Paper-based electrolyte**
Young's Modulus (MPa)	8.4	4.6
Ultimate tensile strength (MPa)	1.28	3.06
Toughness (N/m^2)	$5.8x10^6$	$20.1x10^6$
Configurability	Thin film	Various geometries: arch, cylinder, spiral, etc.

When brushing the ionic gel onto the filter paper and exposing the filter paper to UV, two processes happen:

(I) The dissolution of the paper fibers in the ionic liquid;

(II) The crosslinking of the polymer.

Ionic liquids are good solvents for cellulose [80], [81]. The filter paper used is full of well-distributed microstructures as shown in Figure 3-10, micro-sized cellulose fibers forming micro-sized pores. When the ionic gel mixture is coated on paper, it takes the shape of the filter paper, first filling the porous paper matrix and then slowly dissolving the paper over a period of approximately 25 minutes as shown in Figure 3-11.

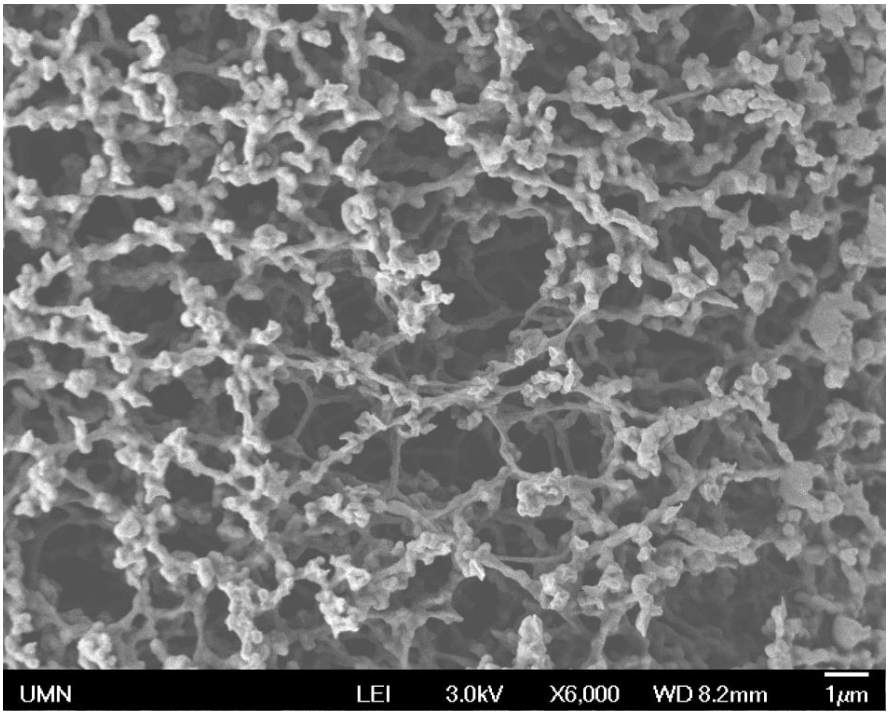

Figure 3-10 SEM image of the filter paper

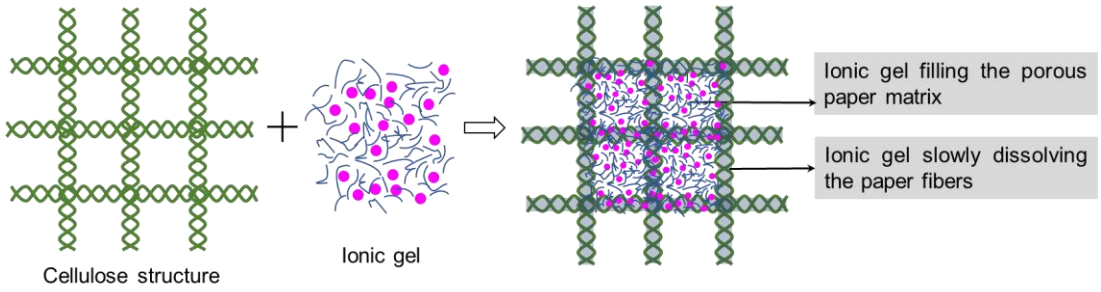

Figure 3-11 Fabrication process of the paper-based solid electrolyte

The dissolution time of the filter paper for Process II in the ionic gel without cross-linking is directly measured as shown in Figure 3-12. Right after brushing the gel onto the filter paper it starts turning transparent, but the shape of the filter paper remains. The filter paper dissolves slowly. At around 9 minutes after applying the gel, the electrolyte arch starts to collapse. After about 25 minutes, the arch shape collapses. Nevertheless, the edge of the paper stays. After 1 hour, the filter paper totally dissolves in the gel, loses its original shape and becomes a pool of gel without a definite shape. Hence, the dissolution time is more than 25 minutes, but less than 60 minutes. In contrast, Process I, the cross-liking under UV exposure takes 1 minute. The separation of these two-time scales explains the

two key features of the paper-based electrolytes, i.e., the retaining of the electrolyte shape to conform to that of the paper substrate and the creation of micron-sized fissures that leads to the high flexibility.

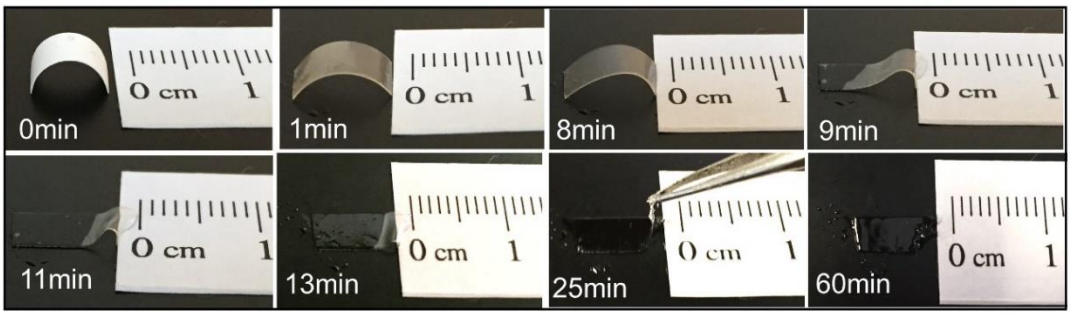

Figure 3-12 Photographs showing the dissolving of filter paper in ionic gel. Cross-linking does not occur in this process

Since the curing time for the ionic gel in the paper substrate (1 minute) is much less than the time taken for the paper to dissolve (25 minutes), the original shape of the paper substrate is retained by the ionic gel. The paper itself eventually dissolves, leaving a clear transparent and flexible ionic gel electrolyte. Because the original paper substrate can be cut, rolled, folded and shaped into various three-dimensional (3D) geometries, the electrolyte can also be easily made into different complex 3D shapes.

Microstructures of the ionic gel electrolyte and the paper-based solid electrolyte are further investigated to explain why the addition of cellulose improves the mechanical flexibility properties. Scanning Electron Microscope (SEM) images of the cross-sections of the paper-based electrolytes show micron-sized fissures, creating a network with many wrinkles as shown in Figure 3-13. In comparison, these fissures and wrinkles cannot be found in the cross-section of the ionic gel electrolytes without filter paper (Figure 3-14). The fissures are vestiges of the fiber structures of the filter paper. The bulk of the material consists of PEG diacrylate (PEGDA), the cross-linked polymer with ionic gel. But the portions that contained cellulose fibers are filled with a softer material. Cellulose fibers get dissolved by the ionic gel into low molecular weight residues [82], [83]. A strong hydrogen-bonding interaction occurs between PEGDA and the dissolved cellulose molecules [84]. This weakens the crystallinity of PEGDA resulting in an improvement in the softness and extensibility properties of the [84], [85]. In short, the bulk of the material

is the more-brittle PEGDA while the fissures are soft due to dissolving of the cellulose fibers in those locations. The fissures or wrinkles allow for greater compressibility and provide lower stiffness. Figure 3-13 (b) shows a zoomed-in view of the wrinkles in the paper-based electrolytes. The size of the fissures is about 100 – 200 nm, matching well with the characteristic size of the cellulose fiber structure in the filter paper (Figure 3-10).

The flexibility of the paper-based electrolytes comes from micro-wrinkles created by the slow dissolving in ionic gel of filter paper fibers. The dissolution process takes significantly longer time than the crosslinking process, so the shape of electrolytes determined by the initial filter paper substrate remains. The crosslinking of the polymer occurs on a barely dissolved structure and fills in the porous holes of the fiber structure of the filter paper. Therefore, the ionic gel takes a similar structural shape as that of the filter paper. The cellulose fibers in the filter paper eventually dissolve after a sufficiently long time, leaving the submicron fissures of the wrinkle structure. Thus, the key for the formation of the wrinkle structure is the separation of the time scales of the cross-linking and dissolution processes.

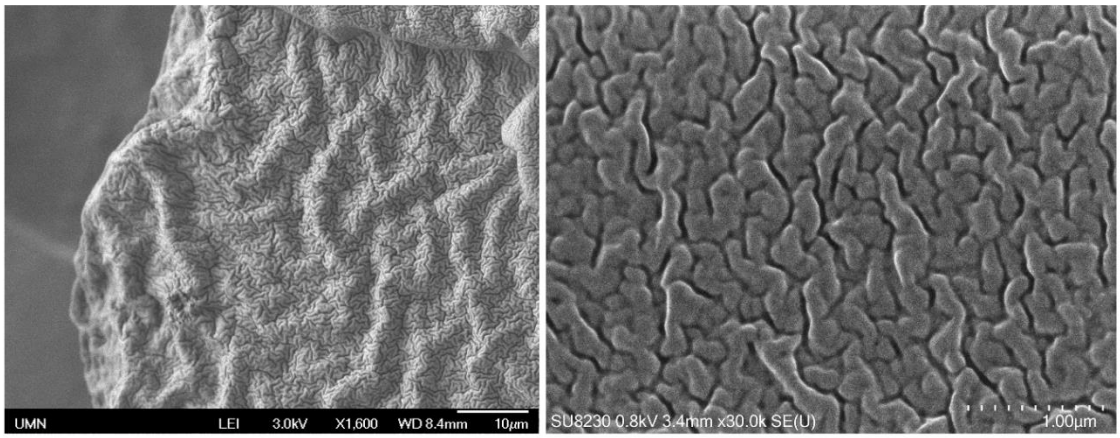

Figure 3-13 (a) SEM image of the cross-section of a paper-based electrolyte. (b) Zoom-in view of the micron-sized wrinkles of the paper-based electrolyte.

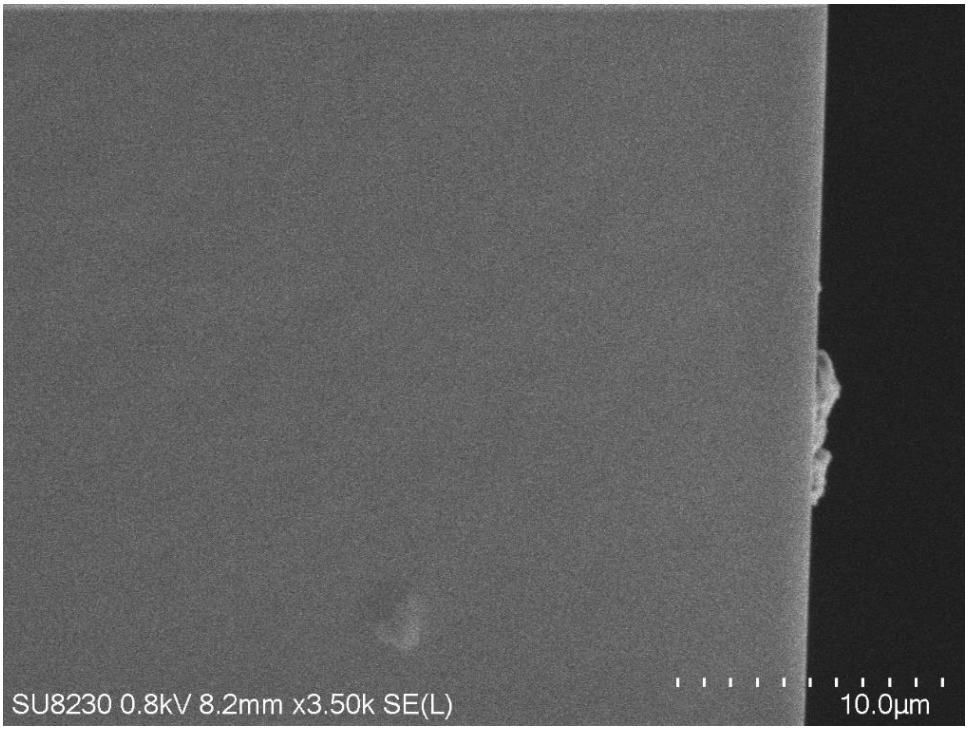

Figure 3-14 SEM image of the cross-section of an ionic gel electrolyte.

In summary, the high flexibility of the new electrolyte arises from the mechanical properties of the microstructure created by dissolution of the cellulose structure of the filter paper in the gel matrix. This highly flexible electrolyte makes possible the development of supercapacitive sensors, which incorporate significant bending or deformation as a part of the sensing mechanism.

The paper-based electrolyte can be further strengthened by adding nanoparticles to the ionic liquid. This will be discussed in Section 6.3.

In order to further understand what happens inside the filter paper after the ionic gel is brushed onto it, the ionic gel was diluted using water (IL: PEG: PI: H2O = 5:4:1:20). The diluted mixture was brushed onto the filter paper. Different from the undiluted mixture being brushed onto the filter paper, the filter paper does not turn transparent immediately. Instead, a light white colored film is obtained. This film was exposed under UV light for 1 min, and then placed on a hot plate (60 °C) for 10 mins to evaporate the water inside. A small piece from the film is cut and the cross-section is observed under SEM.

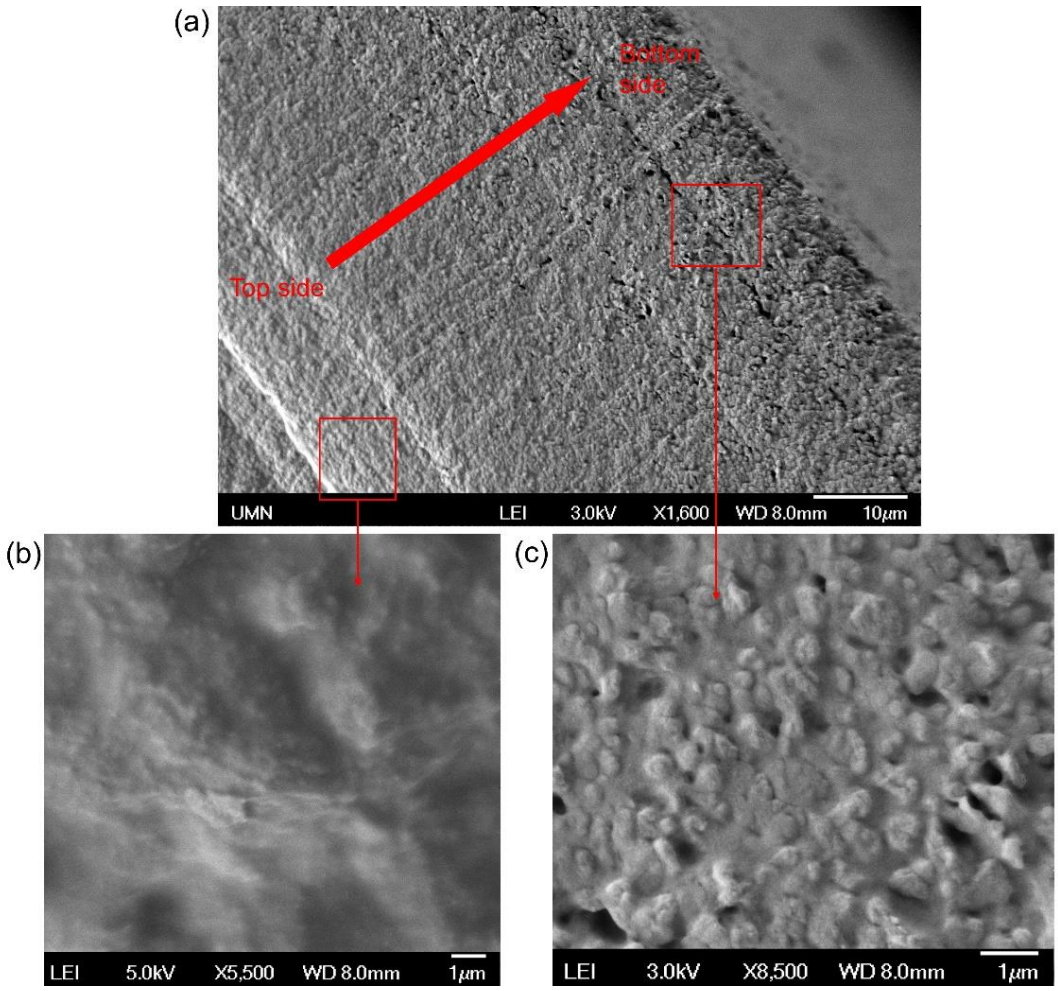

Figure 3-15 SEM images of the paper-based electrolyte film made using diluted ionic gel. (a) depth-varying cross-section of the paper-based electrolyte made by paper being dissolved in diluted ionic gel. (b) zoom-in view of the cross-section near the top side. (c) zoom-in view of the cross-section near the bottom side

Figure 3-15 shows an SEM image of the cross-section of the film. From Figure 3-15 (a), it can be seen that the density of the structure changes gradually. That's because the mixture was brushed on the top side of the filter paper, and partially percolated to the bottom side. As a result, the extent of dissolution of the filter paper in the ionic gel varies from high to low. The section near the bottom side (shown in Figure 3-15(c)) kept the porous structure of filter paper, while near the top side (Figure 3-15(b)), the network of the filter paper has been filled with the crosslinked polymer with ionic liquid inside. Later, the fibers in the filter paper will dissolve and wrinkles will be created in the cross-section.

3.3.2 Electrical Properties

The ion conductivity of the paper-based solid electrolyte is investigated using electrochemical impedance spectroscopy (EIS, Autolab PGSTAT302N, Figure 3-16). An electrochemical cell is made for this test including two gold electrodes patterned on the bottom substrate and a paper-solid electrolyte film cured on top of the electrodes. The EIS data was collected as real (Z') and imagery (Z") components of the complex impedance by scanning from 10Hz to 1MHz. The impedance raw data plot is shown in Figure 3-17. The ionic conductivity of the polymer electrolyte film can be determined from the plot by fitting to a simple equivalent circuit shown in Figure 3-18 [86]. The bulk electrolyte polarization and resistance to ion motion are represented as the parallel combination of a constant phase element (CPE), which captures the dielectric relaxation and distribution within the bulk polymer electrolyte, and resistance (R_b) respectively. C_i describes the interface polarization and double layer formation, while R_i is the lead resistance. In the impedance plot, R_b and CPE are represented as a depressed semicircle at high frequency, with R_b being the diameter. Nonlinear least squares fitting method was used to estimate R_b at high frequency. The fitted semicircle is plotted with red dashed line in Figure 3-17. After that, the ionic conductivity (σ) can be obtained using the following equation:

$$\sigma = \frac{L}{R_b A} \tag{3-1}$$

where L is the traveling length of the ions, and A is the area of the electrolyte cross-section. The electrolyte film was transferred on to two Au electrodes (2mm×1mm) with a gap of 0.5mm. The ion conductivity is estimated to be $3 \times 10^{-4} S/cm$, which enables us to achieve a performance level close to that of the liquid electrolyte-base device [87].

Figure 3-16 EIS instrument - Autolab PGSTAT302N

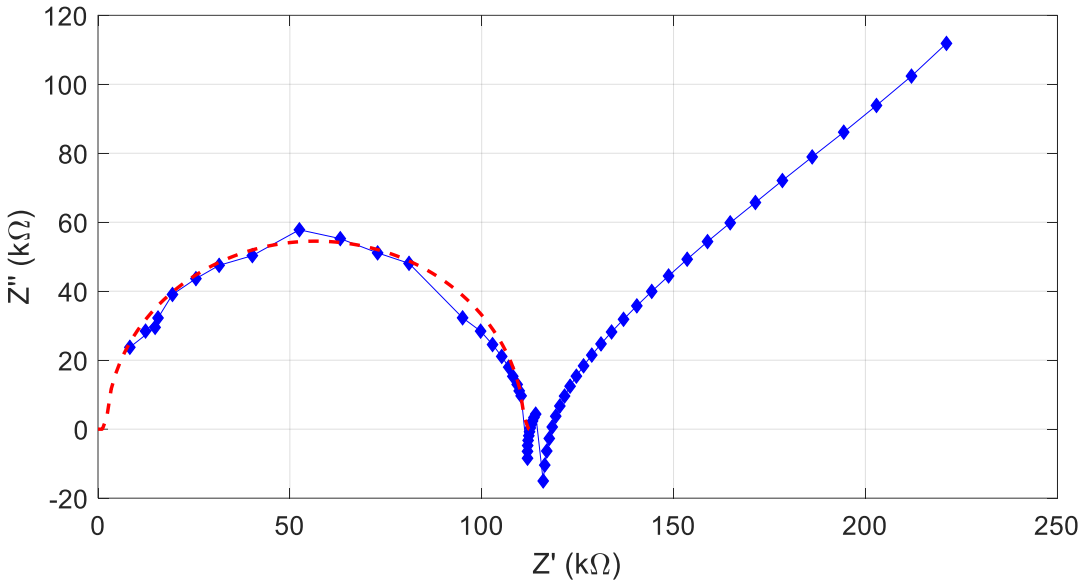

Figure 3-17 Complex impedance plot

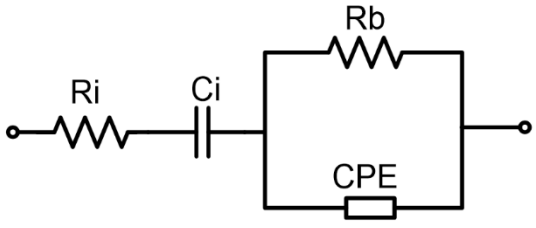

Figure 3-18 Equivalent circuit of the EIS testing cell

3.4 Embodiments of Paper-Based Supercapacitive Force Sensors

The new flexible paper-based electrolytes enable rapid fabrication of many different configurations of supercapacitive force sensors. The fabrication process is easy, inexpensive and highly adaptable to various applications. A few embodiments using different geometries of paper-based electrolytes are presented below to illustrate the versatility of the sensors.

3.4.1 Design of the Paper-Based Supercapacitive Force Sensors

Figure 3-19 shows a prototype force sensor with a corrugated electrolyte element. In addition to its use in fabrication of the electrolyte, paper is also used as the structural material for both the top and bottom panels. When load is applied on the top layer, the corrugated electrolyte deforms, resulting in an increase in the contact area with the bottom copper tape electrodes, thus causing an increase in capacitance. The sensor is made using copper tape as the electrode material, and regular office paper as the structure material.

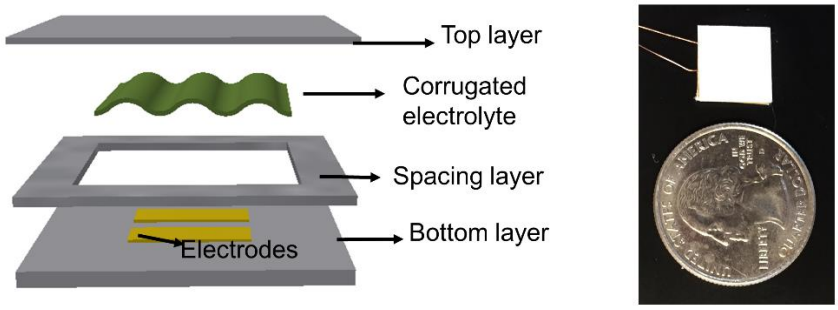

Figure 3-19 Schematic (left) and photograph (right) of a force sensor made of a corrugated electrolyte.

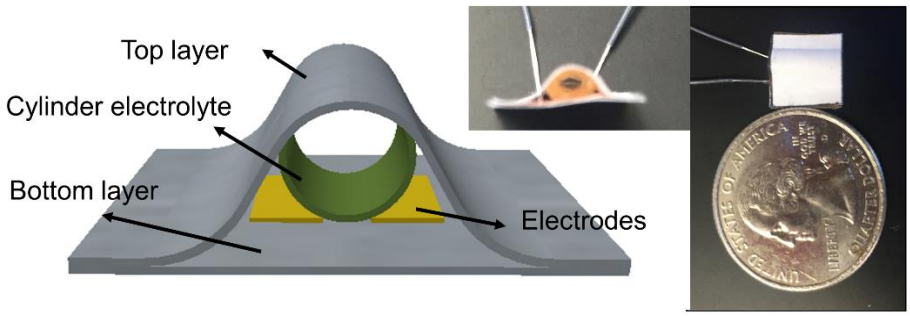

Figure 3-20 Schematic (left) and photograph (right) of a force sensor made of a hollow cylindrical electrolyte.

Figure 3-20 shows a prototype force sensor using an elastic paper-based rolled up electrolyte. The sensor consists of a planar set of two copper electrodes on a paper substrate and a rolled up hollow cylindrical electrolyte placed on top of the electrode pair. Due to the cylindrical electrolyte being hollow, it deforms easily under force and the contact area increases with the shape changing from circular to elliptical. The copper electrodes were made by simply using adhesive copper tape and fixing them on the bottom sheet of paper.

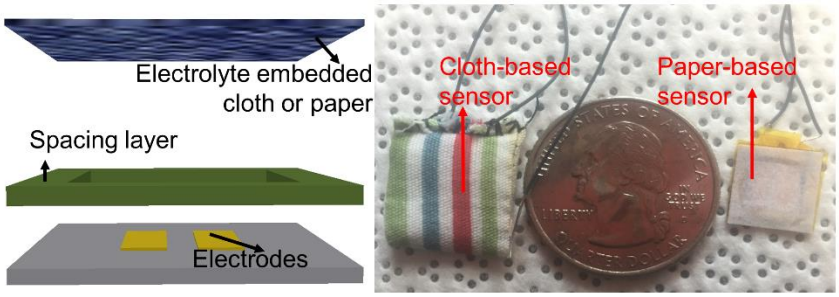

Figure 3-21 Schematic (left) and photograph (right) of force sensors made with cloth-based and paper-based electrolytes

Figure 3-21 shows prototypes of cloth-based and regular-paper-based sensors. The supercapacitive sensors can be fabricated not only using filter paper, but also by using regular printing paper and even cloth. With regular paper and cloth, the dissolution of the fiber structure happens only to a partial degree. Figure 3-21 shows two prototypes of the supercapacitive force sensors, in which the ionic gel is brushed onto regular paper and cloth. The paper and cloth are partially dissolved, and the rest of the substrate structure holds the ionic gel, which can then be used as the electrolyte of supercapacitive force sensors. The sensors are made simply by sewing or gluing together two sheets of cloth/paper. The

electrolyte is then brushed onto the top cloth/paper sheet. The two parallel copper tape electrodes are on the bottom sheet of cloth/paper.

The regular-paper-based supercapacitive sensors are also made into a 4 by 4 sensor matrix, which can be used to measure the distribution of force, as shown in Figure 3-22. One example application for such an array of sensors is a shoe insole force sensor, which can provide the force distribution of human foot. All the sensors above are easy to fabricate. Copper tapes are used as electrodes, and regular paper as the structure material. This provides an option of inexpensive, disposable force sensing for medical care.

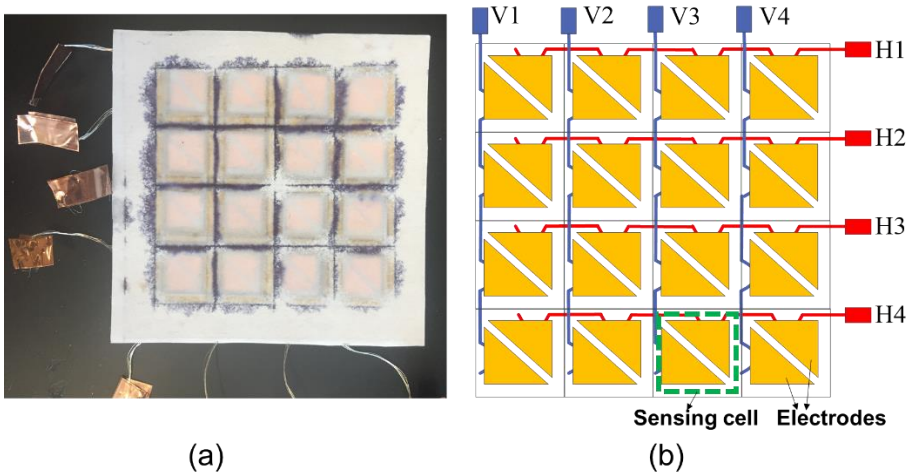

Figure 3-22 (a) 4x4 array of paper-based supercapacitive sensors. (b) Bottom electrodes

3.4.2 Performance of The Paper-Based Supercapacitive Sensors

The sensitivity of our paper-based supercapacitive sensors depends on the size and configuration of the sensors, ranging from several nF/N to several $\mu F/N$. In contrast, typical sensitivities of traditional MEMS capacitive sensors are on the order of pF/N[88], [89]. Figure 3-23 shows the capacitive response to applied forces for the supercapacitive sensor made of the corrugated electrolyte (Figure 3-19). The sensitivity of the sensor is approximately $20nF/N$. A similar sensitivity can also be obtained for the cloth-based sensor (Figure 3-24). The $20nF/N$ sensitivity of the paper-based supercapacitive sensors is more than 1000 times higher than that of traditional MEMS capacitive sensors [88], [89]. The range of measurement of the sensors depends on the design of the sensors. The paper-based sensor of Figure 3-21 can measure up to a maximum force of around 222.4 N

(50 lbs).

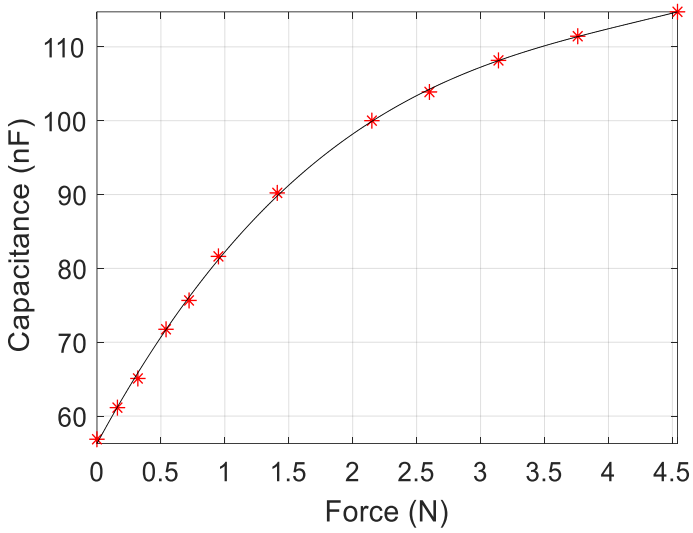

Figure 3-23 Force response curve of the corrugated electrolyte sensor with an ultra-high sensitivity of 20nF/N

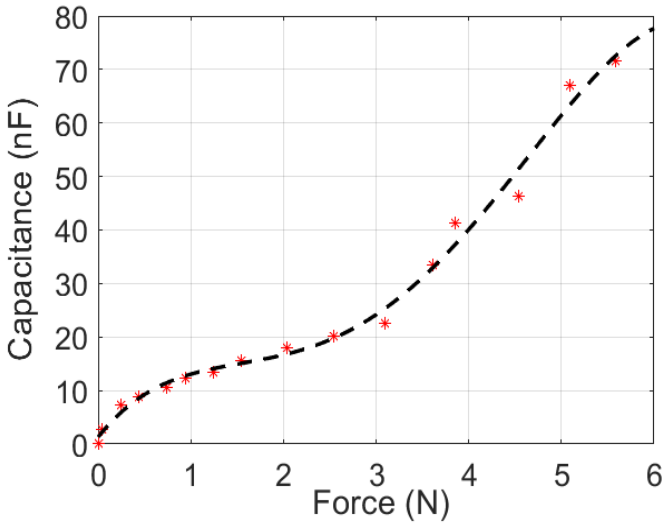

Figure 3-24 Force response curve of the cloth electrolyte sensor

In biomedical in vivo applications using traditional capacitive sensors, the interference from human tissues on the fringe electric field of the sensors can cause large and highly varying parasitic noise, which contaminates the sensor signal and cannot be eliminated by pre-calibration and subtraction. Our supercapacitive sensors developed do not suffer from this problem. A water-proofed embodiment of the supercapacitive sensor is dipped inside

the water (Figure 3-25). The response of the process is shown in Figure 3-26. The capacitance increases by a small amount ranging from $1\ pF - 10\ pF$, starting from a base capacitance of $600\ pF$, which includes variations from instrument errors. This increase in capacitance in the presence of water is negligible compared to the ultra-high sensitivity of the sensor at $\sim 20\ nF/N$. The parasitic capacitance generally exists in all traditional capacitive sensors and pollutes measured signals during in vivo applications. In traditional MEMS electrostatic capacitive sensors, the distance between the electrodes is not negligible relative to the lateral dimensions. The large gap between the electrodes results in additional radial components in the electric field, the so-called fringe electric field [41], [90], which in turn generates parasitic capacitance on the sides of a capacitor. In typical biomedical in vivo applications, the magnitude of parasitic noise can be of the order of pF, similar to the sensitivity of the MEMS sensor. Supercapacitive sensors do not suffer from parasitic noise. In a supercapacitor, the distance between the positive and negative charges at each electrode is of the order of the size of one or two atomic layers. Hence, the fringe fields are negligible.

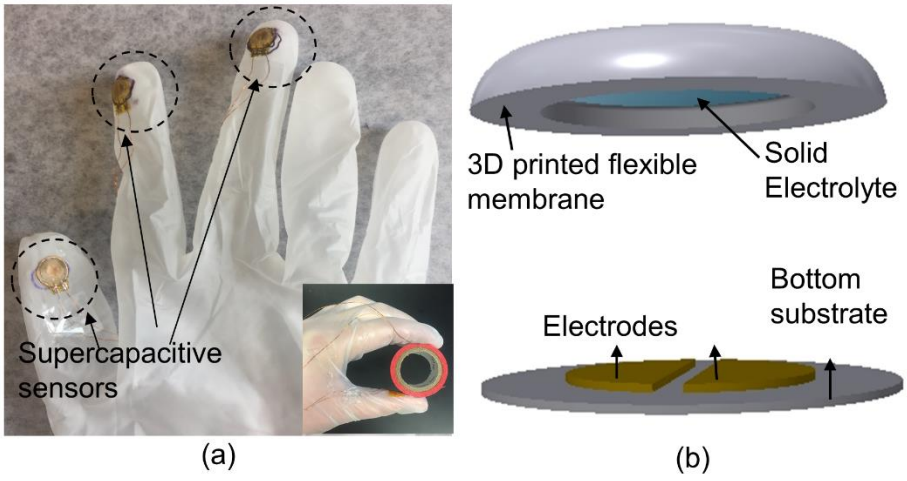

Figure 3-25 Water-proof embodiment of paper-based supercapacitive force sensor used on a glove. (a) Photograph. (b) Schematic of the supercapacitive sensors

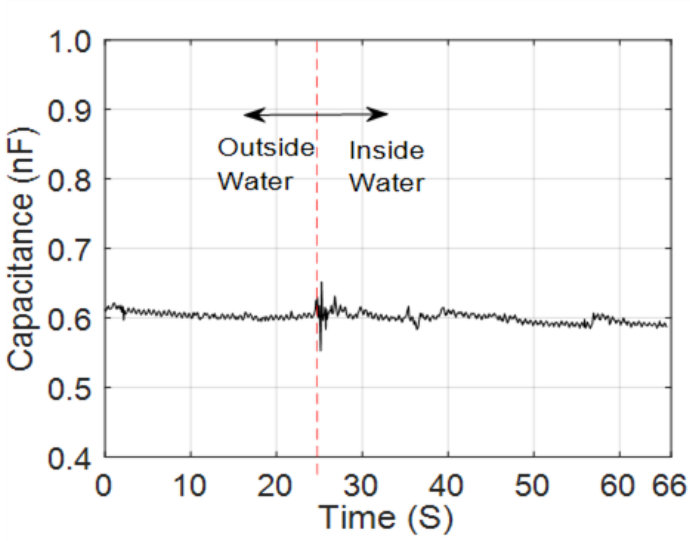

Figure 3-26 Response curve of a water-proofed paper-based supercapacitive sensor when immersed into water.

3.5 Conclusions

This chapter presented a new method for fabricating solid-state electrolytes based on paper substrates coated with ionic gel. The ease of making paper substrates of different shapes allows us to construct electrolytes of various complicated 3D geometries. Paper eventually dissolves in the ionic gel, leaving behind a soft highly flexible electrolyte with micro-wrinkles, essential for ensuring high deformability and high sensitivity of the supercapacitive mechanical sensors.

The new fabrication method overcomes the several disadvantages of the original ionic gel electrolytes and of liquid electrolytes which have severely limited broad application of supercapacitive sensors. The flexible paper-based solid electrolyte is utilized to make various supercapacitive sensors. The sensitivity and range of our paper-based supercapacitive sensors far exceeds those of traditional MEMS capacitive sensors. In spite of their superior performance, the new sensors can be fabricated quickly and highly inexpensively without the need of any cleanroom facilities. The ease of fabrication and the versatility of the sensor configurations was demonstrated by a number of mechanical sensor embodiments that can measure normal forces. Our method for fabricating paper-

based supercapacitive mechanical sensors can be easily customized to specific industrial and biomedical applications and broadly applied to make high-sensitivity mechanical sensors in resource-limited contexts.

Chapter 4

An Instrumented Urethral Catheter with Supercapacitive Pressure Sensors

4.1 Introduction

This chapter designs and fabricates an instrumented urethral catheter for measurement of distributed urethral pressure profiles. The supercapacitive sensing mechanism is explored for the pressure sensors. The supercapacitive sensor has high sensitivity and negligible parasitic capacitance, as discussed earlier in Chapter 2 and Chapter 3. The instrumented catheter is fabricated using a combination of MEMS technologies and 3D printing. Various tests are conducted to validate the performance of the catheter, including in vitro tests and tests inside an extracted sheep bladder.

In the human body, pressure is an essential parameter governing the function of many organs. Pressure is measured throughout the organ systems (e.g. the cardiovascular or nervous system), and therefore in different fluids, in many medical applications. Determining the pressure accurately helps the physician make critical decisions related to diagnosis or treatment. Direct pressure measurement is often performed by sensors using minimally invasive medical devices. For in vivo applications, pressure sensors are usually mounted on a catheter body, delivering measurement results in real time. Various sensing mechanisms have been explored for sensing pressure inside the human body using a

catheter. Due to the ease of miniaturization of silicon-based sensors, piezoresistive sensors have been widely used as pressure sensors for in vivo applications [91]–[93]. However, piezoresistive sensors need compensation for drifting [94]. Optical sensors have also been developed for in vivo pressure measurement, through measuring changes in intensity of the reflected light [95]–[97]. However, the complexity of the sensor limits its application for in vivo use [96]. Due to low temperature and pressure hysteresis, low power consumption and easy fabrication, capacitive pressure sensing have also explored for use on a catheter [98], [99]. However, for in vivo use, capacitive sensors have an inherent problem of parasitic noise [98], [100].

As discussed in Chapter 3, a new sensing mechanism has been developed, namely the supercapacitive sensor, and is explored here for in vivo pressure sensing. Supercapacitors have previously been used as energy storage devices. They exhibit capacitances that are several orders of magnitude higher than traditional capacitors. In this chapter, supercapacitors are used as distributed sensors for a catheter-based application. For a conventional capacitive sensor, the discontinuity in the material at the edge of a capacitor results in additional radial components in the electric field, the so-called fringe electric field. This fringe effect in turn generates parasitic capacitance components on the sides of a capacitor. In typical biomedical in vivo applications, the magnitude of parasitic noise can be of the order of pF, similar to or exceeding the sensitivity of the MEMS sensor to pressure [98]. In a supercapacitor, due to the thin dielectric layer and high surface area electrodes, the capacitance of a supercapacitor is at least 3 orders of magnitude higher than the parasitic capacitance in a supercapacitor, which makes the parasitic capacitance negligible [99]. Besides, the fringe effect is minimal in a supercapacitor due to the thin dielectric layer.

Urology is a medical field where catheters are often used for diagnosis. For example, a catheter may be inserted in the urinary tract via the urethra into the bladder for diagnosis of lower urinary tract dysfunction. Urinary incontinence (UI), as defined by the International Continence Society, is "the complaint of any involuntary leakage of urine" [101]. The most common type of urinary incontinence in women is stress urinary incontinence (SUI), followed by urge and mixed incontinence [102]. SUI happens when the sphincter muscles are not strong enough to fully pinch the urethra shut, causing a

sudden, strong urge to urinate that patients may not be able to control, especially during activities that increase intra-abdominal pressure, such as coughing, sneezing or bearing down. Globally, up to 35% of population over the age of 60 years is estimated to be incontinent [103]. It is estimated more than 50% of nursing facility admissions are related to incontinence [104]. The most widely used method for diagnosis of the cause of UI is urodynamics (UD) [105]. During UD tests, a thin, flexible Foley catheter is inserted into the bladder through the urethra to fill and empty the balder (Figure 4-1). The urethra pressure profile (UPP) inside the urethra is recorded by the sensor on the catheter.

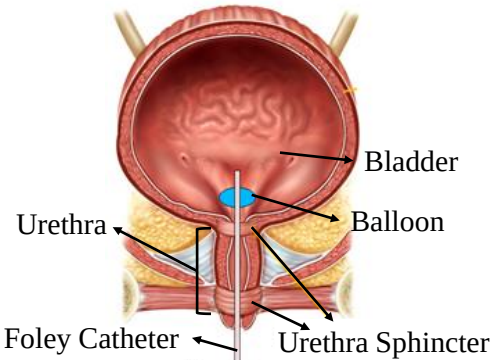

Figure 4-1 Foley catheter inserted into urethra during UD test

In this chapter, an instrumented urethral catheter based on supercapacitive sensors is developed to measure force distribution in the urethra, during clinical diagnosis in patients with UI. The catheter is highly soft, flexible and the sensors are able to operate in a body fluid environment. The performance of the catheter is evaluated in this chapter by an ex vivo test, a pressure cuff test, and an inside-water test. In the future, during clinical diagnosis with the new catheter, bladder filling, coughing, laughing, abdominal stress, and other tests can be used to pinpoint the source of the UI problem. The outline of the rest of this chapter is as follows: In section 4.2, the design and fabrication of the catheter are presented. Various experimental methods are used to evaluate the performance of the sensor in section 4.3. Results are presented in section 4.4 along with discussion of the results. Conclusions are presented in section 4.5.

4.2 Design and Fabrication

4.2.1 Design of the Catheter

The catheter consists of a 3D printed catheter body, five supercapacitive sensors, and their associated electronics. 3D printing is an additive manufacturing technology in which material is joined or solidified under computer control to create a three-dimensional object, with material being added together, typically layer by layer.

The sensors and the electronics are assembled on a 3D-printed catheter body with a diameter of 7Fr (2.33mm). The catheter is designed to be flexible for easy insertion. Figure 4-2 shows the side view of the five supercapacitive sensors on the catheter body. The electrodes are patterned on a soft substrate as shown in Figure 4-2, including five electrodes and one common electrode. The electrolyte is cured on the surface of a soft deformable arch structure inside a 3D printed chamber, which is assembled over each electrode. The load applied from the top of the chamber will cause the deformation of the soft structure, which brings the electrolyte down to touch the bottom electrodes, and consequently creates a capacitance change.

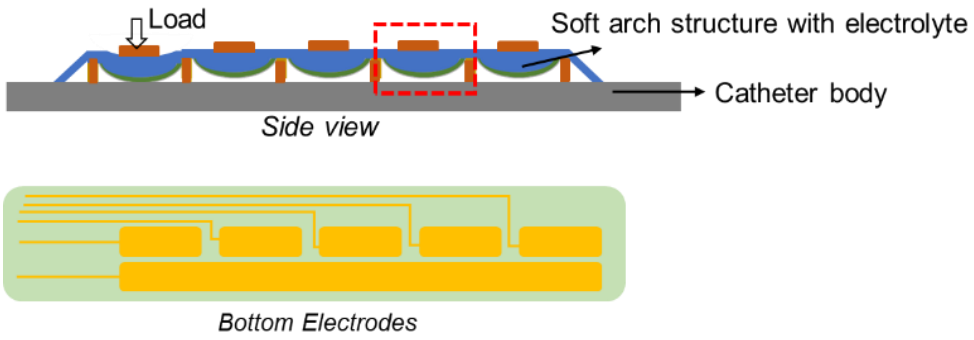

Figure 4-2 Working mechanism of the supercapacitive sensor on the catheter

The soft substrate with electrodes is assembled on a flat stage of the catheter body as shown in Figure 4-3. The chamber which hosts the electrolyte is printed with a combination of both hard and soft material (Figure 4-4). The side wall and internal arch structure of the part are made of soft material that will deform upon loading. On the top of the soft part, a hard bump is designed for the purpose of better receiving the applied load and transferring

it to the soft body. Two separators are designed as supports at the two ends. Besides, a hard skeleton is designed and embedded inside the soft body for recovering after the load is released.

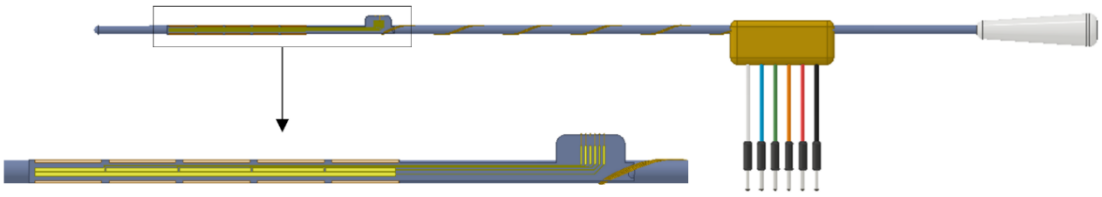

Figure 4-3 Schematic of the catheter and bottom electrodes

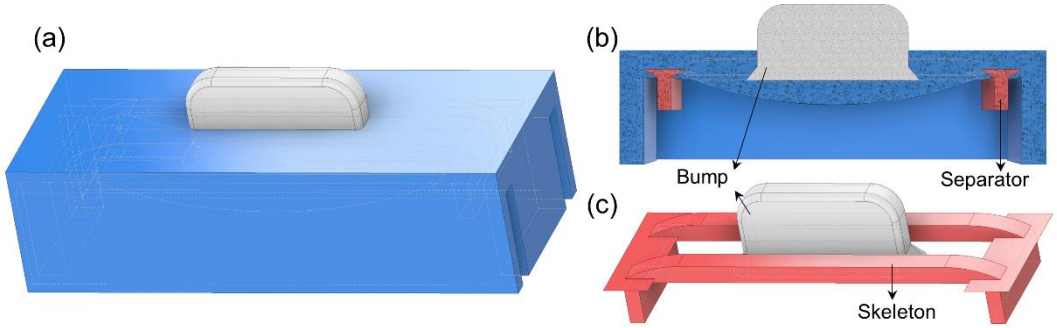

Figure 4-4 (a) Schematic of chamber with electrolyte. (b) Half section view of the chamber. (c) Embedded hard structure of the chamber

4.2.2 Fabrication of the Instrumented Catheter

The catheter body is made with 3D printing technology using a soft material (Veroclear, Stratasys), as shown in Figure 4-5. The diameter of the catheter body is 7 Fr (2.33mm). Near the tip of the catheter, a flat stage is printed to host the electrodes. Another stage with grooves is designed near the other end of the catheter body for hosting the connectors and wires.

Figure 4-5 3D printed catheter body

The bottom electrodes are fabricated on a flexible substrate, namely a polyimide film (75μm, 300 HPP-ST, Dupont), using MEMS fabrication technologies, as shown in Figure 4-6. First, a thin layer of copper (30nm) is sputtered on a polyimide film (PI), on top of which a gold layer (20nm) is sputtered. Then, the 5 electrodes and one common ground electrode are patterned using photolithography and wet etching. The as-fabricated electrode is shown in Figure 4-7. The soft and flexible polyimide film with electrodes is transferred onto the catheter body (Figure 4-8).

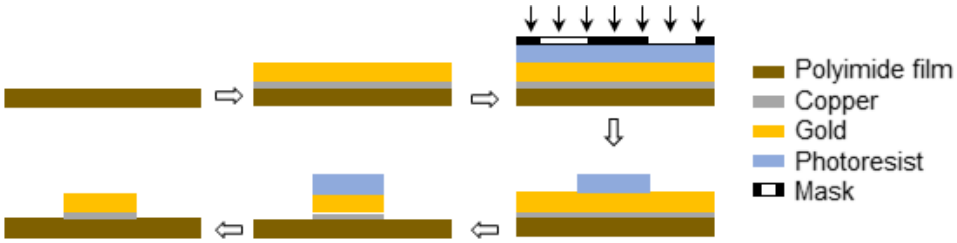

Figure 4-6 Fabrication process of the bottom electrodes

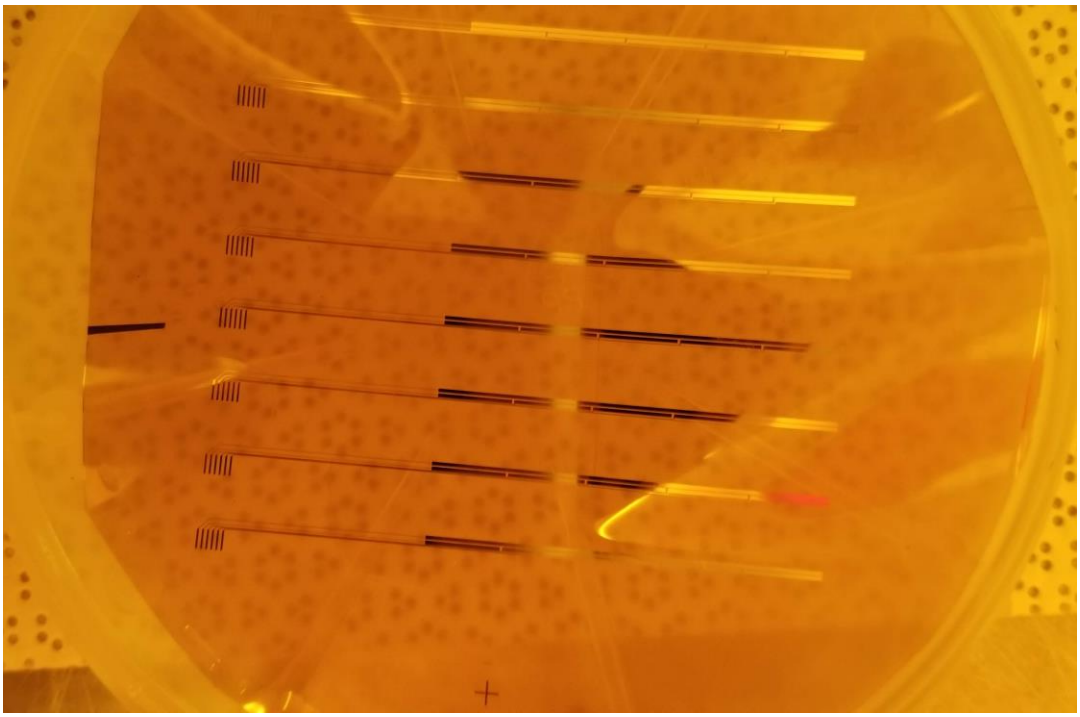

Figure 4-7 The electrodes patterned on a PI substrate

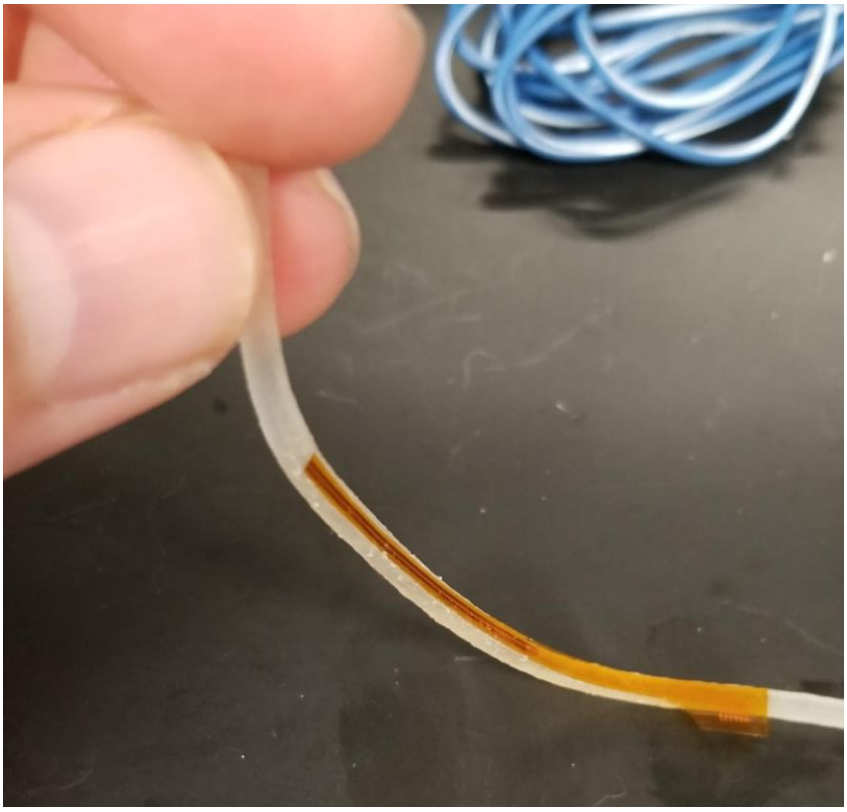

Figure 4-8 Soft and flexible polyimide film with electrodes assembled on the soft catheter body

The paper-based solid electrolyte is cured on top of an arch structure inside a 3D printed chamber as shown in Figure 4-9. The fabrication process starts from cutting the filter paper into a rectangular shape followed by pre-shaping it into an arch. The arch is then transferred to the top of the soft arch inside the 3D printed chamber. The ionic gel described in section 3.2 was brushed onto the paper. The ionic gel functionalizes the entire thickness of the paper and results in a flexible solid-state electrolyte. After that, the combination is put under UV light in a glovebox for 1 min. A clear film (150um) sticking to the 3D printed part is obtained. The 3D printed chamber with electrolyte is made using multi-material 3D printing technology, combining materials of different properties in a single part. The structure contains a soft body (Stratasys, Agilusclear), a hard bump, two hard separators and a hard skeleton (Stratasys, Verowhite). The bump is printed for the purpose of better receiving force applied from the top, while the hard skeleton is embedded inside the soft body and designed to improve the recovering after force is released.

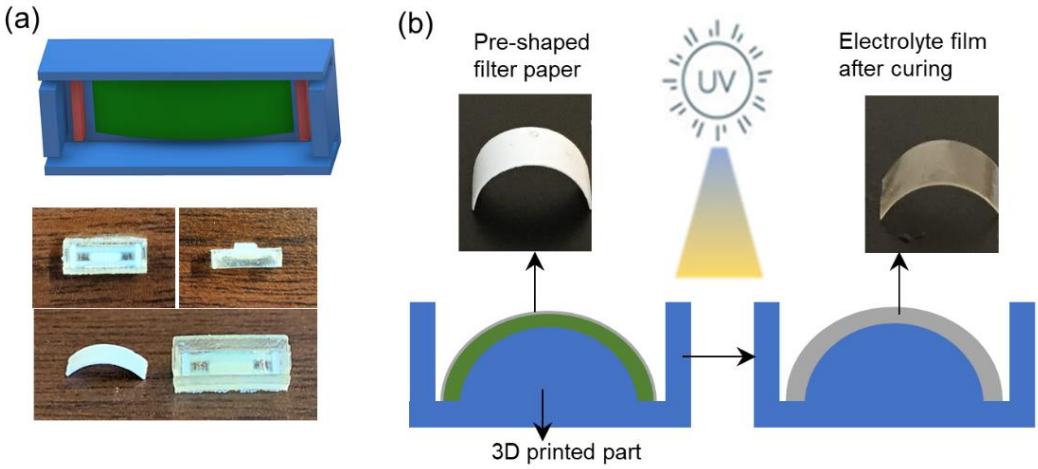

Figure 4-9 (a) Schematic and photo of the pre-shaped filter paper and 3D printed part. (b) Fabrication of the electrolyte.

The soft parts with the cured electrolytes are then assembled over the electrodes using sealing glue (Loctite, Waterproof Sealant). There is an initial gap (around 50 μm) between the peak of the arch and the bottom electrodes in each sensor. Connecting wires (40 AWG, enamel wires) are soldered onto the electrical contact pads on the PI substrate and then wrapped around the catheter. The other ends of the wires are connected to 5 jumper wires

for easy connection to the measurement equipment. The assembled instrumented catheter with 5 supercapacitive sensors is shown in Figure 4-10.

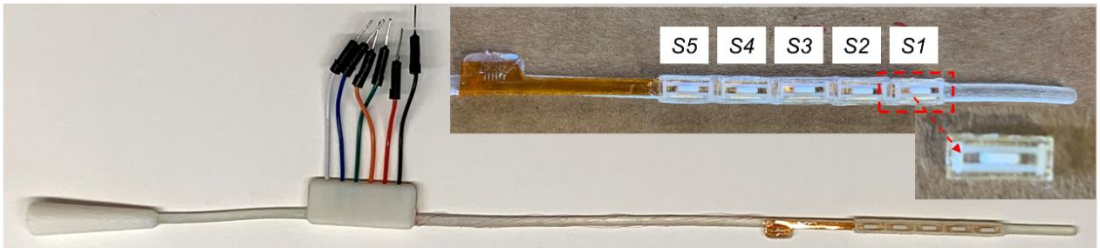

Figure 4-10 The assembled urethral catheter with 5 supercapacitive sensors

4.3 Tests of the Catheter

4.3.1 In Vitro Load Cell Experimental Setup

The catheter is tested with increasing forces using a custom-designed experimental setup as shown in Figure 4-11 (a) and (b). The urethral catheter is fixed on the bottom stage, while the varying force is applied from the top through a load cell (ATI, Nano17). The load cell is fixed on a translational stage, that can move up and down. By moving the translational stage down, the force is increased on the sensor as shown in the inset of Figure 4-11 (a). The force readings can be recorded by the load cell. The capacitance response of each sensor is recorded with a capacitance meter (Rigol DM3068) along with the changing force.

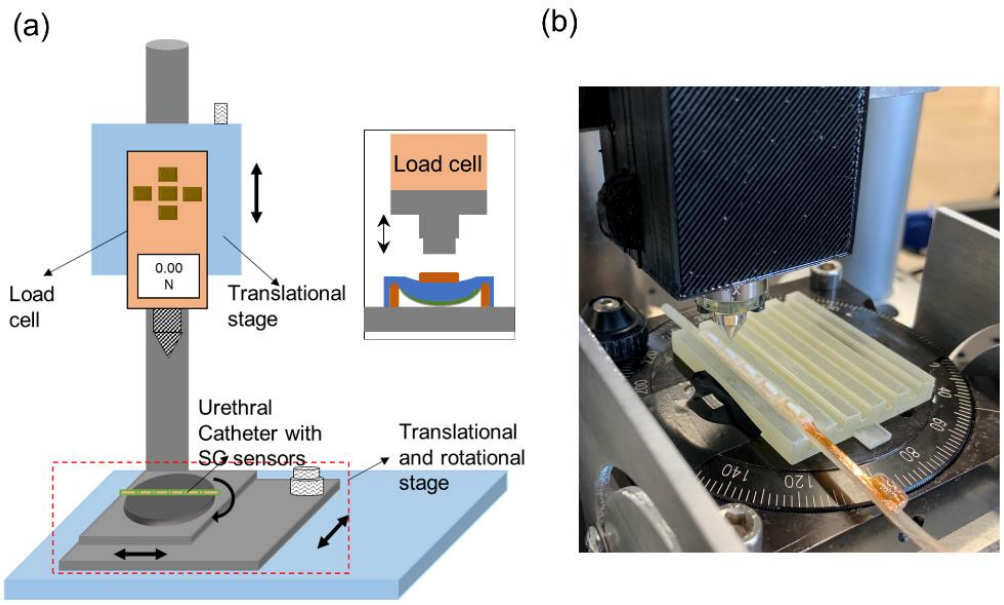

Figure 4-11 (a) Schematic and (b) photo of the experimental setup.

4.3.2 Cuff Test

To create a situation that is similar to that inside a real urethra, a cuff test is designed as shown in Figure 4-12 (a). An inflatable cuff is wrapped around each sensor. The other end of the cuff is connected to a syringe and a pressure gauge. By moving the piston of the syringe, the cuff can be inflated, and pressure can be increased gradually inside the cuff, thus applying more pressure on the sensor top. The pressure is read from the pressure gauge and the response of the sensors is also measured with the changing pressure.

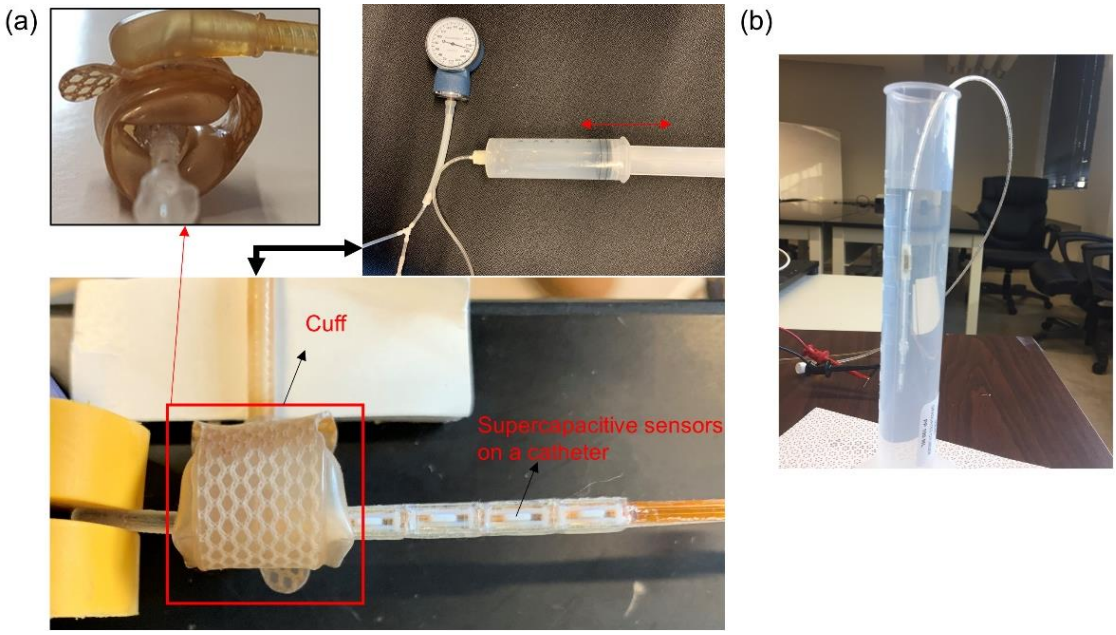

Figure 4-12 (a) Cuff test setup (b) Inside-water test setup

4.3.3 Inside-Water Test

In order to investigate the influence of parasitic noise on the instrumented catheter, a water-proofed embodiment of the supercapacitive sensor on a catheter is dipped inside water, as shown in Figure 4-12(b). The capacitance response of the sensor is recorded, both while it is outside water and inside water. The increased capacitance after being put inside water is regarded as the parasitic capacitance.

4.3.4 Extracted Bladder Test

The catheter is inserted into an extracted bladder as shown in Figure 4-13, with the five sensors being inside the urethra. The locations of the 5 sensors in the urethra can be seen in Figure 4-13(a). An elastic band is wrapped around the urethra, with one end fixed and the other end connected to a force gauge (Figure 4-13 (b)). By gradually moving the force gauge to apply force and stretch the band, pressure can be applied on the sensors.

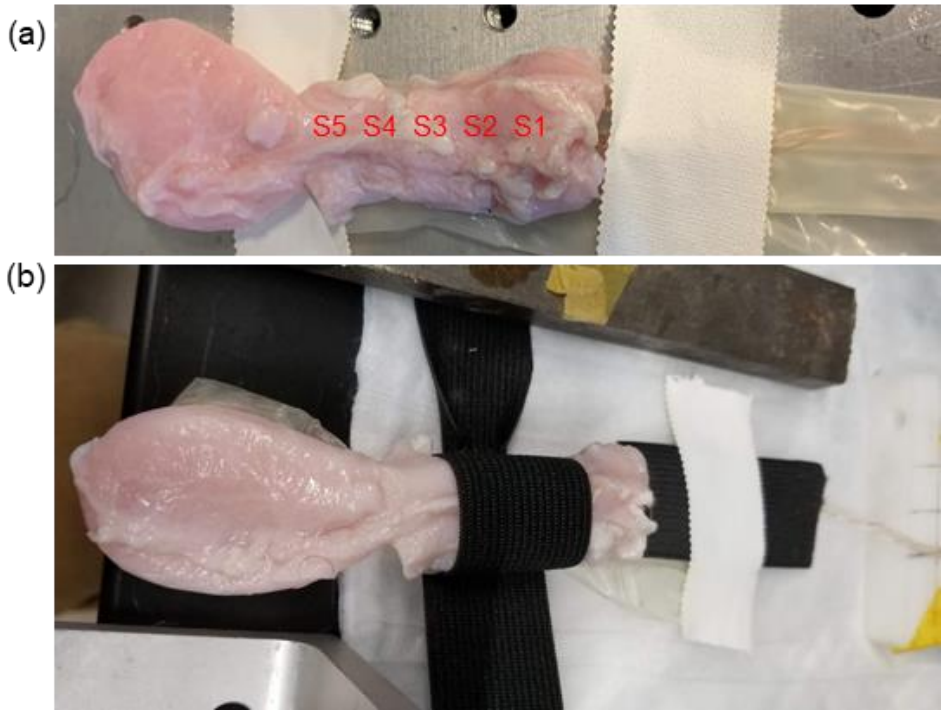

Figure 4-13 Urethral catheter inside an extracted bladder with the sensors being inside the urethra (a) before and (b) after loading

4.4 Results and Discussion

The response of each sensor with changing force is shown in Figure 4-14 for the in vitro load cell tests. The sensitivity of the sensors is the in order of $30 - 50nF/N$, which is more than 1000 times higher than conventional capacitive sensors [89][106]. The capacitance response of each sensor to the increasing pressure inside the cuff is shown in Figure 4-15 for the cuff tests. All the sensor readings increase monotonically with the increasing pressure inside the cuff.

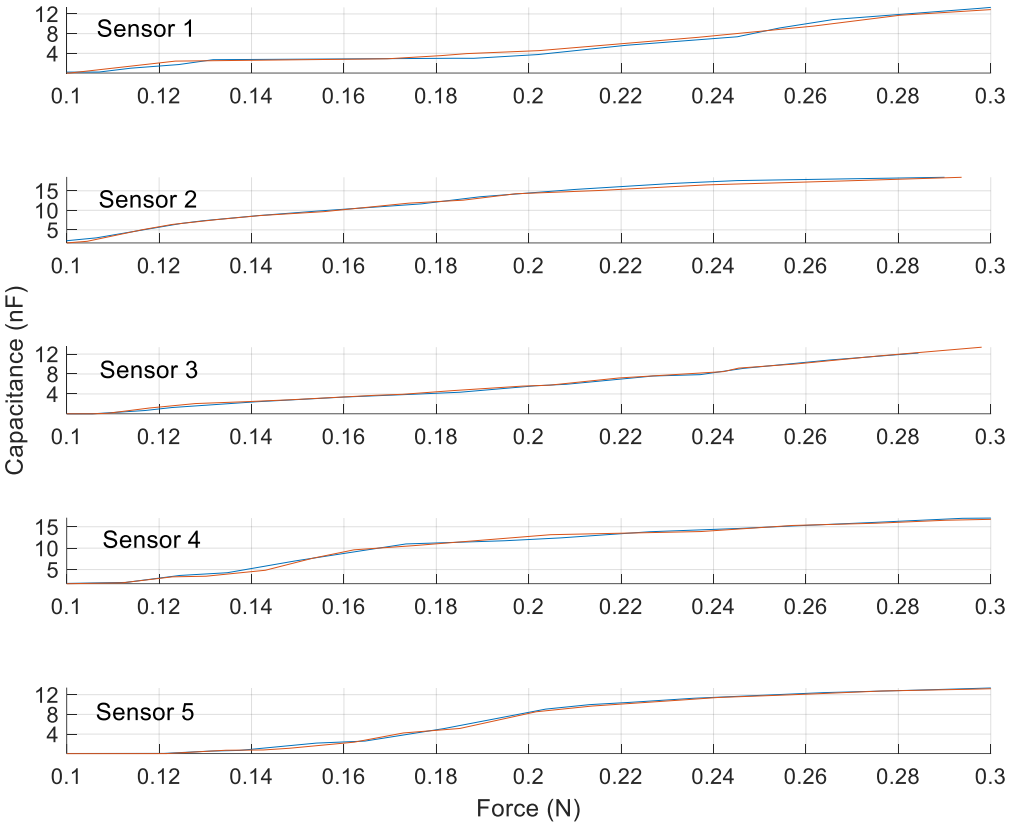

Figure 4-14 Capacitance response of each sensor to the increasing force

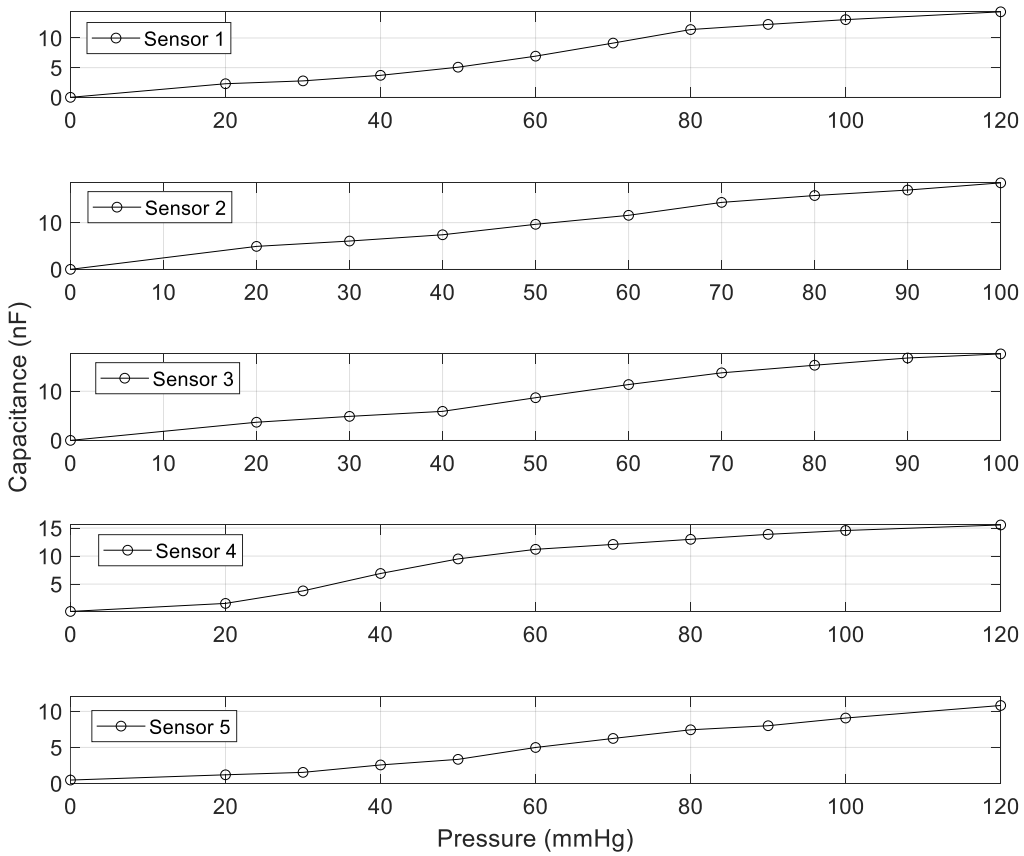

Figure 4-15 Sensors response to the increasing cuff pressure

The parasitic capacitance test result is shown in Figure 4-16. After dipping into water, the capacitance increases by $10pF$, which is negligible compared to the high sensitivity of the sensor (30-50 nF/N). That indicates that the catheter is immune from parasitic noise induced by human tissue for in vivo applications.

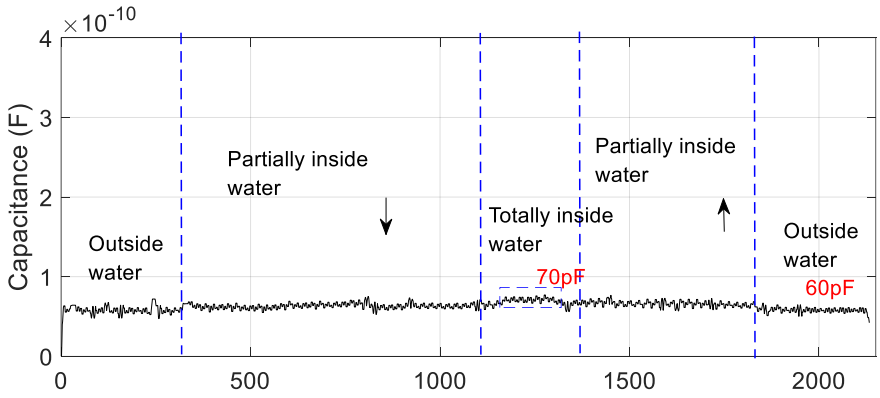

Figure 4-16 Capacitance response outside water and inside water

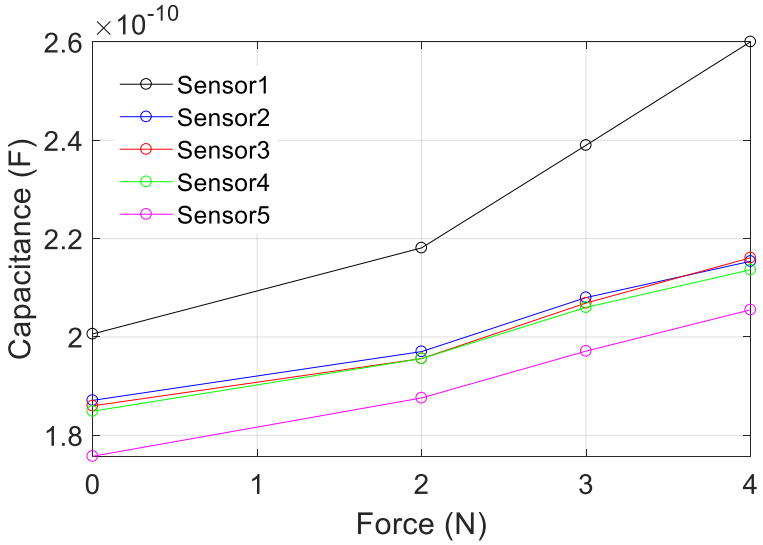

Figure 4-17 Sensor response inside the bladder

Figure 4-17 shows the responses of the sensors during the ex vivo test involving the extracted sheep bladder and urethra. As the stretching force applied on the elastic band increases, the responses of all the five sensors increase monotonically. Since sensor 2-4 are located in the middle of the urethra (which is a thinner portion of the urethra), while sensor 1 is located under the thicker tissue part which experiences more force, the response of sensor 1 is significantly higher than that of sensors 2-4. Sensor 5 is outside the wrapping zone, so it experiences less capacitance change compared to all the other sensors.

4.5 Conclusions

A multi-sensor flexible instrumented catheter for measurement of distributed pressure inside the urethra was developed. The developed sensor has important clinical applications in urodynamic testing, and potentially in other in vivo biomedical catheter applications. Supercapacitive force sensors were designed and fabricated using a combination of MEMS technologies and 3D printing. Experimental in vitro evaluation was conducted using a custom-designed experimental setup with a load cell and then later inside an inflatable cuff. The influence of parasitic noise was investigated by dipping the sensor inside water and measuring its resulting capacitance change. Also, ex vivo tests were conducted inside an extracted bladder and urethra. The experimental results showed preliminary data to indicate

that the sensor has high sensitivity and negligible parasitic capacitance, which could provide highly accurate urethral pressure measurement while removing the influence of human tissue parasitics. Future work could involve in vivo evaluation of the catheter in an IACUC approved sheep study and later in an IRB approved clinical human study.

Chapter 5

A Supercapacitive Shear and Normal Force Sensor

5.1 Introduction

There is a significant research interest in developing domestic robots that can handle common chores inside and around homes to enable a more comfortable and safe living environment, especially for the elderly [107]–[109]. Domestic robots could do more than just floor cleaning - they can be trained to handle objects and dexterously do various household tasks, such as lifting things, washing the dishes and sweeping the desk. When a human being grasps and manipulates objects to lift it, a normal force has to be applied large enough to avoid slipping. A human being can continuously adjust the grasp force on the basis of information from the tactile sensors on his/her skin [110]. For robots, however, this is difficult to realize. In order to train a household robot to manipulate objects properly, and avoid dropping or breaking them, a database of normal and shear forces needs to be constructed for various household tasks, by observing a skilled human doing the task. A set of soft sensors on a glove worn by human beings that can measure both shear and normal forces would be very helpful to collect enough data to train domestic robots, as shown in Figure 5-1.

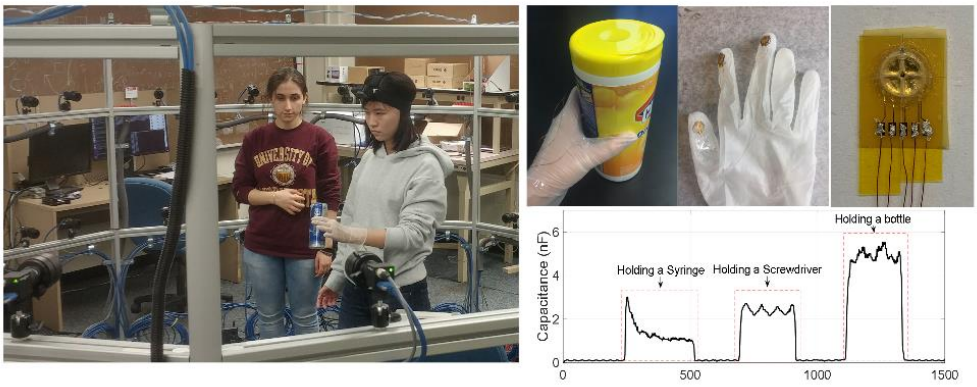

Figure 5-1 Measuring shear and normal forces while handling various objects wearing an instrumented glove

Various sensing principles have been explored by the robot industry to measure forces on fingertips. Piezoresistive and piezoelectric force sensors have been explored due to their ease of micro-fabrication [111]–[115]. These sensing principles, however, suffer from problems like hysteresis, drift, creep and temperature dependency. Optical sensors have also been applied for measuring shear forces combining a trapezoidal external metallic frame with an integrated micro optical displacement sensor [116], [117]. However, these sensors do not have capability of measuring normal force. Besides, these sensors cannot meet the requirements of being soft and compact for robotic applications. Due to low temperature and pressure hysteresis, low power consumption and easy fabrication, capacitive pressure sensing has also been explored for use in tactile sensors [110], [114], [118]–[125]. However, capacitive sensors have limitations of trade-off between sensing range and sensitivity, and parasitic noise. While several of the sensors above have a capability to measure both normal and shear forces, very little experimental data on their accuracy and robustness in real world applications is available. Due to the complexity of the coupling of the influence of normal and shear forces, experimental calibration at every combination of normal and shear force is also not feasible.

In this chapter, the supercapacitive sensing mechanism is explored for measuring normal and shear forces simultaneously. Supercapacitors have previously been used as energy storage devices. They exhibit capacitances that are several orders of magnitude higher than traditional capacitors. As discussed in Chapter 2, in conventional capacitive sensors, the discontinuity in the material at the edge of a conventional capacitor results in

additional radial components in the electric field, called the fringe electric field, which in turn generates parasitic capacitance components on the sides of a capacitance. In a supercapacitor, due to the thin dielectric layer and high surface area electrodes, the capacitance of a supercapacitor is at least 3 orders of magnitude higher than the parasitic capacitance in a supercapacitor, which makes the parasitic capacitance negligible [114]. Furthermore, in this chapter, a learning algorithm is used to develop a sensor model that can provide accurate estimates of shear and normal forces for a wide range and combination of operating normal and shear forces.

The outline of the rest of this chapter is as follows. In Section 5.2, the design and fabrication of the normal-shear force sensors is presented. In section 5.3, various experimental methods are used to evaluate the performance of the sensor and to generate data for training a deep neural network model to represent the sensor response. Experimental results are presented in Section 5.4 along with discussion of the results. Conclusions are presented in section 5.5.

5.2 Design and Fabrication of the Sensor

5.2.1 Design and Sensing Principle

A quad-unit force sensing cell consisting of 4 internal individual force units (S_1, S_2, S_3, S_4), that are axisymmetrically distributed is utilized as shown in Figure 5-2. Each force unit has two electrodes. The electrodes are patterned in such a way that the four units lie symmetrically on the axes of a Cartesian coordinate system with the center of the eight electrodes sitting at the origin. The electrolyte is cured on the surface of a soft semi-ellipsoid. This soft semi-ellipsoid is assembled over the electrodes. If only normal force is applied, as shown in Figure 5-2 (a) and (b), the contact area between the electrodes and electrolyte increases, resulting in an increase in capacitance of all four sensing units. If both normal and shear forces are applied (Figure 5-2(c)), the center of the contact area shifts accordingly depending on the direction of the shear force, with the readings from the four force units being different.

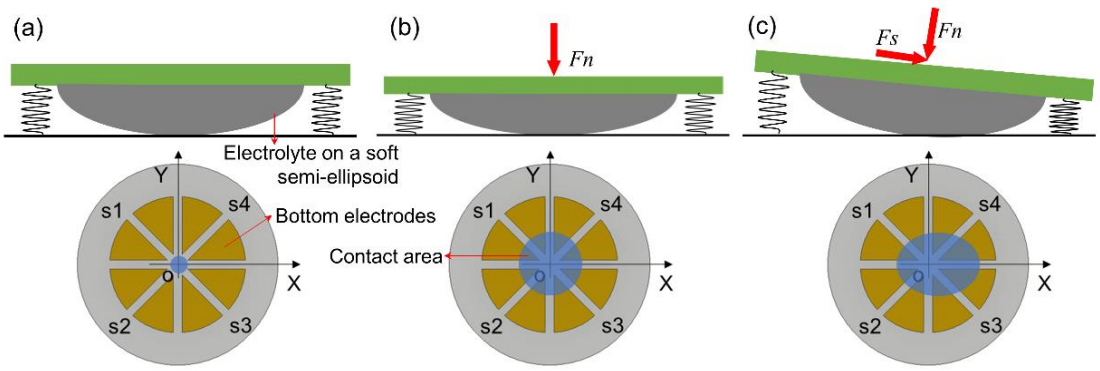

Figure 5-2 Working mechanism of the supercapacitve normal and shear sensor (a) no force is applied, (b) normal force is applied, (c) both normal and shear forces are applied.

The physical structure of the sensor is shown in Figure 5-3. The 4 pairs of electrodes are patterned in a circle on a soft substrate. The top chamber is made of both soft and hard material. It consists of a hard cap, a hard mesh, a soft semi-ellipsoid substrate to host the solid electrolyte and a soft side wall. The hard cap (Figure 5-3(a)) is designed for better receiving the force applied from the top. A hard mesh (or skeleton) is printed and embedded inside the soft side wall to increase the elasticity of the sensor (Figure 5-3(c) and (d)). The solid electrolyte is cured on the surface of the soft semi-ellipsoid, which can deform under the applied force. The 4 capacitance readings (C_1, C_2, C_3, C_4) of the 4 sensing units are used to estimate the normal force and shear force applied on the sensing cell.

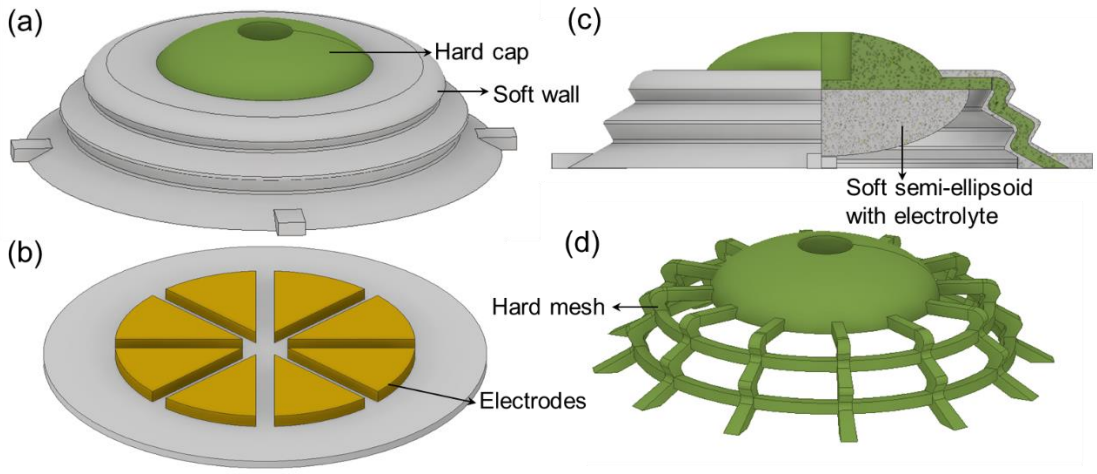

Figure 5-3 Schematic of the normal and shear force sensor (a) top chamber with the solid electrolyte, (b) bottom electrodes patterned on a soft substrate, (c) three quarter section view of the top chamber, (d) a hard mesh skeleton embedded in the soft wall.

5.2.2 Fabrication of the Sensor

The bottom electrodes are fabricated on a flexible substrate, namely a polyimide film (25 µm, Pyralux Copper Kapton Laminate, Dupont), using MEMS fabrication technologies, as shown in Figure 5-4(a). First, a thin layer of titanium (20nm) is sputtered on the polyimide film (PI) for enhancing adhesion, on top of which a gold layer (200nm) is sputtered. Then, the 8 electrodes are patterned in a circle using photolithography and wet etching. The as-fabricated electrode is shown in Figure 5-4(b).

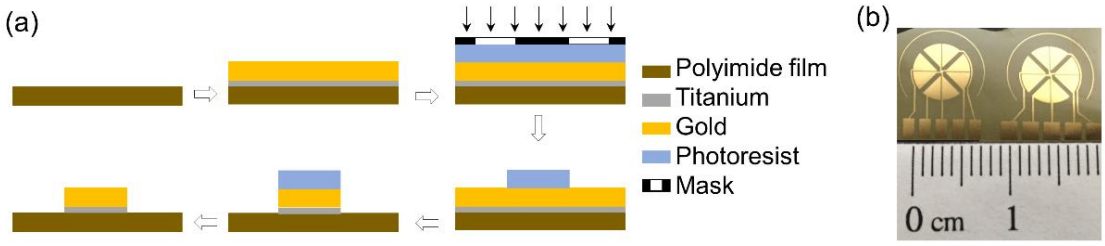

Figure 5-4 (a) Fabrication process of the bottom electrode. (b) The electrodes patterned on PI substrate

The paper-based solid electrolyte is cured on top of an arch structure inside a 3D printed chamber as shown in Figure 5-5. The fabrication process starts from cutting the filter paper into a circular shape followed by pre-shaping it into a dome shape. The arch was then transferred to the top of the soft arch of the 3D printed chamber. An ionic gel was brushed onto the paper, that functionalizes the entire thickness of the paper and results in a solid-state electrolyte. After that, the combination was put under UV light in a glovebox for 1 min. A clear film (150um) sticking to the 3D printed part is obtained. The 3D printed chamber with electrolyte is shown in Figure 5-5(c). The part is made using multi-material 3D printing technology, combining materials of different properties in a single part. The structure contains a soft side wall (Stratasys, Agilusclear), a hard cap, a soft ellipsoid and a hard mesh (Stratasys, Verowhite). The cap is printed for the purpose of better receiving forces applied on top, while a hard mesh (or skeleton) is embedded inside the soft body and designed to improve the elasticity of the structure.

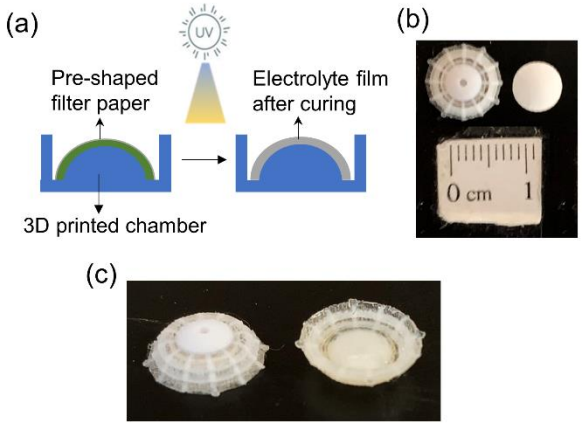

Figure 5-5 (a) Fabrication of the electrolyte. (b) 3D printed chamber and the pre-shaped filter paper. (c) Solid electrolyte cured inside the soft chamber

The soft chamber with the cured electrolytes was then assembled over the electrodes using sealing glue (Loctite, Waterproof Sealant). Connecting wires (40 AWG, enamel wires) are soldered onto the electrical contact pads on the PI substrate. The other ends of the wires are connected to 4 jumper wires for easy connection to the measurement equipment. The assembled sensor with 4 supercapacitive sensing units is shown in Figure 5-6.

Figure 5-6 Photograph of the assembled normal and shear force sensor.

5.2.3 Learning of the Sensor Response

In order to provide accurate estimates of the shear and normal forces acting on the top of the sensor, an accurate sensor model must be used to fully map from individual force unit readings to the applied normal and shear forces. For a linear sensor with axisymmetric stiffness, the normal force can be obtained from the average of the four force units as

$$F_z = \frac{1}{4}(K_{n1}C_1 + K_{n2}C_2 + K_{n3}C_3 + K_{n4}C_4) \quad (5\text{-}1)$$

where K_{n1}, K_{n2}, K_{n3} and K_{n4} are the calibration coefficients between normal force and capacitance of each sensor.

The shear force along the *x* axis can be obtained from:

$$F_x = |(K_{s3}C_3 + K_{s4}C_4) - (K_{s1}C_1 + K_{s2}C_2)| \quad (5\text{-}2)$$

While the shear force along the *y* axis can be obtained from:

$$F_y = |(K_{s1}C_1 + K_{s4}C_4) - (K_{s3}C_3 + K_{s2}C_2)| \quad (5\text{-}3)$$

where K_{s1}, K_{s2}, K_{s3} and K_{s4} are the calibration coefficients between shear force and capacitance of each sensor.

However, the fabricated shear and normal force sensor response is highly non-linear and complex, with forces being exerted from 3 degrees of freedom and the sensors not being axis-symmetric due to significant manufacturing imperfections. That can make accurately building an analytical sensor model very difficult in practice. Therefore, a generalized regression neural network [126]–[128] was used in order to obtain a model matching the experimental data as well as possible. A two-layer feed-forward network with sigmoid hidden neurons and linear output neurons, is designed to fit this multi-dimensional mapping problem as shown in Figure 5-7. The capacitance readings of the four sensing units are fed into the neural network as the inputs, while the 3D forces (measured by a load cell during training) are used as the outputs of the neural network. The network is trained with Levenberg-Marquardt backpropagation algorithm [129].

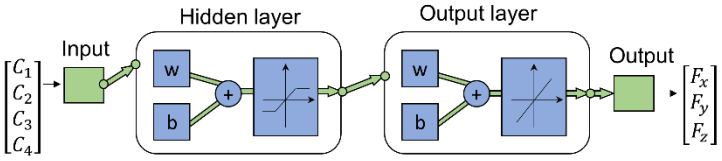

Figure 5-7 Schematic of the neural network

5.3 Experimental Setup

5.3.1 Data Collecting Experimental Setup

In order to collect various datasets for training the neural network, the assembled force sensor is tested with a custom-designed experimental setup as shown in Figure 5-8, which includes two translational stages (one X-Y stage for coarse tuning and one X-Z stage for fine tuning), a rotational stage, a six-axis load cell (ATI, Nano 17), and a pointed tip attached to the load cell. The sensor is fixed on the rotational stage, which is installed on the coarse X-Y translational stage on the bottom. The load cell is fixed on the fine X-Z translational stage over the sensor. By moving the X-Y translational stage down through rotating the vertical knob, varying normal force can be applied from the top through a load cell and the tip. By rotating the horizontal knob on the fine stage, shear force along X-axis can be applied. By changing the angle (θ) of the rotational stage, shear forces from all the orientations on the local sensor coordinate can be applied. The force readings can be recorded by the load cell simultaneously. The response of each sensor is recorded (Rigol DM3068) with the changing forces. So, the vertical displacement z, the horizontal displacement x of fine translational stage on the top, and the rotational angle of rotational stage (also the rotational angle of the sensor) θ are the three varying parameters during the test. Various combinations of the 3 parameters $[x_i, y_i, \theta_i]$ result in different shear and normal forces applied on the sensor.

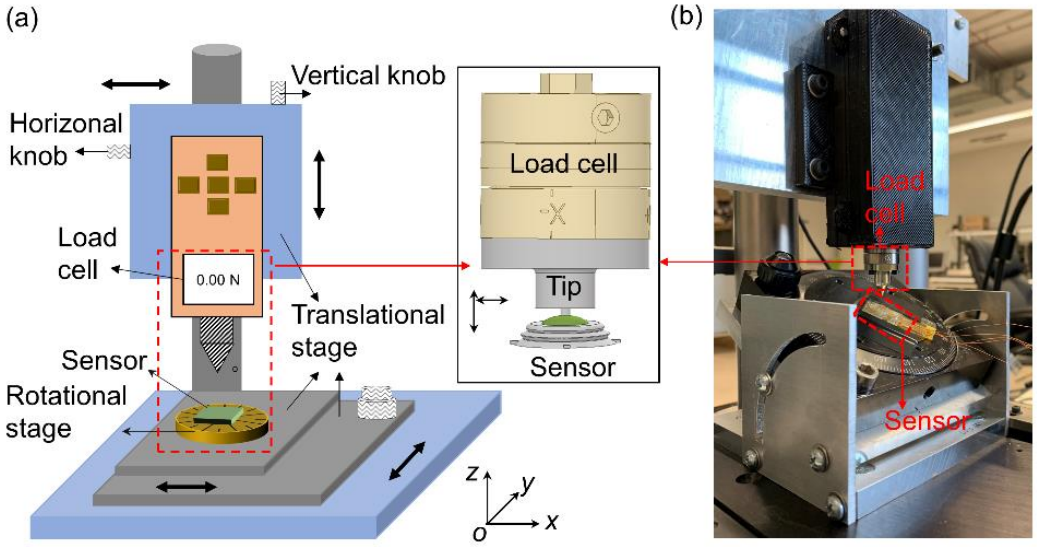

Figure 5-8 (a) The schematic and (b) photo of the experimental setup

To collect enough datasets for training, the following experimental procedure is used:

(1) First the pointed tip is aligned with the center of the sensor by moving the coarse X-Y translational stage on the bottom;
(2) The fine translational stage is moved down to add a normal force F_z on the sensor, then the z displacement is kept steady;
(3) The horizontal knob is turned to apply a shear force $F_s(F_x, F_y)$ gradually, the sensor readings and load cell measurements are recorded;
(4) The rotational stage is rotated by 15^o, steps (1)-(3) are repeated until $\theta = 360^o$.

For example, at $\theta = 45^o$, 6 different normal forces are applied, while under each normal force, a series of shear forces are applied as shown in Table 5-1.

Table 5-1 Norman and shear forces at θ = 45°`

	$\boldsymbol{\theta = 45^o}$					
	$Fz \approx 0.4N$	$Fz \approx 0.6N$	$Fz \approx 0.7N$	$Fz \approx 0.8N$	$Fz \approx 0.9N$	$Fz \approx 1.0\ N$
Fs (N)	0.05	0.1	0.1	0.1	0.1	0.1
	0.1	0.2	0.2	0.2	0.2	0.2
	…	…	…	…	…	…
	1	1	1	1	1	1

5.3.2 Inside Water Test

In order to investigate the influence of parasitic noise on the sensor, a water-proofed embodiment of the supercapacitive sensor is dipped inside water. The capacitance response of the sensor is recorded both while it is outside water and inside water. The increase in capacitance after being put inside water is regarded as the parasitic capacitance.

5.4 Results and Discussion

The response of the sensor if mainly normal force is applied (Figure 5-2 (b)) is shown in Figure 5-9. The sensitivity of the sensors to normal force along z-axis can reach as high

as $50nF/N$, which is more than 1000 times higher than conventional capacitive sensors [98], [130]. As seen in the figure, all 4 capacitances rise monotonically with increase in normal force.

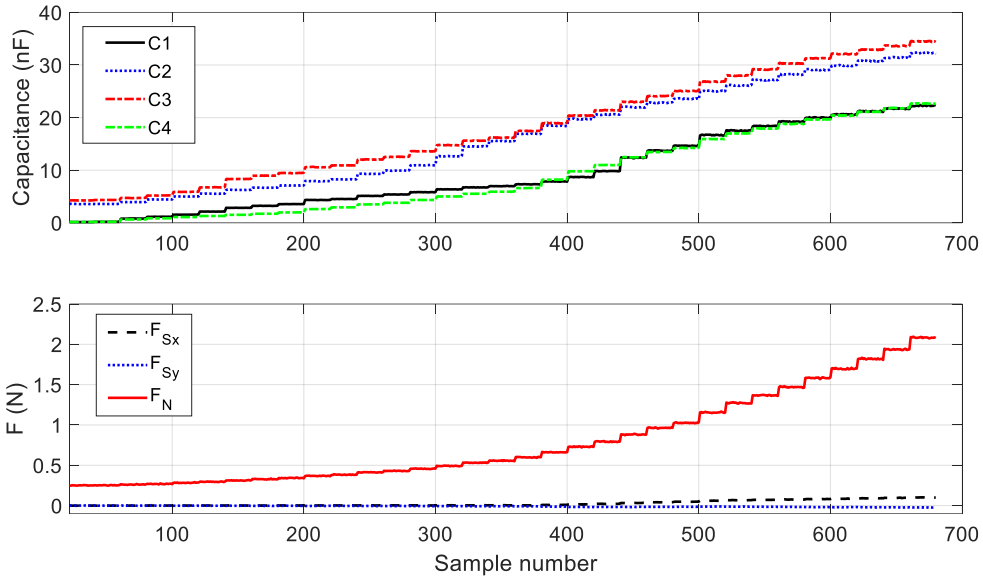

Figure 5-9 Sensor response mainly under gradually changing normal force

Figure 5-10 shows an example of the sensor response when both normal and shear forces are applied. The applied normal force is around $1.7N$. The shear force applied is at $\theta = 60^o$, which is towards S_4, in the local sensor coordinate as shown in Figure 5-11. As shown in Figure 5-10, S_4 capacitance increases, while the readings from S_2 changes in an opposite direction. S_1 experiences a minor increase in capacitance reading, while the S_3 decreases a little. The sensitivity of the sensor to shear force can reach as high as $22nF/N$, which is smaller than the sensitivity to the normal force due to the higher stiffness along the horizontal direction of the sensor.

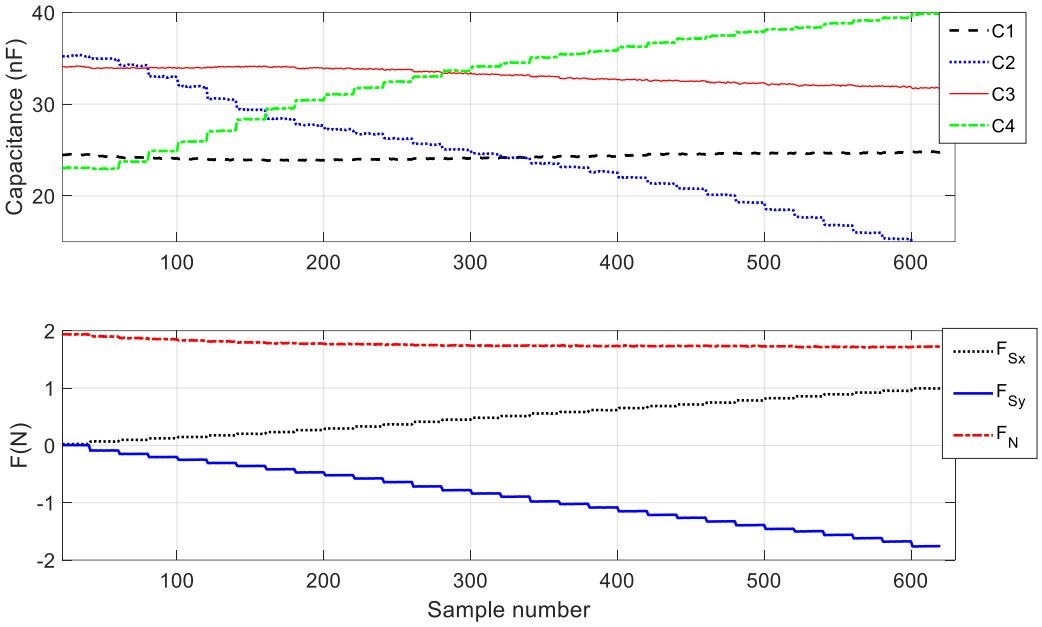

Figure 5-10 Sensor response under gradually changing shear force (θ = 60°) and a constant normal force

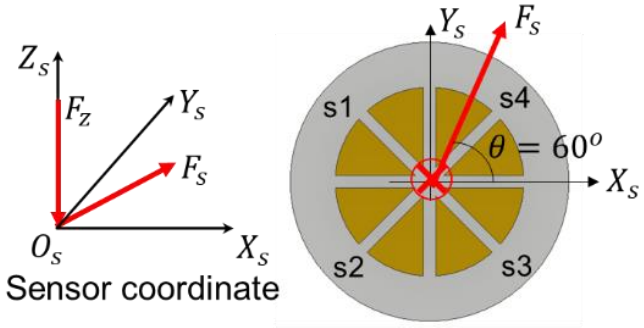

Figure 5-11 Normal and shear force in the sensor coordinate at θ = 60°

By following the test procedure described above, 32,000 datasets including sensor responses (C_1, C_2, C_3, C_4), and load cell measurements (F_x, F_y, F_z) are collected and used to train a model for the sensor. All the datasets used for training are shown in the 3D plot in Figure 5-12.

Several datasets are left aside not used for training and used separately to validate the performance of the model. An example validation is shown in Figures 5-13, 5-14 and 5-15. The applied normal force is around $1.0N$. The shear force applied is at $\theta \approx 265°$, which is towards S_2 and S_3, in the local sensor coordinate, as shown in Figure 5-13. The sensor

response as shown in Figure 5-14 is fed into the previously trained model. As shown in Figure 5-15, the fitted forces using the trained model and the real measured forces match well, with a maximum error of $0.02N$.

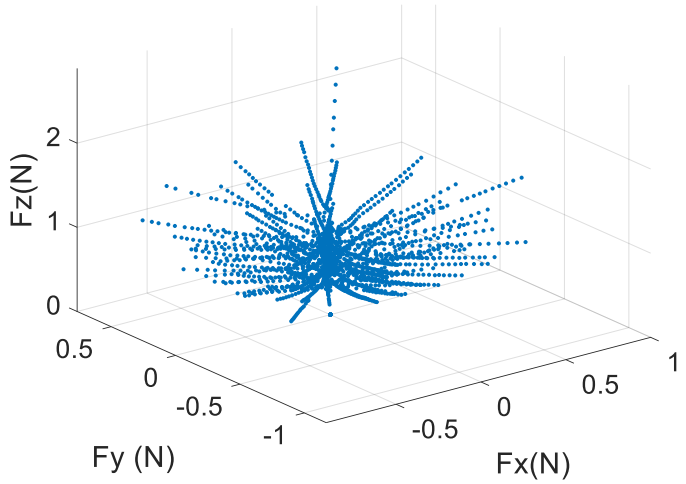

Figure 5-12 Force datasets in a 3D plot

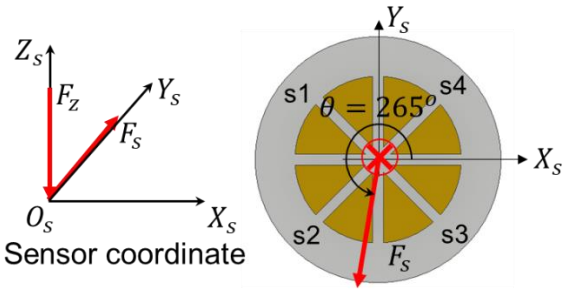

Figure 5-13 Normal and shear force in the sensor coordinate at θ = 265°

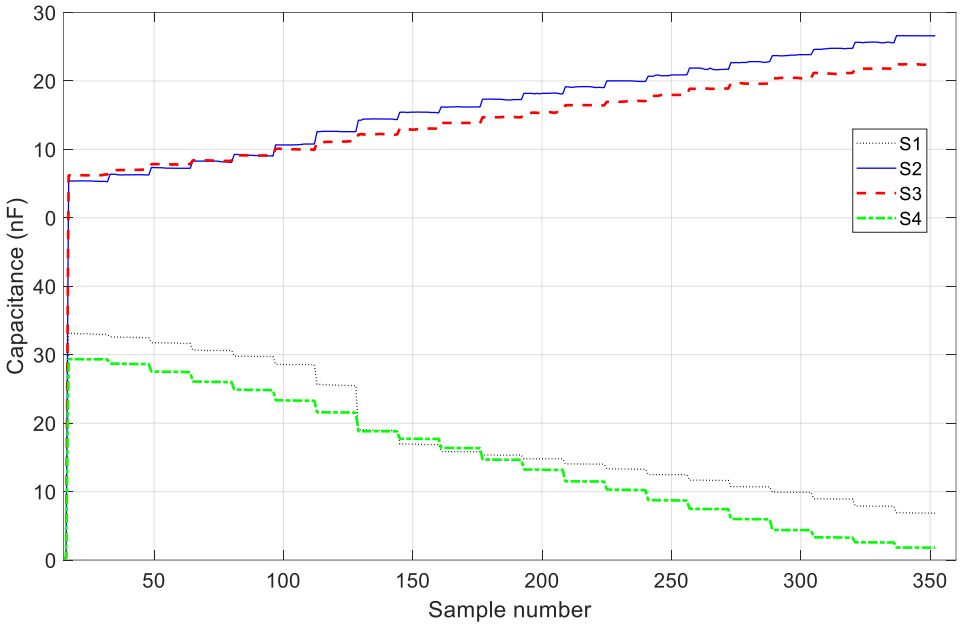

Figure 5-14 Sensor response under gradually changing shear force (θ = 265°) and a constant normal force

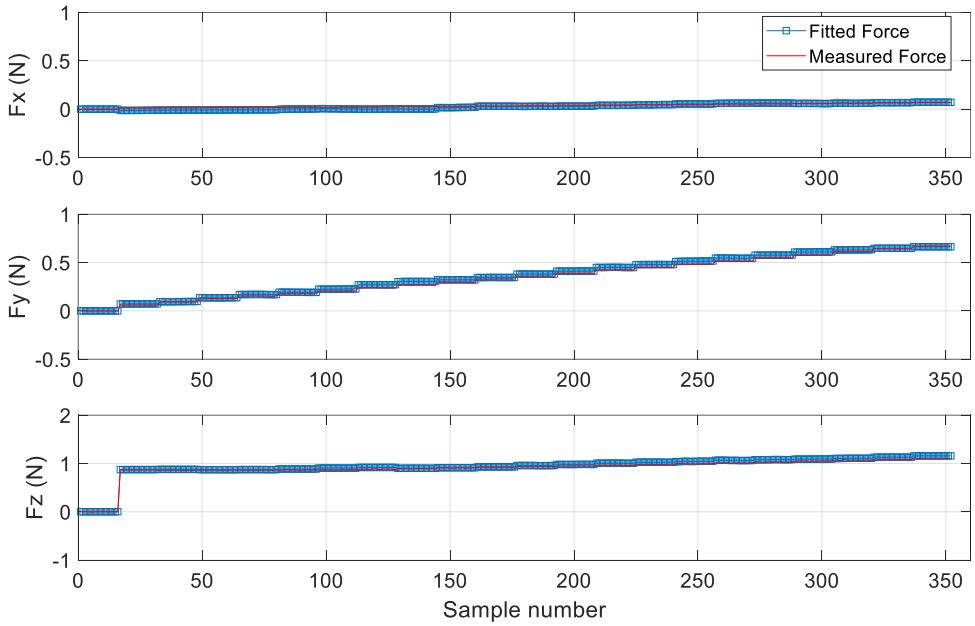

Figure 5-15 Estimated forces using the neural network fitted model

The result for the in-water test is shown in Figure 5-16. The capacitance increases by a small amount ranging from $1\,pF - 10\,pF$, starting from a base capacitance of $600\,pF$,

which includes variations from instrument errors. This increase in capacitance in the presence of water is negligible compared to the ultra-high sensitivity of the sensor at ~ $22nF/N$. That indicates that the sensor is immune from parasitic noise and can be used in liquid environments.

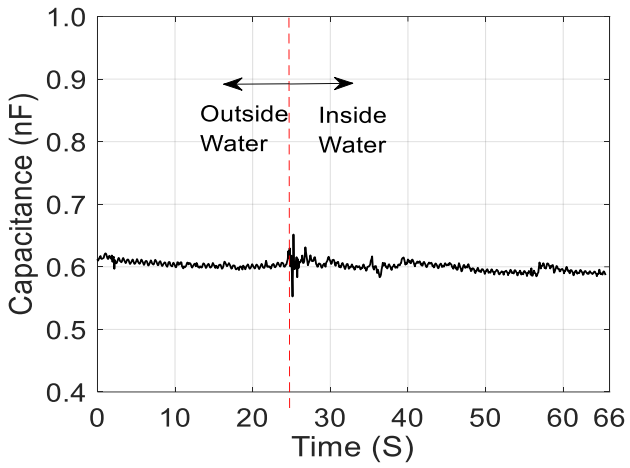

Figure 5-16 Sensor response after dipping into water

5.5 Conclusions

A quad-unit force sensing cell utilizing the paper-based electrolyte was fabricated, which simultaneously measures both normal and shear forces. The developed supercapacitive sensor can be integrated into an instrumented glove, which can be used to collect force information on fingertips for training domestic robots. The sensors were designed and fabricated using a combination of MEMS technologies and 3D printing. A model of the sensor was constructed using experimental data and neural network learning. The influence of parasitic noise was investigated by dipping the sensor inside water. The experimental results showed preliminary data to indicate that the sensor has high sensitivity and negligible parasitic capacitance. Future work could involve installing a set of the shear and normal force sensors on a glove and collecting force data to construct a database for training household robots.

Chapter 6

A Supercapacitive Strain Sensor with Ultra-High Sensitivity and Range

6.1 Introduction

Strain sensors that can measure size and deformation are of significant practical importance in wearable devices and biomedical skin applications. As evidenced by recent publications, there is significant current research interest in development of strain sensors that are flexible and highly stretchable [131]–[134]. For example, flexible transducers consisting of piezoresistive sensors made from metallic glass thin films [131], resistive strain sensors made using metallic nanoparticles [132], highly stretchable piezoelectric strain sensors designed using Kirigami [133], and resistive strain sensors made from carbon nanotube elastomers [134] have been reported. All of these devices use sophisticated fabrication technologies that typically require the use of clean rooms.

On the other hand, sensors made using paper as a substrate, with/without the use of cleanrooms, have been reported for applications such as microfluidics [57], [60], biosensing of analytes [66][135] and printed microelectronics [64]. Paper offers the advantages of being inexpensive, lightweight, environmentally friendly and easy to use [136]. Mechanical strain sensors have also been previously fabricated using paper-based substrates. In these previous sensors, functional resistive materials such as patterned carbon

or graphite are added on top of paper substrates. As the paper is bent or stretched to generate a strain, a change in the resistance of the functional materials is experienced. However, currently available paper-based strain sensors suffer from inadequate range and sensitivity. For example, a flexible and degradable resistive strain sensor on a paper substrate was reported in 2017 [71] that can detect strains as small as 0.2% but has a low sensing range (< 1%) due to the limited stretchability of the paper. Another flexible and printable paper-based strain sensor using patterned graphite film [137] has an improved resolution of 0.038%, but its sensing range is limited to less than 1%. Similarly, a strain sensor using a graphite-pencil to draw on a Xerox paper forming a resistive stripe was fabricated with high sensitivity but has highly limited range [138]. Strain sensors based on highly stretchable piezoresistive graphene-nanocellulose nanopaper [139] were also developed. They can be stretched to 100% but cannot provide adequate resolution and sensitivity with a gauge factor of only 2 at 5%. Besides, piezoresistive strain sensors typically suffer from drifting [140], [141].

In this chapter, a strain sensor based on a supercapacitive sensing mechanism using functionalized paper is fabricated. The new sensor provides ultra-high sensitivity, and at the same time, large sensing range. Supercapacitors have previously been mostly explored to be used as energy storage devices [2], and have only recently been used as force sensors [142]–[144]. They have never been utilized for strain sensing in literature before.

6.2 Sensing Principle of Supercapacitive Strain Sensor

The new physical sensing principle used for the measurement of strain is as follows: A solid-state paper-based electrolyte is pre-strained and sandwiched between two cylindrical electrodes. The initial thickness of the electrolyte is larger than the fixed gap between the two electrodes as shown in Figure 6-1 (a). When the electrolyte gets stretched in response to strain, the thinning of the electrolyte leads to a decrease in the contact area with metallic electrodes, as shown in Figure 6-1 (b), consequently resulting in a decrease in capacitance. Embodiments of the strain sensor are shown in Figure 6-2.

The proposed sensing mechanism requires a highly flexible and stretchable electrolyte.

Ionic-gel electrolytes that incorporate ionic liquid into a cross-linkable polymer matrix have been shown previously to provide both mechanical stability and high electrical conductivity [74], [75], [145] as discussed in Chapter 3. A traditional ionic gel has very limited flexibility and stretchability (maximum strain is about 13%). By incorporating cellulosic materials into the ionic-gel [84], [85], the weakened crystallinity of the polymer results in an improvement in the softness and extensibility properties of the paper-based solid electrolyte film. Thus, the paper-based solid electrolyte can be stretched to 32%. However, in order to be used in a strain sensor, the stretchability of the solid electrolyte needs to be further extended.

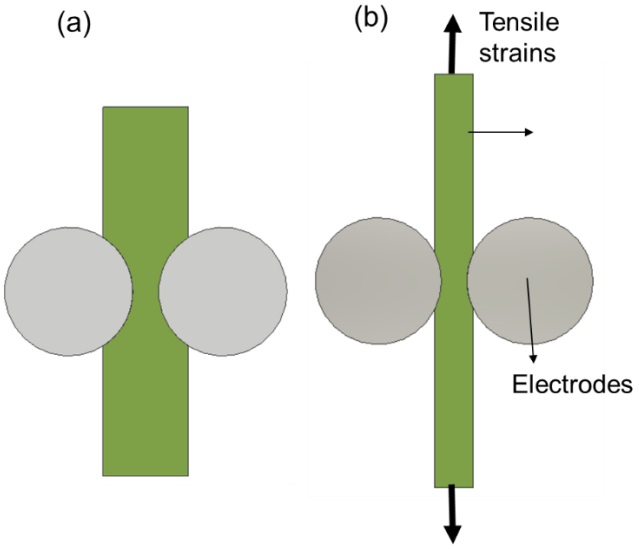

Figure 6-1 Mechanism of the paper-based strain sensor (a) before stretching, and (b) after stretching

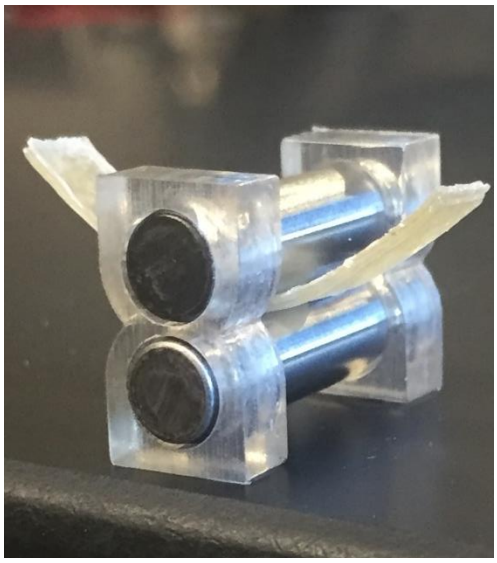

Figure 6-2 A prototype of the strain sensor

6.3 Paper-Based Solid Electrolyte Strengthened with Silicate Nanoparticles

The paper-based electrolyte discussed in section 3.2.2 is further strengthened by embedding silicate nanoparticles into the paper-based ionic gel matrix. Despite the many advantages of PEG-based electrolyte discussed in Chapter 3, they lack high toughness which limit their application in strain sensor. Among a variety of nanoparticles, silicates such as Laponite have been used to design and develop mechanically strong nanocomposite polymer hydrogel [146]–[148]. Laponite consists of synthetic and charged silicate nanodiscs, the chemical composition of which is $(Na^{+}_{0.7}7[(Mg_{5.5}Li_{0.3})Si_8O_{20}(OH)_4]^{-}_{0.7})$, and the dissolution products include $Na^{+}, Si(OH)_4, Mg^{2+}, Li^{+}$. After incorporating silicate nanoparticles into the PEG network, there are physical and covalent crosslinking between silicate particles and polymer chains, resulting in mechanically strong polymer network [149], [150]. Besides, under stress, the presence of nanoparticles promotes the debonding of the polymer from the nanoparticles, creating local voids that dissipate energy, and stop crack propagation [151], [152].

6.3.1 Fabrication of the Strengthened Solid Electrolyte

The ionic gel was mixed with silicate nanoparticles before being brushed on to the filter paper. The detailed fabrication process is as follows: 0.2g silicate nanoparticles (Laponite RDS, pellets size ~20-25nm) were mixed in 6.5g DI water using Vortex and sonication (2hrs). A clear solution was obtained. Then, 1g ionic liquid (1-ethyl-3-methylimidazolium tricyanomethanide, IOLITEC Inc.), 0.8g PEG diacrylate (PEGDA, Mw = 575 g mol^{-1}) monomers (Sigma–Aldrich), and 0.2g photo initiator (2-hydroxy-2-methylpropiophenone, Sigma–Aldrich) were added to the solution. The mixture was put into a mixer for mixing and defoaming for 20mins and stirred overnight. A free-flowing gel with light white color was obtained as shown in Figure 6-3. The addition of silicate nanosphere to the prepolymer solutions results in a decrease in optical transmittance. This is due to the formation of micro-sized silicate aggregates that scatter visible light [153]. The gel was brushed onto the filter paper (Millipore, 0.45μm HATF) and exposed under the UV light for 1 min. As shown in Figure 6-4, right after brushing the gel onto the filter paper and UV exposure, it starts turning transparent slowly as the filter paper gradually dissolves in the ionic gel, as seen in Figure 6-4. After 2 hours at room temperature, the water evaporates, the filter paper is fully dissolved in the ionic gel, and the electrolyte turns into a clear film. A real photo of the nanoparticle-strengthened electrolyte film is shown in the last picture in Figure 6-4 and can be seen to be a transparent thin film.

Figure 6-3 A photograph of ionic gel mixture with silicate nanoparticles

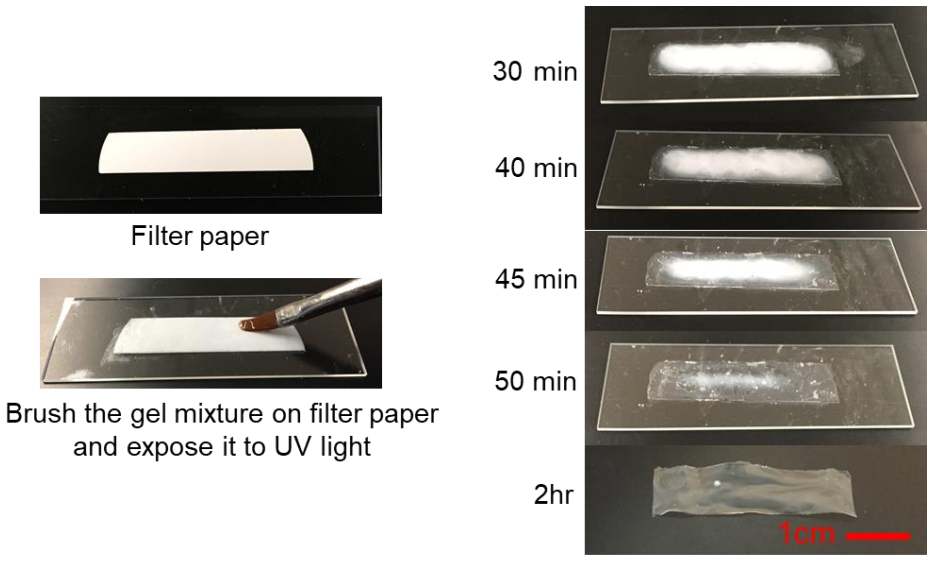

Figure 6-4 Photographs showing the dissolving of filter paper in the ionic gel mixture.

6.3.2 Mechanical Properties of the Strengthened Solid Electrolyte

The deformation response of the nanoparticle strengthened electrolyte film was tested on a DMA machine (RSA-G2, TA Instruments) by measuring stress and strain while stretching the film until failure occurs. A comparison with the stretchability of the original ionic gel electrolyte (without cellulose) and of the modified paper-based electrolyte without nanoparticles is shown in Figure 6-5. As can be inferred from the results in Figure 6-5, the paper-based electrolyte film can achieve a maximum elongation strain of 32% that is 2.5 times larger in comparison with the unmodified standard ionic gel electrolyte without cellulose [144]. After adding silicate nanoparticles, the stretchability and toughness of the strengthened paper-based electrolyte are additionally improved. The strengthened electrolyte can be stretched to more than 110% strain before failure occurs. The Young's modulus of the strengthened electrolyte film is increased to 14MPa. Thus, the strengthened electrolyte film is highly suitable for the strain sensor proposed in this chapter. It should be noted that by changing the ratio of silicate nanoparticles added to the electrolyte, the mechanical properties of the electrolyte film can be variably adjusted.

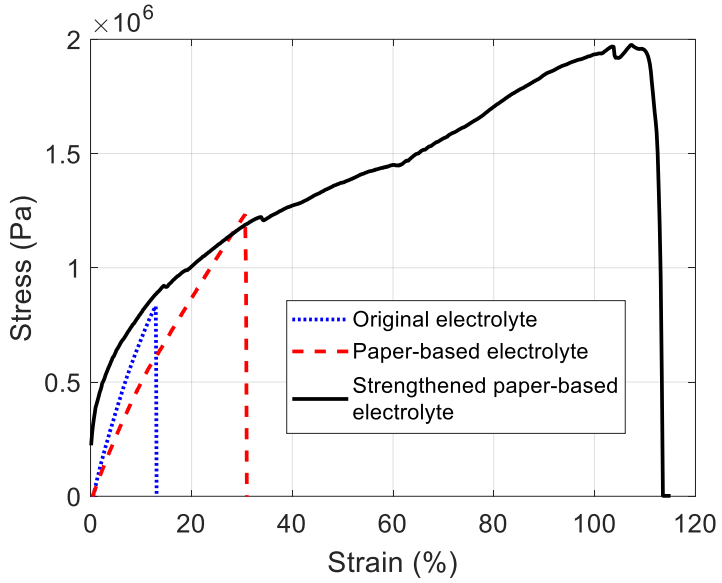

Figure 6-5 Mechanical properties of the strengthened film

6.4 Strain Sensors Based on the Strengthened Electrolyte Film

The nanoparticle strengthened electrolyte film was used to fabricate a supercapacitive strain sensor. Several electrolyte films were stacked together to increase the thickness and create a thick electrolyte. Then the electrolyte was pre-strained and assembled between two cylindrical electrodes, as the prototype shown in Figure 6-2. However, this prototype is not suitable for real applications due to its large size. Therefore, the supercapacitive strain sensor is further downsized and redesigned as shown in Figure 6-6. The sensor consists of a thick electrolyte slab made of multiple stacked strengthened electrolyte films, compressed between two electrodes made of stainless-steel pins, which are fixed by two holders at both ends of the pins. The gap between the two electrode pins is smaller than the thickness of the electrolyte film. Due to the pre-strain in the electrolyte, any applied tensile strain will stretch the electrolyte, and reduce the contract area between the electrolyte and the electrodes, which gives a measurable signal proportional to strain.

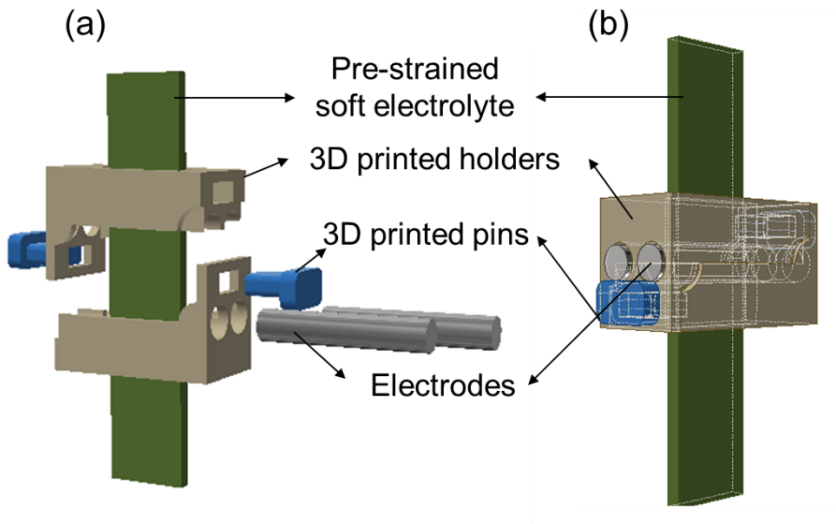

Figure 6-6 The schematic of a smaller strain sensor: (a) exploded view (b) assembled sensor.

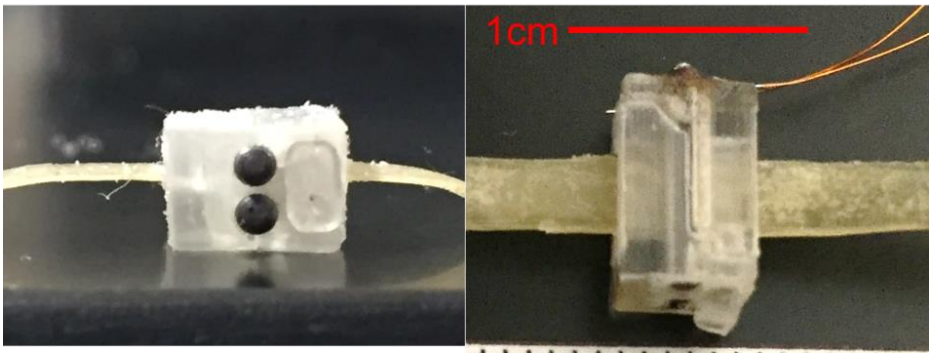

Figure 6-7 Photos of the assembled strain sensor

To prevent the electrolyte from bending while stretching in real world applications, two identical 3D printed holders (Stratasys, Veroclear) were custom designed. First, the strain sensor was scaled down using shorter pins and the 3D printed holders were used both to assemble the pins and electrolyte together and to keep the electrolyte straight without bending near the region of contact with electrodes, as shown in Figure 6-6. Five layers of paper were brushed with the gel mixture embedded with silicate nanoparticles and then stacked together. When tensile loads are applied at both ends of the electrolyte, the thinning of the film leads to a decrease in the contact area between the electrodes and the electrolytes, consequently a decrease in capacitance. The thickness of the stacked electrolyte is about 0.45mm, while the gap between the two electrodes is about 0.3mm. The electrodes (Dowel Pin, Steel,1.5x10mm) used here were 1.5mm in diameter bought from a local hardware

store. In fact, the entire sensor was made using just paper and a few dollars of purchases from a local hardware store. Real photos of the assembled strain sensor are shown in Figure 6-7. The convenience, easy fabrication and low cost of the sensor are its advantages. The same sensor could be micro-fabricated in a clean room and could then be made very small, but then it would no longer have the advantages of easy fabrication without cleanrooms.

6.5 Laboratory Testing and Sensor Performance

6.5.1 Strain Sensor Response

The sensor was first tested as shown in Figure 6-8 using a custom-designed laboratory setup. A force gauge (Torbal, FC50, $50NX0.01N$) was installed on a translational stage which can move along Z-axis. An upper clamp was installed on the shaft of the force gauge, while a lower clamp was installed on a translational and rotational stage. The strain sensor was held in these two clamps as shown in Figure 6-8(b). While gradually moving the force gauge up by turning the knob on the translational stage in steps of 10 um, the force readings from the force gauge were recorded and at the same time the capacitance changes were recorded using a multimeter (Rigol, DM3068). The distance changes were read from the vernier (Newport SM-13) on the translational stage.

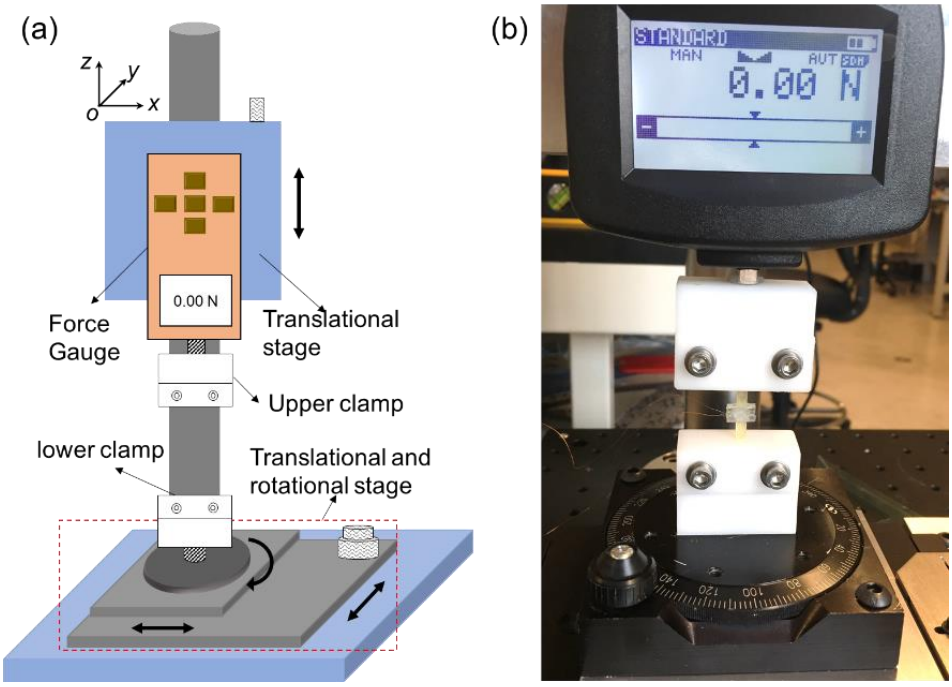

Figure 6-8 (a) Schematic and (b) photo of the calibration setup.

The results are shown in Figure 6-9 (a) and (b). As the applied force increases, the capacitance decreases due to the thinning of the electrolyte film, which leads to smaller contact area between the electrode pins and the electrolyte. Above a strain of ~ 25%, the capacitance saturates, where the thickness of the film has decreased to become close to the value of the gap between the two electrode pins. While the capacitance has a nonlinear relationship with strain response, it is easy to fit a nonlinear polynomial calibration curve to the capacitance readings so that the output of the polynomial has a linear relationship with strain. It should be noted that theoretically the range of the sensor can be further extended by decreasing the gap further between the two electrode pins, since the maximum strain that the electrolyte film can handle is more than 110% as shown in Figure 6-5.

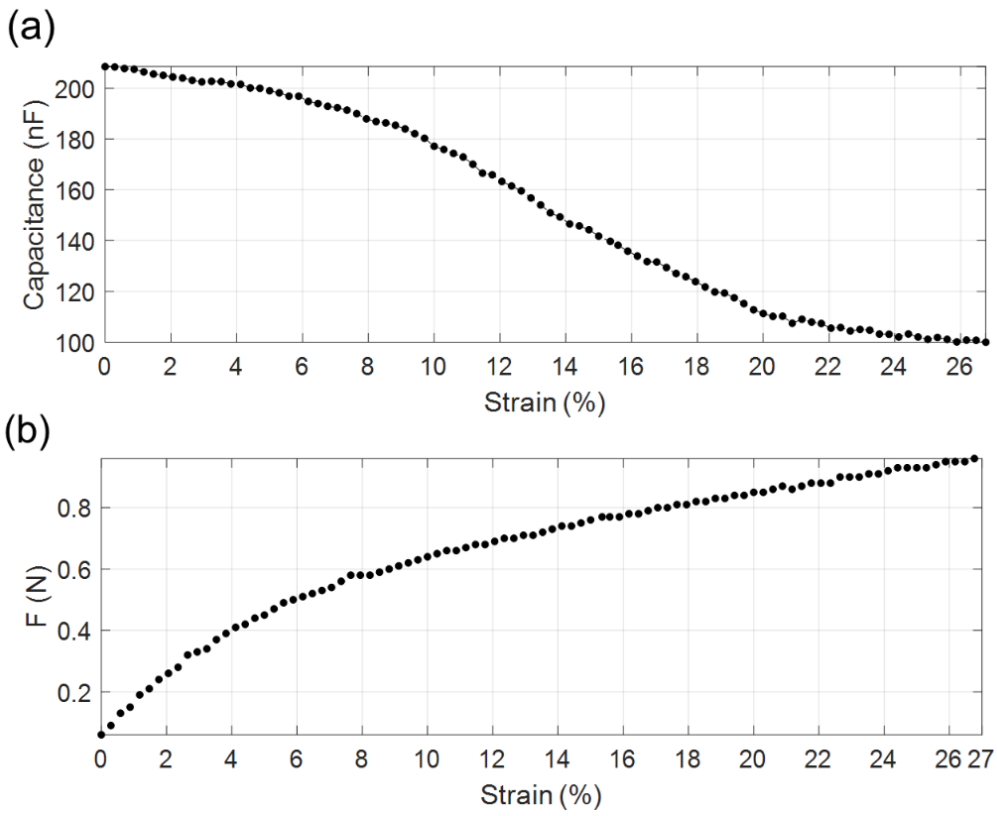

Figure 6-9 Force response curves of the strain sensor.

The supercapacitive strain sensor was glued to an elastic band using super-glue (Loctite, Ultragel Control) as a size sensor. Two Velcro pieces were fixed at the two ends of the elastic band. The band was wrapped around a conical, which has a few rings of different circumferences, as shown in Figure 6-10 (a). The diameter of the rings increases by 1mm from top to bottom. The test started from a ring of 70 mm in diameter with pre-tension, and then the band was moved down step-by-step to next ring until a ring of 80mm in diameter. The capacitance was recorded at every ring. The results are shown in Figure 6-10 (b). As the band is moved down the conical, the capacitance decreases.

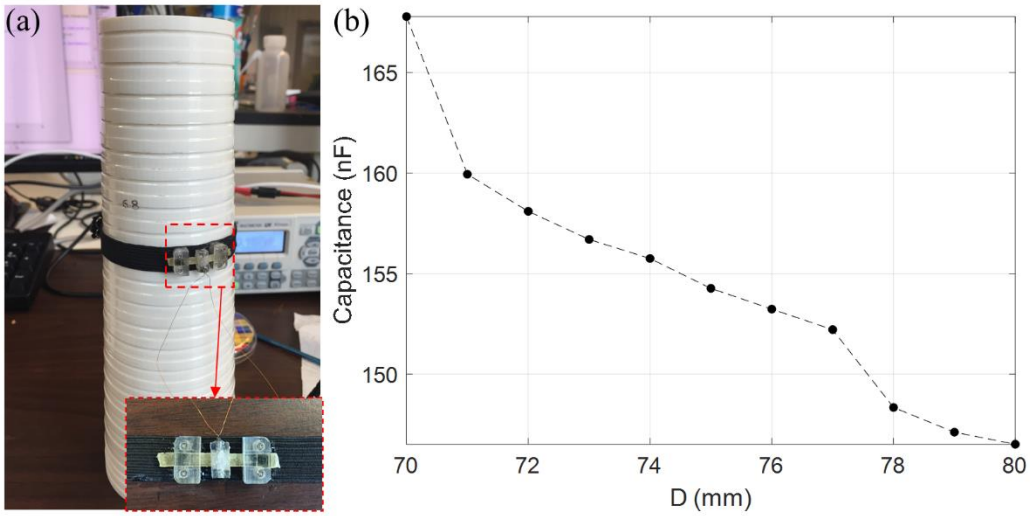

Figure 6-10 Photo of the strain sensor wrapping around a conical. (b) Strain sensor response on a conical

6.5.2 Cantilever Test

To further investigate the sensitivity of the sensor and its capability to measure very small strains, another laboratory set-up was designed by installing the strain sensor on an aluminum ruler used as a cantilever (Figure 6-11 (a)). The sensor was clipped at both ends of the electrolyte film using two 3D printed clamps, which were glued to the ruler using a UV curable glue (RapidFix, liquid plastic adhesive), as shown in Figure 6-11(b). Weights ranging from 0g to 513g were added in steps of 50g at the free end of the cantilever. The capacitance from the strain sensor was recorded. The strain of the surface where the sensor is installed is estimated using:

$$\varepsilon = \frac{\sigma}{E} \tag{6-1}$$

where E is the Young's modulus of the cantilever, and the stress σ on the ruler surface at the location where the sensor is installed can be expressed as:

$$\sigma = \frac{mglh}{2I} \tag{6-2}$$

where h is the thickness of the ruler. The moment in the ruler at the fixed end is $M = mgl$, where m is the mass of the weight, l is the distance from the sensor to the point where load is applied and I is the moment of inertia.

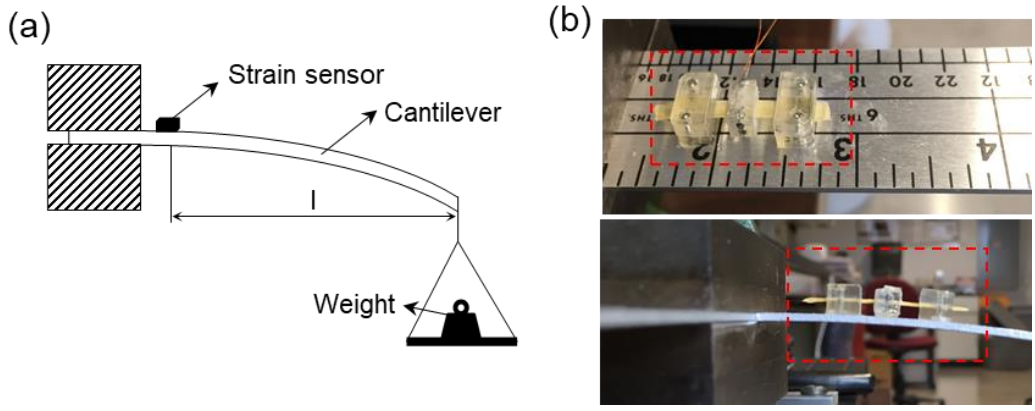

Figure 6-11 (a) A cantilever with end load. (b) Strain sensor installed on a ruler cantilever.

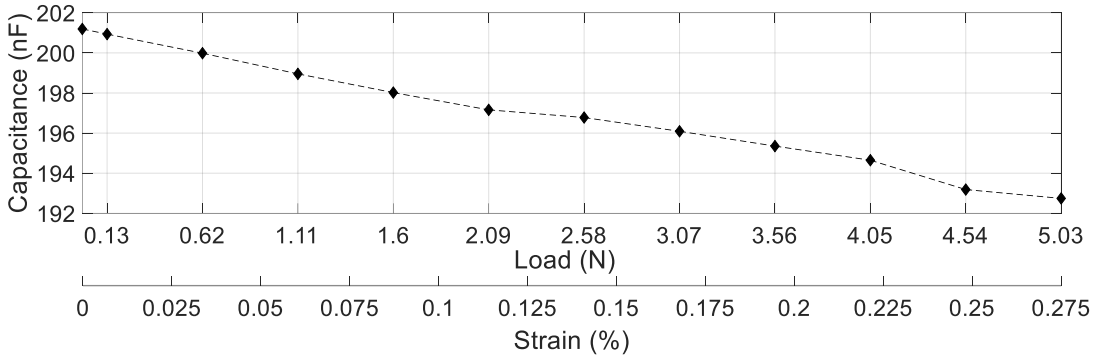

Figure 6-12 Strain sensor response on the gradually loaded ruler cantilever

For the cantilever with a rectangular cross section of height h and width b, the moment of inertia I is:

$$I = \frac{bh^3}{12} \tag{6-3}$$

By combining all the equations above, the strain on the surface where the sensor is installed can be expressed as:

$$\varepsilon = \frac{6mgFl}{Ebh^2} \tag{6-4}$$

The sensor response to the strain obtained from Equation (6-4) is shown in Figure 6-12. The change in capacitance with the load is also shown in the same figure. As the load increases, the capacitance from the supercapacitive strain sensor decreases. The change in capacitance with the load is also shown in the same figure. The sensor is very sensitive and can differentiate a strain less than 0.025 % (since a capacitance change of 50 pF can be

measured very accurately using commercial inexpensive capacitance measurement chips). The sensitivity of the sensor is between 14.3nF and 55nF per 1% strain.

6.6 Applications of the Strain Sensor

6.6.1 Leg Size Sensor

A number of diseases can lead to fluid accumulation and swelling in the lower leg. Early detection of such leg swelling can be used to effectively predict potential health risks and allows for early intervention from medical providers [140]. The swelling of the leg produces a small change of the leg size. Hence a wearable leg size sensor that can automatically monitor the leg size in real-time can help monitor lower leg edema caused by many medical conditions such as heart failure, deep vein thrombosis, venous insufficiency, and hepatic disease [154], [155]. The elastic band with the strain sensor in Figure 6-10 was tested on the leg by sliding upwards, to simulate a leg size change, as shown in Figure 6-13 (a). The capacitance readings while moving the sensors are shown in Figure 6-13 (b). The sensor was kept at each position for a few seconds, during which the sensor response does not drift as shown in Figure 6-13 (b). The average capacitance at each position is shown in Figure 6-13 (c). While the sensor is moving up, the capacitance of the sensor decreases. The strain sensor can be used to monitor the leg size changes of a patient caused by fluid accumulation in the lower leg.

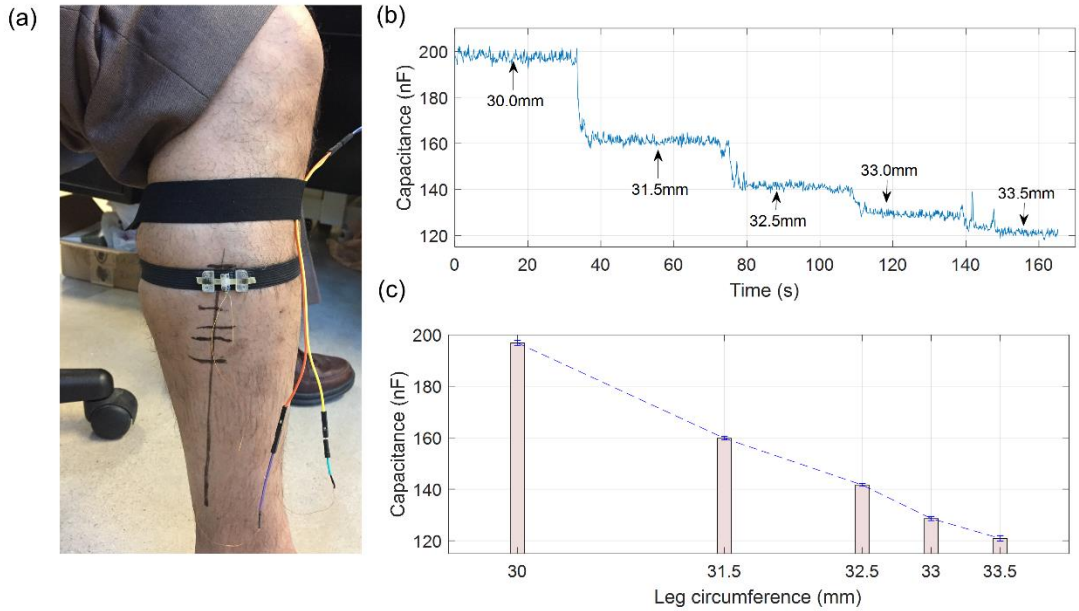

Figure 6-13 (a) Strain sensor used as size sensor wrapped around the leg. (b) Strain sensor response with the changing leg sizes. (c) Mean value of the capacitance changes

6.6.2 Respiratory Rate Measurement

Measurement of the respiratory rate is an important instrument for assessing the severity of many acute disease [156], [157]. The respiratory rate is often not measured in routine practice because its clinical utility is inadequately appreciated. Measuring the respiratory rate is recommended for outpatient patients with pneumonia to help with a decision on whether a patient should be admitted to hospital. In acute bronchial asthma, pulmonary embolism or heart failure, the respiratory rate is an important prognostic parameter as well. Monitoring the respiratory volume is also very important for some post-surgery patients such as cardiac surgery patients after extubation, post-operative patients with obstructive sleep apnea in, etc. [158], [159]. However, current methods of monitoring breathing require cumbersome, inconvenient, invasive, and often expensive devices [160], [161]. Here, the supercapacitive strain sensor is used to provide an easy and cheap way to measure the respiratory rate. It can not only measure the respiratory rate, but also provide a non-invasive, real time monitoring of the respiratory volume. Another strain sensor is fabricated using the same method and then glued to a long elastic band. This instrumented

band can be used to monitor respiration behavior when it is wrapped around the chest of humans as shown in Figure 6-14(a). Figure 6-14(b) shows the results of the instrumented band on a subject. The subject in this test gently breathed at the beginning for about 19s, and then started to take deep breaths. By analyzing the intervals and magnitude of the peaks, respiratory rate and volume information can be obtained.

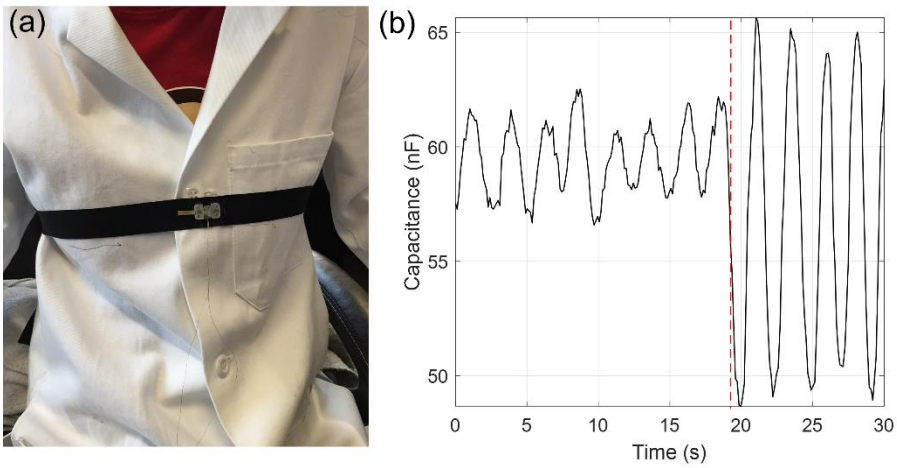

Figure 6-14 (a) An elastic band with the strain sensor wrapped around the chest. (b) Strain sensor response to changes in the respiratory rate and volume

6.7 Conclusions

A new method for fabricating flexible and stretchable solid-state electrolytes based on use of a paper substrate coated with a nanoparticle embedded ionic gel is presented. A strain sensor using this highly stretchable electrolyte which can provide both high sensitivity and high sensing range is developed. The strain sensor can measure strain as large as 25% and has distinctive detectability of micro-strain (0.025%). The sensor is fabricated without use of clean room facilities and by just using paper, ionic gel and simple metal pins as electrodes. The strain sensing principle presented in this chapter is a new and advantageous method of measuring strain.

Chapter 7

Conclusions

This dissertation developed force and strain monitoring sensors for biomedical applications based on a new supercapacitive sensing principle. The new sensors can enable wearable ambulatory health monitoring, home-based wellness assessment, and more effective clinical diagnostics. The supercapacitive sensors are based on a new paper-based solid-state electrolyte and its change in contact area with a pair of electrodes in response to force or strain. The supercapacitive sensors have very high sensitivity, can operate in liquid environments with negligible parasitic capacitance, and are easy to fabricate without requiring cleanroom facilities.

First, a novel paper-based solid electrolyte was developed to replace liquid state electrolytes normally utilized in supercapacitors. The novel electrolyte was fabricated by introducing active ionic materials into the porous matrix of filter paper and functionalizing the entire thickness of the paper. Paper dissolves in the ionic gel after determining the shape of the electrolytes, leaving behind transparent electrolytes with micro-structured fissures responsible for their high deformability, toughness and stretchability. Microstructures of the novel electrolyte were studied to understand the resulting improvement in mechanical properties.

Next, the influence of parasitic capacitance on the supercapacitive sensors was studied. Unlike conventional capacitive sensors, the supercapacitive sensors do not suffer from parasitic capacitance. On one hand, the nominal capacitance and sensitivity of a

supercapacitor are much higher than that of a capacitor, which makes the parasitic noise negligible. Also, less fringe effects exist for a supercapacitive sensor, resulting in a much smaller parasitic capacitance. The response of a fabricated supercapacitive sensor was recorded both in air and in water. Negligible capacitance difference was observed from the results. However, the capacitance of a traditional capacitive sensor of the same dimension increases by as much as 50% after immersion in water, caused by the parasitic noise. The two sensors were also tested inside a tissue. No additional capacitance could be observed for the supercapacitive sensor inside the tissue. When properly sealed, the sensors can thus operate in liquid environments with negligible parasitic capacitance and are therefore suitable for *in vivo* human health applications.

Next, diverse sensors of different configurations were constructed using the supercapacitive sensing principle to measure force. An instrumented urethral catheter based on supercapacitive sensors was developed for diagnostics of urinary incontinence. The sensors on the catheter utilized the flexible paper-based electrolyte and a fabrication process that included MEMS fabrication and 3D printing. Five distributed sensors were installed on the catheter body in order to measure pressure distribution inside a human urethra. Ex vivo and cuff test show that the catheter sensors respond to increasing pressure monotonically and in general have a sensitivity more than 1000 times than that of a catheter with traditional capacitive pressure sensors. Inside-water test shows that the catheter is suitable for in vivo use because of its negligible parasitic noise.

Exploiting the high sensitivity and range of the supercapacitive sensors, an integrated sensor was developed next to measure both normal and shear forces simultaneously. The measurement was enabled by using a miniaturized quad electrode structure and a soft deformable membrane with the paper-based electrolyte that creates different combinations of capacitances in the multiple electrodes in each sensing unit. The sensor's sensitivity to shear and normal force was high, with negligible influence of parasitic capacitance. A custom-designed test setup was used to collect data on the sensor. Based on the collected experimental datasets, a neural network was used to learn a model of the sensor response to various distributions of normal and shear forces. The model obtained from the machine learning provided accurate estimates of normal and shear forces when arbitrary forces were

applied on the sensor involving data not utilized in training the neural network. A set of such soft supercapacitive sensors can be installed on an instrumented glove to measure normal and shear forces on the fingertips, both in humans and in robotic applications.

Finally, a strain sensor was developed utilizing the supercapacitive sensing principle. It consisted of a paper-based solid-state electrolyte which deforms in response to strain and changes its contact area with a pair of electrodes. This results in a highly sensitive capacitance change in a double-layer supercapacitor. The paper-based solid electrolyte was further strengthened utilizing silicate nanoparticles to extend the maximum strain it could experience without failure. Test results showed that the strain sensor could provide an extremely high measurement resolution of 0.025% strain. The sensor was incorporated on a wearable elastic band that can automatically monitor the leg size in a human subject for use in home-based edema monitoring applications. The new sensor can replace more expensive traditional strain sensors.

In summary, the new supercapacitive sensors developed in this dissertation have both high range and a sensitivity several orders of magnitude (at least 1000 times) higher than traditional MEMS capacitive sensors, in spite of their being easily fabricated from paper with no cleanroom facilities. With low cost, easy fabrication, and ultra-high sensitivity, this method of sensing holds the promise to potentially transform the standard practice in fabricating mechanical sensors.

The contributions of this dissertation include development of a new sensing mechanism consisting of the use of a supercapacitor as the sensing device, the development of a new paper-based electrolyte with high flexibility, and development of many embodiments of these force/strain sensors including devices made entirely from paper and copper tape, novel normal-shear force sensors, a urethral catheter with distributed force sensors, and a wearable strain sensor for leg size monitoring.

Bibliography

[1] R. Kötz, M. Carlen, and M. Carlen, "Principles and applications of electrochemical capacitors," *Electrochim. Acta*, vol. 45, pp. 2483–2498, 2000.

[2] B. E. Conway, *Electrochemical Supercapacitors*, vol. 1. 1999.

[3] G. Wang, L. Zhang, and J. Zhang, "A review of electrode materials for electrochemical supercapacitors.," *Chem. Soc. Rev.*, vol. 41, no. 2, pp. 797–828, Jan. 2012.

[4] K. Kierzek, E. Frackowiak, G. Lota, G. Gryglewicz, and J. Machnikowski, "Electrochemical capacitors based on highly porous carbons prepared by KOH activation," *Electrochim. Acta*, vol. 49, no. 4, pp. 515–523, 2004.

[5] B. Fang and L. Binder, "A modified activated carbon aerogel for high-energy storage in electric double layer capacitors," *J. Power Sources*, vol. 163, no. 1, pp. 616–622, 2006.

[6] B. Xu *et al.*, "Highly mesoporous and high surface area carbon: A high capacitance electrode material for EDLCs with various electrolytes," *Electrochem. commun.*, vol. 10, no. 5, pp. 795–797, 2008.

[7] S. Shiraishi, H. Kurihara, K. Okabe, D. Hulicova, and A. Oya, "Electric double layer capacitance of highly pure single-walled carbon nanotubes (HiPco^{TM}Buckytubes^{TM}) in propylene carbonate electrolytes," *Electrochem. commun.*, vol. 4, no. 7, pp. 593–598, 2002.

[8] Y.-S. Kim, K. Kumar, F. T. Fisher, and E.-H. Yang, "Out-of-plane growth of CNTs on graphene for supercapacitor applications," *Nanotechnology*, vol. 23, no. 1, p. 015301, 2011.

[9] P. Simon and Y. Gogotsi, "Materials for electrochemical capacitors," *Nat. Mater.*,

vol. 7, no. 11, pp. 845–854, 2008.

[10] Y. Zhang and R. Rajamani, “High-voltage thin-film supercapacitor with nano-structured electrodes and novel architecture,” *Technology*, vol. 04, no. 01, pp. 55–59, 2016.

[11] B. Kim, S. Sy, A. Yu, and J. Zhang, “Electrochemical Supercapacitors for Energy Storage and Conversion,” *Handb. Clean Energy Syst.*, pp. 1–25, 2015.

[12] Y. Zhang *et al.*, “Progress of electrochemical capacitor electrode materials: A review,” *Int. J. Hydrogen Energy*, vol. 34, no. 11, pp. 4889–4899, Jun. 2009.

[13] S.-B. Ma *et al.*, “A novel concept of hybrid capacitor based on manganese oxide materials,” *Electrochem. commun.*, vol. 9, no. 12, pp. 2807–2811, 2007.

[14] H. Seidel, H. Riedel, R. Kolbeck, G. Mück, W. Kupke, and M. Königer, “Capacitive silicon accelerometer with highly symmetrical design,” *Sensors Actuators A Phys.*, vol. 21, pp. 312–315, 1990.

[15] F. Rudolf, “A Micromechanical Capacitive Accelerometer with a Two-Point Inertial-Mass Suspension,” vol. 4, no. 1983, pp. 191–198, 2000.

[16] W. Li, Z. Song, X. Li, L. Che, and Y. Wang, “A novel sandwich capacitive accelerometer with a double-sided 16-beam-mass structure,” *Microelectron. Eng.*, vol. 115, pp. 32–38, 2014.

[17] H. Johari, J. Shah, and F. Ayazi, “High Frequency XYZ-Axis Single-Disk Silicon Gyroscope,” *Micro Electro Mech. Syst. MEMS 2008 IEEE*, no. 100, pp. 2008–2011, 2008.

[18] H. Johari and F. Ayazi, “Capacitive Bulk Acoustic Wave Silicon Disk Gyroscopes,” *2006 Int. Electron Devices Meet.*, no. 111, pp. 1–4, 2006.

[19] P. Eswaran and S. Malarvizhi, “MEMS Capacitive Pressure Sensors : A Review on Recent Development and Prospective,” *Int. J. Eng. Technol.*, vol. 5, no. 3, pp. 2734–2746, 2013.

[20] W.P. Eaton and J. H.Smith, “Micromachined pressure sensors : review and recent developments,” *Smart Mater. Struct.*, vol. 6, pp. 530–539, 1997.

[21] R. Tan, P. Benharash, P. Schulam, and J. J. Schmidt, “Implantable electrolyte conductance-based pressure sensing catheter, II. Device construction and testing,”

Biomed. Microdevices, vol. 15, no. 6, pp. 1035–1041, 2013.

[22] P. J. Chen, D. C. Rodger, S. Saati, M. S. Humayun, and Y. C. Tai, "Microfabricated implantable parylene-based wireless passive intraocular pressure sensors," *J. Microelectromechanical Syst.*, vol. 17, no. 6, pp. 1342–1351, 2008.

[23] P. Roriz, O. Frazão, A. B. Lobo-Ribeiro, J. L. Santos, and J. a. Simões, "Review of fiber-optic pressure sensors for biomedical and biomechanical applications," *J. Biomed. Opt.*, vol. 18, no. 5, p. 050903, 2013.

[24] P. Yameogo, U. Heiba, M. Al Bahri, and P. Pons, "Self calibrating pressure sensor for biomedical applications," *2009 IEEE Sensors*, 2009.

[25] Y. Tai, M. Mulle, I. Aguilar Ventura, and G. Lubineau, "A highly sensitive, low-cost, wearable pressure sensor based on conductive hydrogel spheres," *Nanoscale*, vol. 7, no. 35, pp. 14766–14773, 2015.

[26] C.-C. Chiang, C.-C. K. Lin, and M.-S. Ju, "An implantable capacitive pressure sensor for biomedical applications," *Sensors Actuators A Phys.*, vol. 134, no. 2, pp. 382–388, 2007.

[27] D. B. Seo and R. Shandas, "Design and Simulation of a Mems-Based Comb-Drive Pressure Sensor for Pediatic Post-Operative Monitoring Applications," *Summer Bioeng. Conf. June*, no. 1, pp. 25–29, 2003.

[28] A. Sepúlveda *et al.*, "Nanocomposite Flexible Pressure Sensor for Biomedical Applications," *Procedia Eng.*, vol. 25, pp. 140–143, 2011.

[29] K. F. Lei, K.-F. Lee, and M.-Y. Lee, "Development of a flexible PDMS capacitive pressure sensor for plantar pressure measurement," *Microelectron. Eng.*, vol. 99, pp. 1–5, 2012.

[30] M. Mizushima *et al.*, "Flexible and capacitive tactile sensor sheet," *2014 Int. Conf. Electron. Packag.*, no. 1, pp. 756–759, 2014.

[31] T. Kasahara *et al.*, "Simple and Low-Cost Fabrication of Flexible Capacitive Tactile Sensors," *Jpn. J. Appl. Phys.*, vol. 50, p. 016502, 2011.

[32] M.-X. Zhou, Q.-A. Huang, M. Qin, and W. Zhou, "A novel capacitive pressure sensor based on sandwich structures," *J. Microelectromechanical Syst.*, vol. 14, no. 6, pp. 1272–1282, 2005.

[33] J. Han and M. A. Shannon, “Smooth contact capacitive pressure sensors in touch- and peeling-mode operation,” *IEEE Sens. J.*, vol. 9, no. 3, pp. 199–206, 2009.

[34] W. H. Ko and Q. Wang, “Touch mode capacitive pressure sensors,” *Sensors Actuators, A Phys.*, vol. 75, no. 3, pp. 242–251, 1999.

[35] L. Minghui, D. Jiahao, and G. Shiqiao, “Novel touch mode capacitive pressure sensor based on SiC,” *IEEE 2011 10th Int. Conf. Electron. Meas. Instruments*, vol. 1, pp. 333–335, 2011.

[36] T. Pedersen, G. Fragiacomo, O. Hansen, and E. V. Thomsen, “Highly sensitive micromachined capacitive pressure sensor with reduced hysteresis and low parasitic capacitance,” *Sensors Actuators, A Phys.*, vol. 154, pp. 35–41, 2009.

[37] G. Fragiacomo, T. Pedersen, O. Hansen, and E. V. Thomsen, “Intrinsic low hysteresis touch mode capacitive pressure sensor,” *2010 IEEE Sensors*, pp. 2279–2282, 2010.

[38] G. Fragiacomo, T. Ansbæk, T. Pedersen, O. Hansen, and E. V. Thomsen, “Analysis of small deflection touch mode behavior in capacitive pressure sensors,” *Sensors Actuators A Phys.*, vol. 161, no. 1–2, pp. 114–119, 2010.

[39] E. G. Bakhoum and M. H. M. Cheng, “Novel Capacitive Pressure Sensor,” *J. Microelectromechanical Syst.*, vol. 19, no. 3, pp. 443–450, 2010.

[40] H. Z. Zhang, Q. Y. Tang, and Y. C. Chan, “Development of a versatile capacitive tactile sensor based on transparent flexible materials integrating an excellent sensitivity and a high resolution,” *AIP Adv.*, vol. 2, no. 2, p. 022112, 2012.

[41] V. Leus and D. Elata, “Fringing field effect in electrostatic actuators,” *Tech. Inst. Technol.*, no. May, pp. 2004–2, 2004.

[42] E. Ghafar-Zadeh and M. Sawan, “CMOS Capacitive Sensors for Lab-On-Chip Applications: A Multidisciplinary Approach,” p. 146, 2010.

[43] P. H. Bezuidenhout, J. Schoeman, and T. H. Joubert, “The modelling of a capacitive microsensor for biosensing applications,” in *Sensors, MEMS and Electro-Optical Systems*, 2014, vol. 9257, p. 92570P.

[44] A. Burke, “Ultracapacitors: Why, how, and where is the technology,” *J. Power Sources*, vol. 91, no. 1, pp. 37–50, 2000.

[45] D.-Y. Cho, K. Eun, S.-H. Choa, and H.-K. Kim, “Highly flexible and stretchable carbon nanotube network electrodes prepared by simple brush painting for cost-effective flexible organic solar cells,” *Carbon N. Y.*, vol. 66, pp. 530–538, Jan. 2014.

[46] M. Beidaghi and C. Wang, “Micro-Supercapacitors Based on Interdigital Electrodes of Reduced Graphene Oxide and Carbon Nanotube Composites with Ultrahigh Power Handling Performance,” *Adv. Funct. Mater.*, vol. 22, no. 21, pp. 4501–4510, 2012.

[47] J. Liu, F. Mirri, M. Notarianni, M. Pasquali, and N. Motta, “High performance all-carbon thin film supercapacitors,” *J. Power Sources*, vol. 274, pp. 823–830, 2014.

[48] B. Nie, S. Xing, J. D. Brandt, and T. Pan, “Droplet-based interfacial capacitive sensing.,” *Lab Chip*, vol. 12, no. 6, pp. 1110–8, Mar. 2012.

[49] M. N. M. Nawi, A. A. Manaf, M. F. A. Rahman, M. R. Arshad, and O. Sidek, “One-side-electrode-type fluidic-based capacitive pressure sensor,” in *IEEE Sensors Journal*, 2013, vol. 15, no. 3.

[50] H. Yu *et al.*, “Capacitive micromachined ultrasonic transducer based tilt sensing,” *Appl. Phys. Lett.*, vol. 101, no. 15, p. 153502, 2012.

[51] B. S. Kang *et al.*, “Capacitance pressure sensor based on GaN high-electron-mobility transistor-on-Si membrane,” *Appl. Phys. Lett.*, vol. 86, no. 25, p. 253502, 2005.

[52] M. Ahmadi, R. Rajamani, G. Timm, and A. S. Sezen, “Flexible Distributed Pressure Sensing Strip for a Urethral Catheter,” *J. Microelectromechanical Syst.*, vol. 24, no. 6, pp. 1840–1847, 2015.

[53] J. D. Suter, C. J. Hohimer, J. M. Fricke, J. Christ, K. Hanseup, and a T. Evans, “Principles of Meniscus-based MEMS Gas or Liquid Pressure Sensors,” *J. Microelectromechanical Syst.*, vol. 22, no. 3, pp. 670–677, 2013.

[54] H. Tao *et al.*, “Metamaterials on paper as a sensing platform,” *Adv. Mater.*, vol. 23, no. 28, pp. 3197–3201, 2011.

[55] D. Tobjörk and R. Österbacka, “Paper electronics,” *Advanced Materials*, vol. 23, no. 17. pp. 1935–1961, 2011.

[56] M. M. Hamedi, A. Ainla, F. Güder, D. C. Christodouleas, M. T. Fernández-Abedul,

and G. M. Whitesides, “Integrating Electronics and Microfluidics on Paper,” *Adv. Mater.*, pp. 5054–5063, 2016.

[57] A. W. Martinez, S. T. Phillips, and G. M. Whitesides, “Three-dimensional microfluidic devices fabricated in layered paper and tape,” *Proc. Natl. Acad. Sci.*, vol. 105, no. 50, pp. 19606–19611, 2008.

[58] G. V. Martins, A. P. M. Tavares, E. Fortunato, and M. G. F. Sales, “Paper-Based Sensing Device for Electrochemical Detection of Oxidative Stress Biomarker 8-Hydroxy-2′-deoxyguanosine (8-OHdG) in Point-of-Care,” *Sci. Rep.*, vol. 7, no. 1, pp. 1–10, 2017.

[59] A. C. Marques *et al.*, “Office paper platform for bioelectrochromic detection of electrochemically active bacteria using tungsten trioxide nanoprobes,” *Sci. Rep.*, vol. 5, pp. 1–7, 2015.

[60] X. Li, J. Tian, G. Garnier, and W. Shen, “Fabrication of paper-based microfluidic sensors by printing,” *Colloids Surfaces B Biointerfaces*, vol. 76, no. 2, pp. 564–570, 2010.

[61] F. Güder *et al.*, “Paper-Based Electrical Respiration Sensor,” *Angew. Chemie - Int. Ed.*, vol. 55, no. 19, pp. 5727–5732, 2016.

[62] Q. Zhong *et al.*, “Paper-Based Active Tactile Sensor Array,” *Adv. Mater.*, vol. 27, no. 44, pp. 7130–7136, 2015.

[63] A. D. Mazzeo *et al.*, “Paper-based, capacitive touch pads,” *Adv. Mater.*, vol. 24, no. 21, pp. 2850–2856, 2012.

[64] G. Grau, R. Kitsomboonloha, S. L. Swisher, H. Kang, and V. Subramanian, “Printed transistors on paper: Towards smart consumer product packaging,” *Adv. Funct. Mater.*, vol. 24, no. 32, pp. 5067–5074, 2014.

[65] S. K. Mahadeva, K. Walus, and B. Stoeber, “Paper as a platform for sensing applications and other devices: A review,” *ACS Appl. Mater. Interfaces*, vol. 7, no. 16, pp. 8345–8362, 2015.

[66] Y. Xia, J. Si, and Z. Li, “Fabrication techniques for microfluidic paper-based analytical devices and their applications for biological testing: A review,” *Biosens. Bioelectron.*, vol. 77, pp. 774–789, 2016.

[67] D. D. Liana, B. Raguse, J. Justin Gooding, and E. Chow, “Recent advances in paper-based sensors,” *Sensors (Switzerland)*, vol. 12, no. 9, pp. 11505–11526, 2012.

[68] Y. Long Han, H. Liu, C. Ouyang, T. Jian Lu, and F. Xu, “Liquid on paper: Rapid prototyping of soft functional components for paper electronics,” *Sci. Rep.*, vol. 5, pp. 1–11, 2015.

[69] M. M. Ali *et al.*, “A Printed Multicomponent Paper Sensor for Bacterial Detection,” *Sci. Rep.*, vol. 7, no. 1, pp. 1–10, 2017.

[70] X. Liu, M. Mwangi, X. Li, M. O’Briena, and G. M. Whitesides, “Paper-based piezoresistive MEMS sensors,” *Lab Chip*, vol. 11, no. 13, pp. 2189–2196, 2011.

[71] H. Liu, H. Jiang, F. Du, D. Zhang, Z. Li, and H. Zhou, “Flexible and Degradable Paper-Based Strain Sensor with Low Cost,” *ACS Sustain. Chem. Eng.*, vol. 5, no. 11, pp. 10538–10543, 2017.

[72] X. Liao *et al.*, “Flexible and printable paper-based strain sensors for wearable and large-area green electronics,” *Nanoscale*, vol. 8, no. 26, pp. 13025–13032, 2016.

[73] S. B. Aziz, T. J. Woo, M. F. Z. Kadir, and H. M. Ahmed, “A Conceptual Review on Polymer Electrolytes and Ion Transport Models,” *J. Sci. Adv. Mater. Devices*, pp. 1–17, 2018.

[74] M. A. B. H. Susan, T. Kaneko, A. Noda, and M. Watanabe, “Ion gels prepared by in situ radical polymerization of vinyl monomers in an ionic liquid and their characterization as polymer electrolytes,” *J. Am. Chem. Soc.*, vol. 127, no. 13, pp. 4976–4983, 2005.

[75] Q. Sun *et al.*, “Transparent, low-power pressure sensor matrix based on coplanar-gate graphene transistors,” *Adv. Mater.*, vol. 26, no. 27, pp. 4735–4740, 2014.

[76] S. K. Lee, S. M. Humayun Kabir, B. K. Sharma, B. J. Kim, J. H. Cho, and J. H. Ahn, “Photo-patternable ion gel-gated graphene transistors and inverters on plastic,” *Nanotechnology*, vol. 25, no. 1, 2014.

[77] A. F. Visentin and M. J. Panzer, “Poly(ethylene glycol) diacrylate-supported ionogels with consistent capacitive behavior and tunable elastic response,” *ACS Appl. Mater. Interfaces*, vol. 4, no. 6, pp. 2836–2839, 2012.

[78] S. W. Lee *et al.*, “Periodic array of polyelectrolyte-gated organic transistors from

electrospun poly(3-hexylthiophene) nanofibers," *Nano Lett.*, vol. 10, no. 1, pp. 347–351, 2010.

[79] B. Nie, R. Li, J. Cao, J. D. Brandt, and T. Pan, "Flexible Transparent Iontronic Film for Interfacial Capacitive Pressure Sensing," *Adv. Mater.*, vol. 27, no. 39, pp. 6055–6062, 2015.

[80] M. Armand, F. Endres, D. R. MacFarlane, H. Ohno, and B. Scrosati, "Ionic-liquid materials for the electrochemical challenges of the future.," *Nat. Mater.*, vol. 8, no. 8, pp. 621–9, 2009.

[81] M. Isik, H. Sardon, and D. Mecerreyes, "Ionic liquids and cellulose: Dissolution, chemical modification and preparation of new cellulosic materials," *Int. J. Mol. Sci.*, vol. 15, no. 7, pp. 11922–11940, 2014.

[82] S. Sen, J. D. Martin, and D. S. Argyropoulos, "Review of cellulose non-derivatizing solvent interactions with emphasis on activity in inorganic molten salt hydrates," *ACS Sustain. Chem. Eng.*, vol. 1, no. 8, pp. 858–870, 2013.

[83] R. P. Swatloski, S. K. Spear, J. D. Holbrey, and R. D. Rogers, "Dissolution of cellulose with ionic liquids," *J. Am. Chem. Soc.*, vol. 124, no. 18, pp. 4974–4975, 2002.

[84] Q. Chen, H. Chen, L. Zhu, and J. Zheng, "Fundamentals of double network hydrogels," *J. Mater. Chem. B*, vol. 3, no. 18, pp. 3654–3676, 2015.

[85] S. Liang, J. Wu, H. Tian, L. Zhang, and J. Xu, "High-strength cellulose/poly(ethylene glycol) gels," *ChemSusChem*, vol. 1, no. 6, pp. 558–563, 2008.

[86] D. M. DeLongchamp and P. T. Hammond, "Fast ion conduction in layer-by-layer polymer films," *Chem. Mater.*, vol. 15, no. 5, pp. 1165–1173, 2003.

[87] R. C. Agrawal and G. P. Pandey, "Solid polymer electrolytes: Materials designing and all-solid-state battery applications: An overview," *J. Phys. D. Appl. Phys.*, vol. 41, no. 22, 2008.

[88] H. Jin *et al.*, "Stretchable Dual-Capacitor Multi-Sensor for Touch-Curvature-Pressure-Strain Sensing," *Sci. Rep.*, vol. 7, no. 1, pp. 1–8, 2017.

[89] M. Ahmadi, R. Rajamani, and S. Sezen, "Transparent Flexible Active Faraday Cage

Enables In Vivo Capacitance Measurement in Assembled Microsensor," *IEEE Sensors Lett.*, vol. 1, no. 5, pp. 1–4, Oct. 2017.

[90] G. W. Parker, "Electric field outside a parallel plate capacitor," *Am. J. Phys.*, vol. 70, no. 5, p. 502, 2002.

[91] X. Wu, M. Hu, J. Shen, and Q. Ma, "A miniature piezoresistive catheter pressure sensor," *Sensors Actuators A Phys.*, vol. 35, no. 5, pp. 197–201, 1993.

[92] K. V. Meena, R. Mathew, and A. R. Sankar, "Design and optimization of a three-terminal piezoresistive pressure sensor for catheter based in vivo biomedical applications," *Biomed. Phys. Eng. Express*, vol. 3, no. 4, 2017.

[93] M. Esashi *et al.*, "Fabrication Of Catheter-Tip And Sidewall Miniature Pressure Sensors," *IEEE Trans. Electron Devices*, vol. 29, no. 1, pp. 57–63, 1982.

[94] R. Otmani, N. Benmoussa, and B. Benyoucef, "The thermal drift characteristics of piezoresistive pressure sensor," *Phys. Procedia*, vol. 21, pp. 47–52, 2011.

[95] P. Dario, D. Femi, and F. Vivaldi, "Fiber-optic catheter-tip sensor based on the photoelastic effect," *Sensors and Actuators*, vol. 12, no. 1. pp. 35–47, 1987.

[96] D. Tosi, S. Poeggel, I. Iordachita, and E. Schena, "Fiber Optic Sensors for Biomedical Applications," in *Opto-Mechanical Fiber Optic Sensors: Research, Technology, and Applications in Mechanical Sensing*, 2018, pp. 301–333.

[97] N. Wu, Y. Tian, X. Zou, and Y. Zhai, "A miniature fiber optic blood pressure sensor and its application in in vivo blood," *Sensors Actuators B Chem.*, 2013.

[98] M. Ahmadi, R. Rajamani, and S. Sezen, "Transparent Flexible Active Faraday Cage Enables In Vivo Capacitance Measurement in Assembled Microsensor," *IEEE Sensors Lett.*, vol. 1, no. 5, pp. 6072–6078, 2017.

[99] M. Ahmadi, R. Rajamani, G. Timm, and S. Sezen, "Instrumented Urethral Catheter and Its Ex Vivo Validation in a Sheep Urethra," *Meas Sci Technol.*, vol. 28, no. 3, pp. 1–10, 2017.

[100] Y. Zhang, R. Rajamani, and S. Sezen, "Novel Supercapacitor-Based Force Sensor Insensitive to Parasitic Noise," vol. 1, no. 6, pp. 2–5, 2017.

[101] J. T. A. P. Abrams, J. G. Blaivas, S. L. Stanton, "The standardization of terminology of lower urinary tract function recommended by the international continence

society," *Int. Urogynecol. J.*, vol. 1, no. 1, pp. 45–58, 1990.

[102] K. Bø, "Urinary incontinence, pelvic floor dysfunction, exercise and sport," *Sport. Med.*, vol. 34, no. 7, pp. 451–464, 2004.

[103] Y. S. Hannestad, G. Rortveit, H. Sandvik, and S. Hunskaar, "A community-based epidemiological survey of female urinary incontinence: the Norwegian EPINCONT study. Epidemiology of Incontinence in the County of Nord-Trøndelag.," *J. Clin. Epidemiol.*, vol. 53, no. 11, pp. 1150–7, 2000.

[104] D. H. Thom, M. N. Haan, and S. K. Van Den Eeden, "Medically recognized urinary incontinence and risks of hospitalization, nursing home admission and mortality," *Age Ageing*, vol. 26, no. 5, pp. 367–374, 1997.

[105] W. Schfer *et al.*, "Good Urodynamic Practices: Uroflowmetry, filling cystometry, and pressure-flow studies," *Neurourol. Urodyn.*, vol. 21, no. 3, pp. 261–274, 2002.

[106] M. Ahmadi, R. Rajamani, G. Timm, and A. S. Sezen, "Flexible Distributed Pressure Sensing Strip for a Urethral Catheter," *J. Microelectromechanical Syst.*, vol. 24, no. 6, pp. 1840–1847, 2015.

[107] J. Y. Sung, H. I. Christensen, and R. E. Grinter, "Sketching the future: Assessing user needs for domestic robots," *Proc. - IEEE Int. Work. Robot Hum. Interact. Commun.*, pp. 153–158, 2009.

[108] M. Cakmak and L. Takayama, "Towards a comprehensive chore list for domestic robots," *ACM/IEEE Int. Conf. Human-Robot Interact.*, vol. 4, pp. 93–94, 2013.

[109] P. Fiorini and E. Prassler, "Cleaning and Household Robots: A Technology Survey," *Auton. Robots*, vol. 9, no. 3, pp. 227–235, 2000.

[110] F. Zhu and J. W. Spronck, "A capacitive tactile sensor for shear and normal force measurements," *Sensors and Actuators: A. Physical*, vol. 31, no. 1–3. pp. 115–120, 1992.

[111] L. Wang and D. J. Beebe, "A Silicon-based shear force sensor: development and characterization," *Sensors Actuators, A Phys.*, vol. 84, no. 1, pp. 33–44, 2000.

[112] L. Wang and D. J. Beebe, "Characterization of a silicon-based shear-force sensor on human subjects," *IEEE Trans. Biomed. Eng.*, vol. 49, no. 11, pp. 1340–1347, 2002.

[113] R. D. Ponce, J. D. Posner, and V. J. Santos, "Bioinspired Flexible microfluidic

normal force sensor skin for tactile feedback," *Sensors Actuators A. Phys.*, vol. 179, pp. 62–69, 2012.

[114] M. Y. Cheng, C. L. Lin, Y. T. Lai, and Y. J. Yang, "A polymer-based capacitive sensing array for normal and shear force measurement," *Sensors (Switzerland)*, vol. 10, no. 11, pp. 10211–10225, 2010.

[115] L. Beccai *et al.*, "Design and fabrication of a hybrid silicon three-axial force sensor for biomechanical applications," *Sensors and Actuators, A: Physical*, vol. 120, no. 2. pp. 370–382, 2005.

[116] T. Iwasaki *et al.*, "Shearing force measurement device with a built-in integrated micro displacement sensor," *Sensors and Actuators, A: Physical*, vol. 221. pp. 1–8, 2015.

[117] T. Takeshita, K. Harisaki, H. Ando, E. Higurashi, H. Nogami, and R. Sawada, "Development and evaluation of a two-axial shearing force sensor consisting of an optical sensor chip and elastic gum frame," *Precision Engineering*, vol. 45. pp. 136–142, 2016.

[118] T. A. Chase and R. C. Luo, "A thin-film flexible capacitive tactile normal/shear force array sensor," in *Proceedings of IECON '95 - 21st Annual Conference on IEEE Industrial Electronics*, 1995, pp. 1196–1201.

[119] H. Lee, J. Chung, S. Chang, and E. Yoon, "Polymer Tactile Sensing Array with A Unit Cell of Multiple Capacitors for Three-axis Contact Force Image," *MEMS Conf.*, no. January, pp. 623–626, 2007.

[120] L. Viry *et al.*, "Flexible three-axial force sensor for soft and highly sensitive artificial touch," *Adv. Mater.*, vol. 26, no. 17, pp. 2659–2664, 2014.

[121] Hyung-Kew Lee, Jaehoon Chung, Sun-Il Chang, and Euisik Yoon, "Normal and Shear Force Measurement Using a Flexible Polymer Tactile Sensor With Embedded Multiple Capacitors," *J. Microelectromechanical Syst.*, vol. 17, no. 4, pp. 934–942, 2008.

[122] J. A. Dobrzynska and M. A. M. Gijs, "Polymer-based flexible capacitive sensor for three-axial force measurements," *J. Micromechanics Microengineering*, vol. 23, no. 1, 2013.

[123] P. Roberts, D. D. Damian, W. Shan, T. Lu, and C. Majidi, “Soft-matter capacitive sensor for measuring shear and pressure deformation,” *Proc. - IEEE Int. Conf. Robot. Autom.*, pp. 3529–3534, 2013.

[124] H. K. Lee, J. Chung, S. Il Chang, and E. Yoon, “Real-time measurement of the three-axis contact force distribution using a flexible capacitive polymer tactile sensor,” *J. Micromechanics Microengineering*, vol. 21, no. 3, 2011.

[125] T. Nakadegawa, H. Ishizuka, and N. Miki, “Three-axis scanning force sensor with liquid metal electrodes,” *Sensors and Actuators, A: Physical*, vol. 264. pp. 260–267, 2017.

[126] S. Sapna, “Backpropagation Learning Algorithm Based on Levenberg Marquardt Algorithm,” 2012, pp. 393–398.

[127] P. Diagrams and M. Word, “Neural Network Ensembles, Cross Validation, and Active Learning Anders,” *Adv. neural Netw. Process. Syst.*, vol. 7, pp. 6–7, 2010.

[128] D. F. Specht, “1991_ITNN_A general regression neural network.pdf,” *IEEE Transaction on Neural Network*, vol. 2, no. 6. pp. 568–576, 1991.

[129] A. Reynaldi, S. Lukas, and H. Margaretha, “Backpropagation and Levenberg-Marquardt algorithm for training finite element neural network,” *Proc. - UKSim-AMSS 6th Eur. Model. Symp. EMS 2012*, no. 2, pp. 89–94, 2012.

[130] Y. Zhang, M. Ahmadi, and R. Rajamani, “An Instrumented Urethral Catheter With Supercapacitor Based Force Sensor,” 2018, p. V001T06A002.

[131] H. J. Xian *et al.*, “Flexible strain sensors with high performance based on metallic glass thin film,” *Appl. Phys. Lett.*, vol. 111, no. 12, pp. 1–6, 2017.

[132] E. Puyoo *et al.*, “Metallic nanoparticle-based strain sensors elaborated by atomic layer deposition,” *Appl. Phys. Lett.*, vol. 110, no. 12, 2017.

[133] R. Sun *et al.*, “Kirigami stretchable strain sensors with enhanced piezoelectricity induced by topological electrodes,” *Appl. Phys. Lett.*, vol. 112, no. 25, pp. 1–6, 2018.

[134] Q. Li, K. Wang, Y. Gao, J. P. Tan, R. Y. Wu, and F. Z. Xuan, “Highly sensitive wearable strain sensor based on ultra-violet/ozone cracked carbon nanotube/elastomer,” *Appl. Phys. Lett.*, vol. 112, no. 26, pp. 1–4, 2018.

[135] A. Apilux, W. Dungchai, W. Siangproh, N. Praphairaksit, C. S. Henry, and O.

Chailapakul, “Lab-on-paper with dual electrochemical/colorimetric detection for simultaneous determination of gold and iron.,” *Anal. Chem.*, vol. 82, no. 5, pp. 1727–1732, 2010.

[136] S. Ahmed, M. P. N. Bui, and A. Abbas, “Paper-based chemical and biological sensors: Engineering aspects,” *Biosens. Bioelectron.*, vol. 77, pp. 249–263, 2016.

[137] X. Liao *et al.*, “Flexible and printable paper-based strain sensors for wearable and large-area green electronics,” *Nanoscale*, vol. 8, no. 26, pp. 13025–13032, 2016.

[138] X. Liao *et al.*, “Flexible and highly sensitive strain sensors fabricated by pencil drawn for wearable monitor,” *Adv. Funct. Mater.*, vol. 25, no. 16, pp. 2395–2401, 2015.

[139] C. Yan *et al.*, “Highly stretchable piezoresistive graphene-nanocellulose nanopaper for strain sensors,” *Adv. Mater.*, vol. 26, no. 13, pp. 2022–2027, 2014.

[140] S. Zhang, R. Rajamani, L. Alexander, and A. Serdar Sezen, “Note: Development of leg size sensors for fluid accumulation monitoring,” *Rev. Sci. Instrum.*, vol. 87, no. 5, pp. 1–4, 2016.

[141] Y. Liu, H. Wang, W. Zhao, H. Qin, and X. Fang, “Thermal-performance instability in piezoresistive sensors: Inducement and improvement,” *Sensors (Switzerland)*, vol. 16, no. 12, pp. 1–23, 2016.

[142] B. Nie, R. Li, J. Cao, J. D. Brandt, and T. Pan, “Flexible Transparent Iontronic Film for Interfacial Capacitive Pressure Sensing,” *Adv. Mater.*, vol. 27, no. 39, pp. 6055–6062, 2015.

[143] A. B. A. Manaf, K. Nakamura, and Y. Matsumoto, “Characterization of miniaturized one-side-electrode-type fluid-based inclinometer,” *Sensors Actuators A Phys.*, vol. 144, no. 1, pp. 74–82, 2008.

[144] Y. Zhang, S. Sezen, M. Ahmadi, X. Cheng, and R. Rajamani, “Paper-Based Supercapacitive Mechanical Sensors,” *Sci. Rep.*, vol. 8, no. 1, p. 16284, 2018.

[145] J.-H. Choi *et al.*, “Random network transistor arrays of embedded ZnO nanorods in ion-gel gate dielectric,” *J. Mater. Chem.*, vol. 20, no. 35, p. 7393, 2010.

[146] P. Schexnailder and G. Schmidt, “Nanocomposite polymer hydrogels,” *Colloid Polym. Sci.*, vol. 287, no. 1, pp. 1–11, 2009.

[147] C. J. Wu, A. K. Gaharwar, P. J. Schexnailder, and G. Schmidt, “Development of biomedical polymer-silicate nanocomposites: A materials science perspective,” *Materials (Basel).*, vol. 3, no. 5, pp. 2986–3005, 2010.

[148] K. Haraguchi, “Synthesis and properties of soft nanocomposite materials with novel organic/inorganic network structures,” *Polym. J.*, vol. 43, no. 3, pp. 223–241, 2011.

[149] H. Nanoparticles, “Highly Extensible , Tough , and Elastomeric Nanocomposite Hydrogels from Poly (ethylene glycol) and Hydroxyapatite ... Highly Extensible , Tough , and Elastomeric Nanocomposite Hydrogels,” no. March 2011, pp. 1641–1650, 2017.

[150] A. K. Gaharwar, C. P. Rivera, C. J. Wu, and G. Schmidt, “Transparent, elastomeric and tough hydrogels from poly(ethylene glycol) and silicate nanoparticles,” *Acta Biomater.*, vol. 7, no. 12, pp. 4139–4148, 2011.

[151] V. V. Zuev, “The mechanisms and mechanics of the toughening of epoxy polymers modified with fullerene C60,” *Polym. Eng. Sci.*, vol. 52, no. 12, pp. 2518–2522, 2012.

[152] C. M. Manjunatha, A. C. Taylor, A. J. Kinloch, and S. Sprenger, “The tensile fatigue behaviour of a silica nanoparticle-modified glass fibre reinforced epoxy composite,” *Compos. Sci. Technol.*, vol. 70, no. 1, pp. 193–199, 2010.

[153] A. K. Gaharwar, C. Rivera, C. J. Wu, B. K. Chan, and G. Schmidt, “Photocrosslinked nanocomposite hydrogels from PEG and silica nanospheres: Structural, mechanical and cell adhesion characteristics,” *Mater. Sci. Eng. C*, vol. 33, no. 3, pp. 1800–1807, 2013.

[154] D. Hayn, S. Raschhofer, M. Falgenhauer, R. Modre-osprian, F. Fruhwald, and G. Schreier, “Edema Detection for Heart Failure Patients in Home Monitoring Scenarios AIT Austrian Institute of Technology GmbH , Graz , Austria Medical University of Graz , Austria Introduction Sensor system Edema parameters,” pp. 93–96, 2012.

[155] K. G. Brodowicz, K. McNaughton, N. Uemura, G. Meininger, C. J. Girman, and S. H. Yale, “Reliability and feasibility of methods to quantitatively assess peripheral edema,” *Clin. Med. Res.*, vol. 7, no. 1–2, pp. 21–31, 2009.

[156] R. Strauß, S. Ewig, K. Richter, T. König, G. Heller, and T. T. Bauer, “The prognostic significance of respiratory rate in patients with pneumonia: A retrospective analysis of data from 705 928 hospitalized patients in Germany from 2010-2012,” *Dtsch. Arztebl. Int.*, vol. 111, no. 29–30, pp. 503–508, 2014.

[157] F. Q. Al-Khalidi, R. Saatchi, D. Burke, H. Elphick, and S. Tan, “Respiration rate monitoring methods: A review,” *Pediatr. Pulmonol.*, vol. 46, no. 6, pp. 523–529, 2011.

[158] S. Ianchulev, D. Ladd, C. MacNabb, N. Marengi, E. Cho, and J. Freeman, “Use of a respiratory volume monitor to assess respiratory competence in cardiac surgery patients after extubation,” *Cardiology*, vol. 125, no. s2, p. 388, 2013.

[159] Voscopoulos, “Non-Invasive Respiratory Volume Monitoring to Detect Apnea in Post-Operative Patients: Case Series,” *J. Clin. Med. Res.*, vol. M, no. 3, pp. 209–214, 2014.

[160] L. Nilsson, A. Johansson, and S. Kalman, “Monitoring of respiratory rate in postoperative care using a new photoplethysmographic technique . PubMed Commons,” vol. 16, no. 4, pp. 309–315, 2001.

[161] D. Zito *et al.*, “SoC CMOS UWB pulse radar sensor for contactless respiratory rate monitoring,” *IEEE Trans. Biomed. Circuits Syst.*, vol. 5, no. 6, pp. 503–510, 2011.